DISSERTATION

submitted to the
Combined Faculties for the Natural Sciences and Mathematics
of the Ruperto-Carola University of Heidelberg, Germany
for the degree of
Doctor of Natural Sciences

presented by
Nina Korablinova

born in Kaliningrad, Russia

Oral examination: 28th January, 2004

MEASURING CORNEAL TOPOGRAPHY USING WAVEFRONT ANALYSIS TECHNIQUE

Referees: Prof. Dr. Josef Bille
Prof. Dr. Wolfgang Schlegel

ABSTRACT

Refractive surgery has emphasized the need of accurate and precise methods for measuring the power of the human cornea. Available techniques for measuring corneal topography include keratometry, videokeratoscopy, and scanning slit imaging.

A new type of instrument, a corneal topographer based on a Hartmann-Shack wavefront sensor for measuring corneal elevation over a spherical surface, is presented in this thesis.

The performed tests of the topography system showed a high accuracy and reproducibility of the measurements on spherical as well as on toric test sample surfaces that approximate the curvature of the central human cornea. A comparison between the data obtained by the topographer and those provided by a videokeratoscope showed that the topographer is as precise as standard instruments used in clinical praxis.

The measurements on human corneas demonstrated the importance of a Z-tracker module for the correct placement of the corneal surface. To enhance the accuracy of the topography system, a better tracking of the corneal position is necessary to compensate for the rapid eye movements during the examination that strongly affect the measurements. Additionally, more clinical studies are necessary to test the topographer on human cornea and to give an evidence for the clinical acceptance of the instrument.

ZUSAMMENFASSUNG

Die refraktive Chirurgie gab einen Anstoß für die Entwicklung der präzisen Methoden zur Bestimmung der Brechkraft der menschlichen Hornhaut. Die vorhandenen Techniken umfassen solche Methoden wie Keratometrie, Videokeratometrie und Slit-Imaging Photographie.

In dieser Arbeit ist ein auf einem Hartmann-Shack Wellenfrontsensor basierender Hornhauttopograph präsentiert, der die Hornhauterhebung über eine sphärische Fläche bestimmt.

Die Testmessungen an Probekörpern, die ähnliche optische Eigenschaften besitzen wie die menschliche Hornhaut, zeigten eine hohe Genauigkeit und Reproduzierbarkeit des Hornhauttopographen. Ein Vergleich der Messdaten mit denen, die mit einem Videokeratoskop gewonnen wurden, zeigte eine gute Präzision des Hornhauttopographen in der Bestimmung der sphärischen als auch asphärischen Oberflächenform der Probekörper.

Die Testmessungen an menschlicher Hornhaut veranschaulichten die Notwendigkeit eines Z-Trackers für eine genaue Positionierung der Hornhautoberfläche. Um die Genauigkeit des Hornhauttopographen für die Messung an der menschlichen Hornhaut noch weiter zu erhöhen, ist jedoch eine bessere als die benutzte Technik zur Überwachung der Hornhautposition nötig. Diese muß in der Lage sein, rasche Augenbewegungen zu kompensieren, die die Messung mit dem Hornhauttopographen erheblich stören. Weitere umfangreiche klinische Erprobungen des Hornhauttopographen am menschlichen Auge sind erforderlich, um seine mögliche Anwendung in der Ophthalmologie zu beurteilen.

Contens

CHAPTER 1

INTRODUCTION

The anterior part of the human eye is limited by a perfectly transparent media, called the cornea. In addition to its mechanical function, the cornea has two major roles in vision. First, it is transparent to enable light to be transmitted to the retina. Second, its anterior surface is the primary refractive element of the human eye. With its refractive power of about 42 diopters the cornea contributes almost 70% of the total optical power of the eye (60 diopters). Thus, it plays an important role by the refraction and focussing of the light on the retina, and subtle variations in its shape significantly affect the patient's visual acuity.

The optical quality of the cornea is a critical factor in proper visual function of the human eye and can be determined using corneal topography - a method of corneal shape examination assisted by computer analysis. Instruments that measure the cornea's topography are called corneal topographers, and they have recently become a quite common tool for clinicians.

The most corneal topographers used in clinical praxis today are based on Placido's disc technique. They project a series of illuminated rings onto the corneal surface, which are reflected back and captured by a video camera. The images of the reflected rings of light are analyzed by a computer, and different topographical maps of the cornea are generated that reveal any distortions of the cornea, such as the corneal curvature, meridians of astigmatism, and corneal irregularities as well as the keratoconus or corneal scarring. This diagnostic procedure is essential for patients being considered for refractive surgical procedures (such as LASIK[1]) and may even be necessary in the follow-up of some patients who have undergone these refractive surgical procedures.

In recent years some new and alternative methods for measuring corneal topography were invented [41]. However, some instruments are widthwise used, some of them are not commercially available or only in testing phase. One of these new methods for measuring corneal topography is the wavefront analysis with a Hartmann-Shack wavefront sensor.

---

[1] LASIK is an abbreviation for Laser-in-situ-Keratomileusis, a surgical procedure for correcting refractive errors using an Excimer laser.

A Hartmann-Shack wavefront sensor (HSS) is a device that provides a way to precisely measure the phase information of the wavefront. It uses an array of micro lenses to focus the rays emerging from an optical system such as the human eye or refracted from the cornea onto a CCD camera positioned in the focal plane of the lens array. The local slope of the wavefront is determined by the lateral offset of the focus from each micro lens. The phase information is then derived from the slope. Using this technique the optical aberrations of the wavefront can be measured objectively and described mathematically.

In this work a new method using the wavefront analysis technique with a Hartmann-Shack wavefront sensor for measuring corneal topography is presented. A corneal topographer, called the HSS Corneal Topographer, was built up and tested as an instrument for possible clinical use. The test measurements showed that this system offers one precise way of measuring the shape of the anterior corneal surface and the accurate reconstruction of it.

The organization of the thesis is as follows.

In Chapter 2, the main anatomical factors governing the human eye, especially the structure of the cornea and its optical properties are reviewed. It also describes the common visual aberrations of the human eye, and how clinicians correct them.

Chapter 3 focuses on corneal topography. It provides information on historical background and several methods for measuring corneal topography. The way the corneal data is normally displayed and the basic terminology in corneal topography is introduced to help one to better understand the data provided by the corneal topographers.

Chapter 4 builds on wavefront analysis technique. It explains the basic concept of a Hartmann-Shack wavefront sensor, its characteristics, and limitations. The wavefront reconstruction and representation with Zernike polynomials are described.

Chapter 5 explains optical principle and technical aspects of the corneal topography system (HSS Corneal Topographer) used in this work for measuring corneal topography. A description of the least squares algorithm of modal wavefront estimation from derivatives used in software tool follows.

Chapter 6 describes tests of the software algorithm. Special attention is given to simulations and test measurements.

Finally, Chapter 7 summarizes the principal contributions of this dissertation and discusses some possibilities to improve the topography unit in the future.

Additionally, Appendix A catalogues the software description and short user manual.

Chapter 2

THE HUMAN EYE

The anatomy of the human eye is extensively reviewed in several ophthalmic and physiological textbooks. In this chapter some important aspects including a short description of the human eye, cornea, and its properties are highlighted. Additionally, some of the corneal disorders and common vision problems which plague humans and the customary solutions to those problems are investigated. For more detailed information of the structural importance of the eye, see [42, 13, 33].

2.1 Anatomy of the Human Eye

The human eye is a complex anatomical device that remarkably demonstrates the architectural wonders of the human body.

The general structure of the human eye is given in Fig. 2.1. The ultimate goal of such an anatomy is to allow humans to focus images on the retina, and each optical element of the eye plays a distinct part in enabling humans to see.

The eye is essentially an opaque eyeball filled with a water-like fluid. The transparent front surface of the eye is known as the cornea. The cornea has the dual purpose of protecting the eye and refracting light as it enters the eye. As part of the tough outer coat of the eye, the cornea, together with the sclera, should maintain the intraocular pressure, support the intraocular structures, and resist trauma and infection.

After light passes through the cornea, a portion of it passes through an opening of the iris known as the pupil. The iris, visible through the cornea, contains involuntary muscles which react to incoming luminance, and thus, the iris has an automatic ability to modify the pupil size playing an important optical function as an aperture. In bright-light situations, the iris is minimized to reduce the size of the pupil and limit the amount of light which enters the eye; and in dim-light situations, the pupil size expands to its maximal size to allow in as much light as possible.

Light which passes through the pupil opening, enters the crystalline lens which focuses the light onto the back of the eye. The crystalline lens is made of a transparent, high-protein material - fibrous, contained within an elastic capsule. Its structure is complex, composed of a radial pattern of fibrous layers which is the source of diffraction halos people see at night. The lens is surrounded by ciliary muscles which

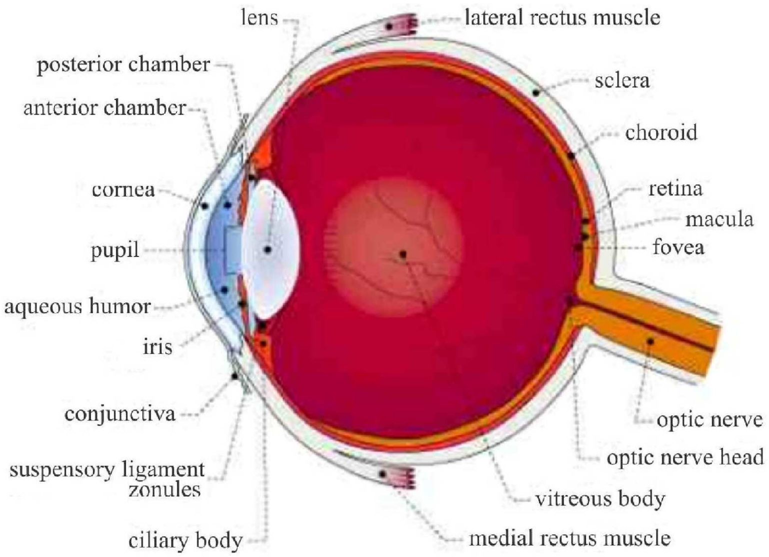

Fig. 2.1. A side view of the human eye.

relax and contract in order to change the shape of the lens (and therefore its refractive power) to allow the eye to focus on objects at different distances - a process known as accommodation. As the lens ages, it becomes harder and undergoes reduced flexibility and transparency, severely limiting the degree of accommodation - a condition called presbyopia.

The inner layer of the eye is the retina, which is an extension of the central nervous system. The retina contains two types of light-sensitive cells called rods and cones[1]. These cells convert the light energy into neural signals sent to the brain for interpretation via the optic nerve. The rods are very sensitive to light and are suited to and only function at low light levels. But they provide poor spatial resolution. The cones are far less sensitive to light than rods and only function at high light levels. On the other hand, the cones are capable of providing high spatial resolution and color vision. They predominate in the central region of the retina called fovea. As the distance from the fovea increases, the number of rods increases and the number of cones decrease (the rods reach their maximum density at about 20° from the fovea). The peripheral region of the retina is used more for light and motion detection, whereas the foveal area (1.5 mm in diameter) is used more for form detection, color detection, and resolution of fine detail.

There are as many as one-million neural pathways from the rods and cones to the brain through that the nerve impulses travel. This network of nerve cells is bundled together to form the optic nerve. The area where the optic nerve connects to the retina, called optic disc, contains neither rods nor cones, and thus, this region is blind, hence the name the blind spot.

---

[1] An adult eye is typically equipped with 120 million rods which detect the intensity of light and 6 million cones which detect the frequency of light.

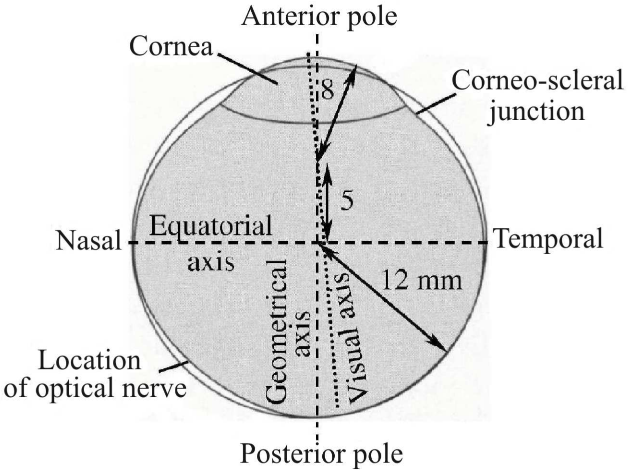

Fig. 2.2. Shape and dimensions of the human eye. The departure of the eye's cross section from a circle that best fits the sclera is shown. Note that the sclera is flattened around the optical nerve and around the cornea.

2.2 Shape and Dimensions of the Human Eye

As for all organs, the dimensions of the human eye and its optical components vary greatly from person to person and some further depend upon accommodation level, age and certain pathological conditions. In spite of these variations, average values have been used to construct representative or schematic eye (Section 2.3).

In an idealized geometrical form of the eye, the sclera would be a sphere having a radius of about 12 mm with a transparent portion of a sphere of 8 mm radius added anteriorly to represent the cornea. The distance between the centers of these two curvatures is approximately 5 mm (Fig. 2.2).

To fully describe the optical properties of the eye, a number of axes should be introduced. It is important to distinguish the geometrical axis from the visual axis.

The geometrical axis (also called optical axis) goes through the anterior and posterior poles of the eye and is usually defined as the line joining the center of curvature of the refracting surfaces. This axis requires the existence of the nodal point, which only exists if the eye is rotationally symmetric. However, the optical system of the eye is not perfectly rotationally symmetric, and therefore even if the four refracting surfaces were each perfectly rotationally symmetric, the four centers of curvatures would not be co-lined. In the case of the eye, we define the optical axis as the line of best fit through these non co-lined points.

The visual axis is defined as the line joining the object of interest (fixation point) and the fovea, which passes through the nodal points.

The optical and visual axes are tilted to each other by about 5°.

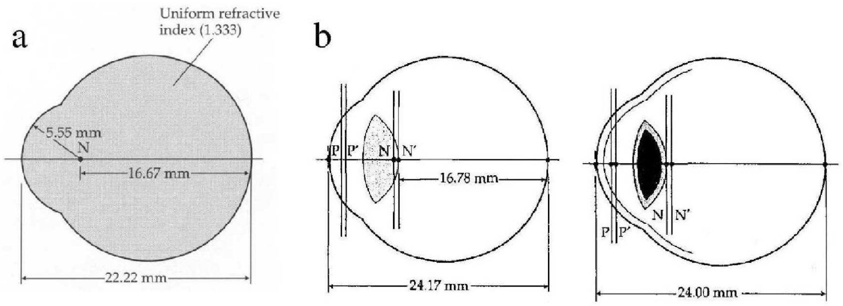

Fig. 2.3. The cornea-lens combination of the real eye can be represented in several simplified forms: **a** - a reduced eye, **b** - Gullstrand's schematic eyes named as a "simplified eye" (left) and an "exact eye" (right). The cross-sectional drawings of the eye show, to scale, the curvatures and dimensions of the eye, along with the locations of the principal planes (P and P') and nodal points (N and N'). All the optical surfaces have constant radii of curvature, that is, they are spherical surfaces [33].

2.3 Eye Models

To understand the optical function of the human eye some eye's models are in use that simplify and approximate an average or typical eye to some degree [42]. To construct a model of the eye, population mean value for relevant ocular parameters is used, and it can be done at different levels of sophistication.

A simple approximation is called a reduced eye (Fig. 2.3a). In this model the cornea and lens have been replaced by a single optical surface having equivalent power of the cornea-lens combination. At this surface the refractive index changes, and its power is equivalent to the eye's total power. The eye has a single nodal point (N). The corneal radius of curvature and the axial length are unrealistically small.

A closer approach to the reality might have a separate cornea and lens. Fig. 2.3b shows two of Gullstrand's schematic eyes. The "simplified eye" has a single corneal surface and a lens with a single refractive index (Fig. 2.3b left). The "exact" eye includes both corneal surfaces and a lens with different central and peripheral refractive indices (Fig. 2.3b right). The differences between these two eye models are small, but significant. The simplified eye has higher dioptric power, a flatter cornea, and a thicker lens, for example. The differences between the schematic eyes mean that they will give somewhat different answers to optical calculations. The exact eye will be required for some purpose, while the simplified eye may be sufficiently adequate for others.

In its ultimate form, the model eye is an attempt to represent the optical components of the biological eye as accurately as possible, with curvatures, thickness, and separations that mimic the true anatomy of the eye.

2.4 Optics of the Human Eye

Optically, the eye is a two-element system, made up of the cornea and the lens, both of which are plus lenses. The overall dioptric power of this system is the sum of the power of its components and is given by the equation

$$P_{Eye} = P_{Cornea} + P_{Lens} - \frac{d}{n} P_{Cornea} \cdot P_{Lens}, \tag{2.1}$$

where d is the distance between the posterior surface of the cornea and the anterior surface of the lens (the anterior chamber depth), and n is the refractive index of the aqueous humor (Tab. 2.1).

The cornea is the major refracting component of the eye and performs about two-thirds of the refraction for the relaxed eye. The remainder is provided by the lens, however, whose power increases during accommodation.

The difference between the anterior and posterior radii of corneal curvature yields an average of 42 D of convergence (for the calculation, see Section 2.5), with the anterior surface contributing 48 D of convergence and the posterior surface 6 D of divergence.

The overall power of the lens is about half that of the cornea. Average radii of curvature for the unaccommodated adult lens are around 10 mm for the anterior surface and -6 mm for the posterior surface[2]. Combining these measurements with a thickness around 4 mm gives a total unaccommodated lens power of about +20 D (assuming the lens has a refractive index of 1.413). Therefore the lens contributes about one-third of the eye's total power in its unaccommodated condition. When the lens increases in power with maximum accommodation, the anterior radius of curvature is about 5 mm and the posterior radius is about -5 mm. The combined effect increases the lens power to around +30 D.

When the cornea and lens are considered as a combined optical system, these values produce a total power for the eye of around +60 D (unaccommodated eye) and +70 D (accommodated eye)[3].

2.5 Cornea

The assessment of corneal topography is a valuable tool in the diagnosis and management of certain corneal conditions. However, before using this technique to diagnose abnormalities of corneal shape, it is vital to have a good understanding of the normal corneal shape and its natural variations. When abnormalities of corneal topography are detected, it is also important to be able to determine whether these are a result of abnormalities of the cornea itself or whether they are artifacts arising from errors in image acquisition or analysis.

---

[2] These are the values commonly used in schematic eyes.

[3] Other often cited values are based on a slightly smaller or lager corneal radius of curvature or on a different index of refraction. The precise value of the refractive power of the eye is not important, since no model is totally accurate.

Tab. 2.1. Some important optical parameters of the human eye.

Segment/Structure	Radius (mm)	Power (diopters)
Cornea		
anterior surface	7.7 - 7.8	+48.8 - +48.2
posterior surface	6.5 - 6.8	-6.2 - -5.9
Cornea (entire)		+42.8 - +42.4
Lens (unaccommodated)		
anterior surface	10.0 - 11.0	+7.7
posterior surface	-6.0	+12.8
Lens (unaccommodated) combined		+20.3
Lens (accommodated)		
anterior surface	5.0	+15.4
posterior surface	-5.0	+15.4
Lens (accommodated) combined		+30.1
Human eye (unaccommodated)		+60.8 - +60.4
Human eye (accommodated)		+69.5 - +70.4

Thickness	
Cornea (at apex)	0.5 mm
Cornea (at periphery)	0.7 - 1.2 mm
Anterior camber depth	3.3 - 3.5 mm
Lens	3.5 - 4.0 mm

Index of refraction	
Air	1.0
Corneal anterior surface	1.376
Cornea (entire)	1.3375 (SKI*)
Aqueous humor	1.336
Lens	1.413

*SKI is the abbreviation for Standard Keratometric Index (Section 3.2.1).

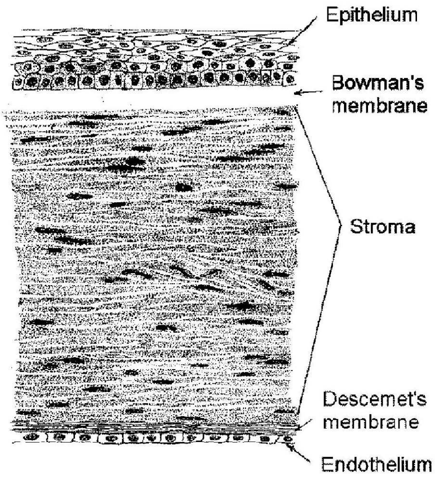

Fig. 2.4. The schematic cross-sectional structure of the five corneal layers [49].

2.5.1 Corneal Anatomy and Optics

The cornea is the transparent tissue covering the front of the eye and as a result of its position, the cornea has to meet strict physical criteria and perform a variety of specialized functions.

The basic anatomic components of the cornea account for its thickness, radius of curvature, surface regularity, and the shape of the cornea, all of which play a role in its anterior topography. Disorders of these basic components can directly affect the shape of the cornea.

It is appropriate to begin any discussion of corneal topography with an analysis of structural characteristics of the human cornea.

General Structure

The cornea has a complex structure. It is comprised of five layers, which are, in order from the outer surface of the eye: the epithelium, Bowman's membrane, the stroma, Descemet's membrane and the endothelium (Fig. 2.4).

- The epithelium is a layer of cells that cover the surface of the cornea and assure the smooth form of the surface. It is only about 5-6 cell layers thick (50 µm). Only the innermost layer of these cells is able to divide. After cells are formed, they move gradually towards the surface as the superficial cells are shed. The epithelium protects the cornea by providing a barrier against water, larger molecules, and toxic substances. It quickly regenerates when the cornea is injured (cell regularity with a turnover time of 7 days).

  The epithelium is always covered by a thin layer of tears, renewed with each blinking of the eyelid. The tear film is essential for clear vision because it moistens the cornea and fills up small irregularities of the epithelial surface improving the overall optics. The tear film does not contribute significant to the refractive power itself, since it is only 4-7 μm thick. However, the importance of the tear film is realized if it dries out. This is due to the fact that it nourishes the cornea through absorption, and the epithelium, which has a high oxygen demand, becomes hypoxic and loses its transparency.

- Bowman's membrane lies just beneath the epithelium. It is 8-14 μm thick and made up of tightly packed fine collagen fibrils. This layer being very tough and difficult to penetrate protects the cornea from injury.
- The stroma is the thickest layer (500 μm) and lies underneath Bowman's membrane. It is composed of tiny collagen lamellaes that run parallel to each other. This special formation of the collagen fibrils gives the cornea its clarity while enhancing elasticity and mechanical strength.
- Descemet's membrane lies between the stroma and the endothelium. The thickness of this membrane is about 10-12 μm. It is the basement membrane of the endothelial cells.
- The endothelium is just underneath Descemet's membrane and consists of a single layer of cells (5 μm), which are hexagonal and fit together like a honeycomb. This layer regulates the fluid balance of the cornea in order to maintain the stroma at about 78% hydration and to retain transparency. If damaged or diseased, these cells will not regenerate.

Each corneal layer has its own refractive index, but since the stroma is by far the thickest layer (90% of the entire corneal thickness), its refractive index dominates. The mean value of refractive index is usually taken as 1.376 (Tab. 2.1).

Because there are no blood vessels in the cornea (expect fine capillaries at the very extreme periphery), it is normally clear and has a shiny surface[4].

The cornea is also extremely sensitive because there are more nerve endings in the cornea than anywhere else in the body. Thus, the injuries of the cornea are painful. If the injury penetrates more deeply into the cornea, it may leave a scar - an opaque area, causing the cornea to lose its clarity and luster.

Thickness

The cornea is not uniformly thick throughout. Its thickness varies from a minimum near the corneal apex[5] (the geometric center of the cornea), being about 0.5 mm thick, to a maximum at the junction between cornea and limbus, where it is on the order of

---

[4] In disease, the cornea may be invaded by blood vessels, a condition known as pannus.

[5] The apex of the cornea is the highest spot of the cornea and location of the greatest sagittal height on the anterior corneal surface. The apex of the normal cornea is close to the optical axis. However, in pathological states such as keratoconus and after corneal surgery, the apex may be displaced.

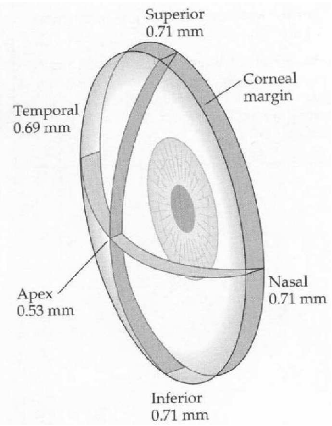

Fig. 2.5. Cross section through the cornea demonstrating the increasing thickness of the cornea from the center to the periphery. The vertical and horizontal meridians are shown here as if they were optical sections [33].

0.7 mm thick (Fig. 2.5). Temporal cornea tends to be thinner than the nasal cornea, but the difference is very small. The average thickness at the limbus measures about 1.2 mm.

Radius of curvature

Since the anterior and posterior surface are not parallel and thickness increases peripherally in all meridians, the posterior surface has a smaller radius of curvature than the anterior surface. Consequently, the corneal cross section is that of a convex-concave lens in which the power of the anterior surface is positive in sign, and the power of the posterior surface is negative (Tab. 2.1).

The radius of the curvature at the corneal vertex was determined by numerous authors (Tab. 2.2). The average radius of curvature of the anterior surface of the cornea near the pole is about 7.8 mm with the standard deviation of 0.4 mm, so that most of the subjects range between 7.0 and 8.5 mm[6]. The horizontal radius is usually 0.05-0.25 mm flatter than the vertical (with-the-rule astigmatism)[7]. In general, the mean apical radius decreases with the higher myopia.

Even though, several studies have measured the anterior radius of curvature, there have been far fewer investigations of the rear surface. It is difficult to measure the shape of the posterior surface of the cornea because of the influence of anterior surface shape on any measurement[8]. The radius of the posterior corneal surface has a slightly

---

[6] The experimental distribution of the corneal vertex radii shown that females have slightly steeper anterior corneas than males.

[7] This equates to 0.25-1.25 D of the corneal astigmatism.

[8] The posterior corneal surface is of lesser significance than the anterior surface because of the small refractive index difference across the posterior corneal boundary, but it is not of negligible significance.

Tab. 2.2. Population distribution of corneal vertex radii of curvature (mm) [1].

	Anterior	Posterior
Donders (1864)		
females	7.8	
males	7.86	
Stenstrom (1948)	7.86±0.26	
Lowe and Clark (1973)	7.65±0.27	6.46±0.26
Kiely et al. (1982)	7.72±0.27	
Edmund and Sjøntoft (1985)	7.76±0.25	
Guillon et al. (1986)	7.78±0.25	
Koretz (1989)		
females	7.69±0.23	
males	7.78±0.24	
Dunne et al. (1992)		
females	7.93±0.20	6.53±0.20
males	8.08±0.16	6.65±0.16
Patel et al. (1993)	7.68±0.40	5.81±0.41

steeper radius of curvature than the anterior surface being 6.7 mm (Fig. 2.6) [12, 28, 38].

There is a high linear correlation between the anterior and posterior radii of curvature, and a reasonable fit of this relationship is $R_{posterior} = 0.81 R_{anterior}$ [1].

Surface Regularity

The anterior surface of the cornea is lined with an epithelial layer. The superficial cells of this epithelial layer are polyhedral in shape and, under normal circumstances, do not keratinize. Their nuclei are flat and projected posteriorly. These qualities combine to create for a very smooth anterior surface of the cornea.

An intact, healthy corneal epithelial surface with a normal, smooth tear film is an essential component for the regular refraction of light by the eye, the formation of a clear retinal image, and maximum visual acuity.

Corneal Size

At birth the corneal diameter is about 10 mm. It continues to grow and reaches full size by approximately 1 year.

Viewed from the front, the outline of the cornea formed by the corneal-limbal junction is roughly elliptical (Fig. 2.7a). The longer horizontal axis of the ellipse is typically about 11.7 mm, the vertical axis around 11.6 mm (the standard deviations

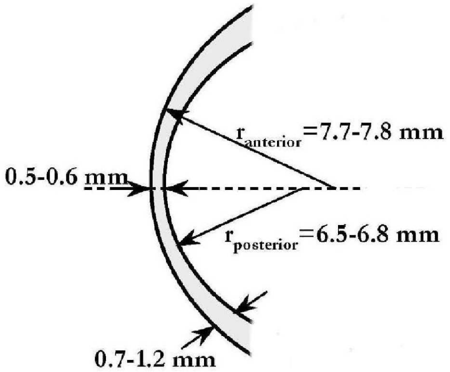

Fig. 2.6. The difference in the thickness from the center to the periphery determines the difference in radius of curvature between these two regions.

around these averages are about ±0.5 mm) [33]. The smaller vertical diameter is largely due to a superficial overlapping of the sclera onto the cornea. The outline of the posterior surface of the cornea is circular.

Normally, pupil diameter ranges from 3 mm to 6 mm, and this limits the optical zone of the cornea to the central 6 mm under most conditions.

Corneal Shape

The shape of the anterior corneal surface has been extensively studied. In profile, the central 4 mm of the cornea are approximately spherical[9] (Fig. 2.7b). Outside this optical zone, the cornea is aspheric and radially asymmetric.

The asphericity of the corneal shape means that the normal cornea becomes flattened from the center to the periphery[10] (i.e., the radius of curvature increases with distance from the surface apex). The normal cornea has a prolate shape[11]. When corneal curvature along one meridian varies symmetrically with respect to the corneal apex, the profile of the cornea can be considered as part of an ellipse.

The asphericity of the cornea can be described with the asphericity parameter Q (Section 3.4). The value of asphericity parameter for several surfaces is given in Tab. 3.3. The normal cornea has peripheral flattening corresponding to the asphericity factor of -0.26 [20].

Corneal Astigmatism

The anterior corneal surface exhibits toricity, which produces some degree of astigmatism. Corneal astigmatism is the difference in corneal curvature between two meridi-

---

[9] When examined critically, however, the cornea begins to flatten within 1 mm of the corneal apex: the curvature is always changing.

[10] At least in the adult; in a newborn baby, it is the opposite case.

[11] The reverse pattern is an oblate shape, as occurs on the long side of an ellipse (Section 3.4). This is only seen in abnormal corneas, for example by keratoconus or after radial keratotomy.

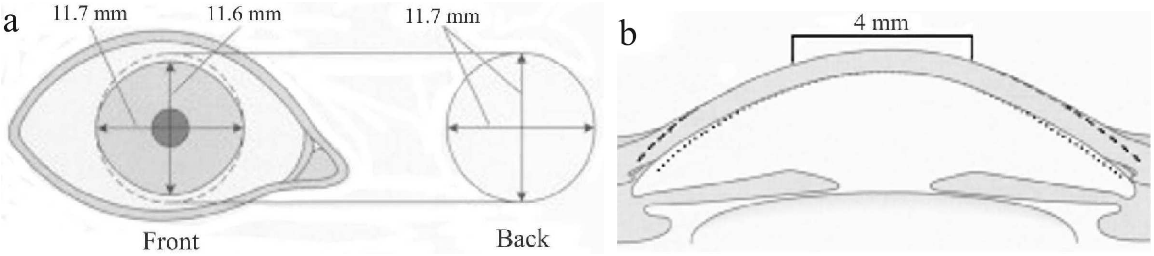

Fig. 2.7. Approximations of corneal size (**a**) and corneal shape (**b**). **a** - Viewed from in front, the outline of the cornea is slightly elliptical, with a mean vertical diameter about 1 mm less than the mean horizontal diameter. From behind, the outline of the cornea is circular [33]. **b** - The flattening of the peripheral cornea can be seen easily when its cross section is compared to a circle (dashed line). The central 4 mm of the cornea - the optical zone - have a near constant radius of curvature. Peripherally, the circle deviates from the corneal surface, and the deviation is such that the corneal radius of the curvature is larger. That is, the normal cornea is flatter. The posterior corneal surface has less peripheral flattening. Here it is also compared to a circle (dotted line).

ans and means that the cornea has a higher curvature in one direction than another.

In most individuals the horizontal meridian is the flattest and the vertical meridian the steepest[12]. The average difference between the refractive powers of these two meridians usually lies between 0.5 and 1.0 D and is called natural astigmatism.

Net Corneal Power

Most of the refraction of light occurs on the anterior surface of the cornea. It is the only air-to-tissue interface in the eye, so the change in refractive index is much greater than anywhere else. Thus, the anterior surface of the cornea dominates optically and the corneas anterior radius of curvature is the major factor in the refractive status of the eye[13].

The refractive power generated at a single spherical surface is determined by changes in the refractive index and the shape of the surface as follow

$$P = \frac{n' - n}{r}, \tag{2.2}$$

---

[12] This physiological tendency of the average cornea to have a steeper curvature vertically has not been adequately explained. Some authors explain this difference with the pressure applied by the blinking eyelids.

[13] The posterior surface of the cornea has a smaller radius of curvature than the anterior surface, but the refractive indices of the cornea and the aqueous are so similar that the posterior surface of the cornea is less important in refraction because of the relatively little refractive power.

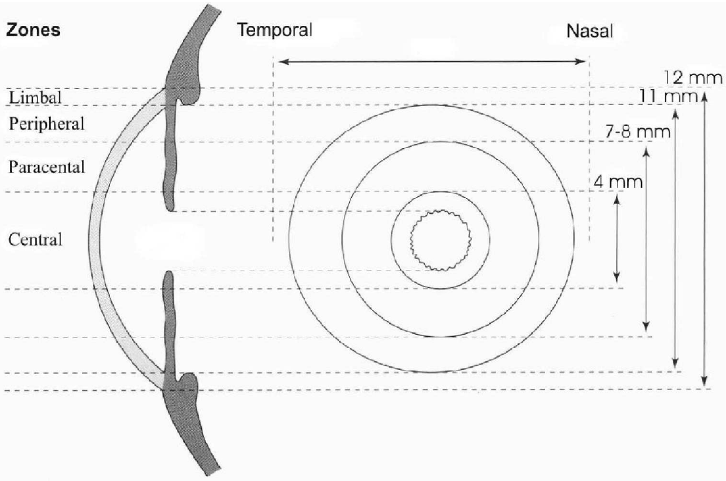

Fig. 2.8. Topographic zones of the anterior corneal surface. Diagrammatic representation of the right cornea in vertical section (left) and from anteriorly (right). None of these areas is discrete, because the cornea forms continuous curves.

where P is the refractive power (in diopters) of the surface, n and n' are the refractive indices of the first and the second bounded mediums, and r is the radius of the curvature (in meters).

As mentioned in Section 2.5, the average value for the anterior central radius of curvature is around 7.8 mm for a normal cornea, which contributes a refractive power of +48.2 D (with the cornea's refractive index of 1.376[14]). The mean value for the posterior radius of curvature is around 6.8 mm, which translates to a power of -5.9 D.

The refractive power of the entire cornea can be approximated to the sum of the power of its anterior and posterior surfaces

$$P_{Cornea} = P_{anterior} + P_{posterior} - \frac{d}{n} P_{anterior} \cdot P_{posterior} \,. \tag{2.3}$$

Combining the effects of the anterior and posterior surfaces and allowing for their separation 0.5 mm and the refraction index of 1.376 gives a total corneal power of +42.4 D.

2.5.2 Topographical Zones

Classically, the anterior corneal surface has been arbitrarily divided into four concentric regions, called optical zones (Fig. 2.8). These divisions are somewhat variable as the corneal surface is smooth and one zone blends with the next, but the concept is useful when describing the normal corneal shape and has practical applications such as the fitting of contact lenses.

---

[14] For the discussion about the refractive index of the cornea, see Section 3.2.1.

Central Zone

The central zone (otherwise called the optical zone, corneal cap, or central spherical zone) is the optically important area. This zone can be defined as the area surrounding the corneal apex. It is about 4 mm in diameter and is symmetrical and approximately spherical. Its radius of curvature does not vary by more than 0.05 mm (i.e., the refraction differs by less than 0.25 D).

The central zone is surrounded by the corneal periphery which is divided into three zones: paracentral, peripheral, and limbal.

Paracentral Zone

The paracentral zone is an annulus 4 to 7-8 mm diameter. Normally, the paracentral zone has a flatter radius of curvature than the central zone. After radial keratotomy, this is the region where a marked change in curvature - the paracentral knee - between the new, flatter, central zone and the new, peripheral, steeper corneas occurs.

Together with the central zone, it forms the apical zone used for contact lens fitting. In an ideal situation, the apical zone of the cornea would be perfectly spherical. In actuality, the majority of corneas are spherocylindrical lenses with the axis of highest power separated from the axis of lowest power by 90°. In certain situations, such as high congenital astigmatism, the meridians may not be perpendicular to each other.

Peripheral Zone

The peripheral zone is defined as the area from the peripheral margin of the apical zone to the central border of the limbus. This zone is approximately 7 to 11 mm diameter. Topographically, this is the area in which the normal cornea flattens most progressively and becomes more aspheric.

The peripheral curvature is of great importance when fitting contact lenses because it is the region of the cornea that supports the greatest area of the maximum contact with the lens. The contact lens should be fitted to the peripheral corneal curvature, where it obtains most of its support. This zone also plays an important role with regard to refractive surgery.

Limbal Zone

The limbal zone is defined as a rim 0.5-1.0 mm wide adjacent to the sclera. It is usually covered by the conjunctival vascular arcade, and its exact extent depends upon the amount of scleral override (normally, its size is approximately 12 mm in diameter). Because the cornea has a generally steeper radius of curvature than does the rest of the globe, there is an apparent sulcus at this juncture that defines the end of the cornea and the beginning of the sclera.

This region is also of significance because it is involved in many peripheral corneal thinning disorders, as well as being the common site for numerous surgical procedures.

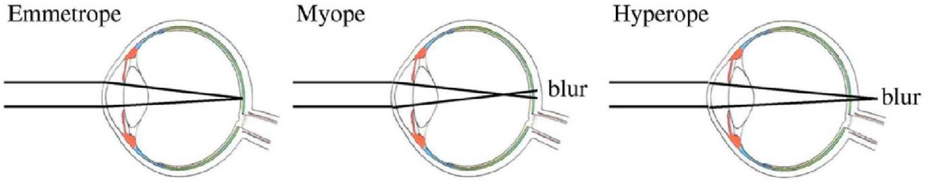

Fig. 2.9. A side view of an emmetropic, myopic and hyperopic schematic eye shown unaccommodated viewing a distant object. When all the components of the eye are properly matched, and the optical image coincides with the retinal plane, the refractive error is zero - this is emmetropia. In the case of an ametropic eye the parallel rays of light are not focused exactly upon the retina with eye in a state of rest causing the retinal blur. The myopic eye has too much optical power in relation to its length. The hyperopic eye is too short and has too little refractive power.

Surgical incisions or disease processes involving this region can indirectly change the central corneal topography and affect visual acuity.

2.6 Eye Classification

Ideally, when the eye fixates an object of interest, the image is sharply focused on the fovea. In paraxial optical terms, the object and fovea are conjugate. However, the object can only be focused sharply if it is within the accommodation range of the eye. If the accommodation range is inappropriate or too small, object of interest cannot be focused sharply on the retina. In these cases, the retinal image is out-of-focus or blurred, and visual acuity is reduced. The anatomical variables that affect visual acuity are also relevant to refractive error and image defocusing. For an image of a distant object to be in focus on the retina, the refractive power of the eye must match, in a sense, the axial length of the eye (or vice versa).

Defocused retinal images occurs also when the refractive power of the eye varies with meridian. This is commonly due to one or more refractive surfaces in the eye being toroidal, transversely displaced or tilted. There are now two pairs, one corresponding to each of two principal meridians. These errors are referred to as astigmatism or cylindrical refractive errors, in contrast to spherical refractive errors, which are present when the refractive error is the same in all meridians.

Eyes are generally classified into three categories: emmetropic, myopic, and hyperopic. A comparison of their vision when viewing a distant object is shown in Fig. 2.9. In addition, eyes may contain some astigmatism. An excellent characterization of these conditions is found in [19], and is briefly summarized in the following subsections.

2.6.1 Emmetropia

Emmetropic eyes are those which when relaxed, or unaccommodated, focus distant parallel light well onto the retina as shown in Fig. 2.9. The emmetropic eye is regarded as the ”normal” eye. For the emmetropic eye a far point of district vision is at infinity. A refractive anomaly occurs if the far point is not at infinity. An eye whose far point is not at infinity is called an ametropic eye. Ametropia indicates a not coordinated match between power of eye and its axial length resulting in the defocused image of a point source that is a blur circle, the size of which is proportional to the amount of refractive error measured in diopters. The departure from emmetropia is often considered to be an error of refraction, and ametropia is also referred to as refractive errors.

2.6.2 Myopia

Myopia, or nearsightedness, describes an eye which, when unaccommodated and viewing a distant object, focuses the light in front of the retina. This causes distant object to be blurred out, as shown in Fig. 2.9. However, as the object nears the eye, there is a distance M_R, called the far point, at which the unaccommodated eye sees in perfect focus. If the object is moved closer than that point, the eye simply accommodates to keep it in focus. As myopes age, they do not have that luxury, so their uncorrected eye can only see objects when placed at roughly M_R.

Myopia is caused when the cornea is too highly curved (i.e., it has too much refractive power), the axial length of the eyeball is too lang, or both.

2.6.3 Hyperopia

Hyperopia, or farsightedness, is the opposite of myopia, in that the unaccommodated eye formes distant light behind the retina (or at least the optical image would lie behind the retina, if the retina were not in the way). This also causes a retinal image that is out of focus for distant objects, as shown in Fig. 2.9. To compensate, the hyperope simply accommodates to focus the incoming light more and can see distant objects, unlike myopes. As the object is brought near the eye, the degree of accommodation increases correspondingly. As hyperopes age and lose that ability, they become seeing anything in perfect focus without spectacle or surgical correction.

Hyperopia is caused by a cornea which is too flat (i.e., the refractive power is too weak), or an eye which is not long enough, or both.

2.6.4 Astigmatism

Astigmatism can be defined as the refractive error in which no point focus is formed owing to the unequal refraction of light in different meridians. The astigmatism results in two separate and district foci, one for each principal direction of refractive curvature. Thus, a point source usually does not have a circular image, because the

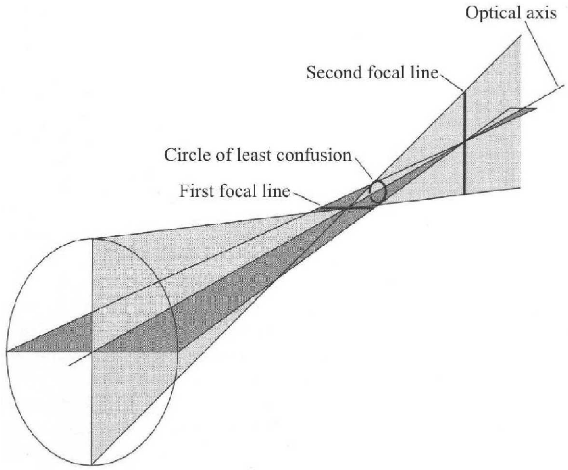

Fig. 2.10. There is no single plane of focus for an astigmatic optical system. Instead, the meridians of greatest and least power have focal planes defining a range of focus with a blurred "circle of least confusion", a midway between the extremes.

plane of focus varies from one meridian to the next[15]. The primary, or more curved direction comes to a focus first (Fig. 2.10). Then the secondary focus is reached farther back. At each of these foci the image from a distant point light source is a thin sliver, oriented with the principal curvatures. A midway between these two focal planes is a point where the point light source would be equally out of focus, and the blur is most circular: this is called the circle of least confusion. The amount of astigmatism is described as a degree of cylinder and its corresponding axis. It may originate from any rotational asymmetry or decentration of the optical surface of the system or irregularities in refractive index.

The most common cause of astigmatic error of the eye is due to the astigmatic curvature of the anterior corneal surface (Section 2.5). This may occur both physiologically and pathologically. The astigmatism of the anterior corneal surface is usually neutralized by inverse astigmatism of the posterior corneal surface or the lens.

In about 90% of eyes, the steepest meridian (meridian of greatest curvature) is the vertical meridian (within 30%). This is termed "direct" or "with-the-rule" astigmatism. The meridians of greatest and least power may be also something other than strictly horizontal and vertical (oblique astigmatism), or the meridians may not be orthogonal (bioblique astigmatism).

Additionally, it is distinguished between regular and irregular astigmatism. The regular astigmatism is where the refractive power changes gradually from one meridian to the next by uniform increments. In the case of the irregular astigmatism the changes in the curvature of the meridians are unequal and conform to no geometric pattern.

---

[15] Uncorrected astigmatism light distribution typically manifests itself as an oval smear on the image plane.

2.7 Correction of Refractive Errors

The ability of the eye to resolve images and distinguish form and detail can be affected by refractive errors. These optical defects caused by the elements of the eye - cornea and lens - degrade image quality, blur the image, or create a loss of visual acuity.

Whatever the cause of the refractive error, it can be corrected with appropriate ophthalmic lenses, which include spectacles, contact and intra-ocular lenses. There are also several surgical techniques to correct some of the refractive aberrations.

The most common is to pre-refract the light rays before they enter the eye with spectacles or contact lenses with the desired correction [39]. Only two kinds of the optical aberrations can be corrected by this way: sphere and cylinder. These aberrations called regular are the most common optical aberration affecting human vision. All other aberrations are called irregular and there is no standard way to correct them with spectacles or contact lenses.

Another way to correct refractive errors of the eye is corneal refractive surgery, which has become quite popular [3]. This surgical technique aims to change the shape of the cornea with either a scalpel or laser to correct the vision (the myopic cornea would be made flatter while the curvature of the hyperopic cornea should be increased by making it steeper).

Surgical reshaping of the corneal surface has shown the importance of knowing the shape of the cornea. Because the surgical procedure can also correct the irregular aberrations it follows that the nature of the surgical approach is aided by knowing the exact shape of the cornea that is to be modified [29].

2.8 Corneal Disorders

2.8.1 Keratoconus

Keratoconus (also called conical cornea) is an eye condition which results in the bulging and thinning of the cornea, as well as localized regions of high curvature (Fig. 2.11). The weakened tissue is forced to assume by the intraocular pressure on its posterior surface. The almost conical shape usually reduces a patient's visual acuity and is associated with very high myopia and astigmatism. The visual disturbance caused by keratoconus is mainly due to the irregular shape of the corneal surface.

2.8.2 Diplopia

Diplopia (more commonly known as ”Double Vision”) occurs when a patient fixates on a single object but perceives multiple objects. It is usually caused by problems with the muscles of the eye preventing a unique fused image from being formed.

Monocular diplopia is slightly different: the shape of the cornea of a single eye creates multiple images of an object. It is believed to be caused by corneal warpage, trauma or keratoconus. If a similar process occurs in both eyes (bilateral monocular

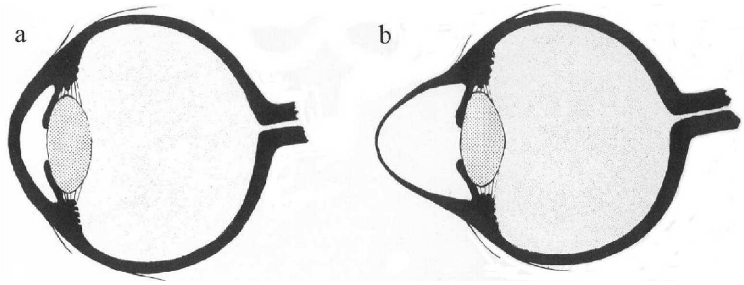

Fig. 2.11. Cross-section trough a cornea: **a** - a normal cornea, **b** - a cone-shaped cornea with the apex of the cone being forward represents keratoconus, the most common form of corneal bulging.

diplopia), that is, the doubling is still present with either eye covered, the patient may still only see two images. Seeing multiple images (polyopia) is rather rare.

CHAPTER 3

CORNEAL TOPOGRAPHY

In this chapter traditional technique and more recent methodology for measuring corneal topography are explained. The main goal is to present the basic terminology in corneal topography that will help to understand the data measured by any corneal topographer. The historical evolution of corneal shape measurements is also reviewed[1].

3.1 Historical Background

It has been known for over a century that the cornea is the main refractive element of the eye, and already early the ophthalmologists have tried to determine its topographic characteristics. This has not been a simple task given that the cornea possesses an aspheric surface that is not radially symmetric. These efforts have been led to the gradual development of instruments.

In 1619, Scheiner was the first to measure the corneal shape [40]. He observed that shiny glasses spheres of different radii produced reflected images of different sizes. He then produced a series of convex spherical mirrors of progressively larger curvatures and tried to determine corneal curvature by matching the size of the image reflected from a subject's cornea with the image produced by one of the calibrated spheres.

In the 1820s, Cuignet developed a keratoscope. In his system, a light was projected onto a target that was held in front of patient's eye. The light, target, patient, and observer were positioned in such way that the observer could visualize the reflected image of the target on the patient's cornea. Distortions of the reflected image, indicating abnormal corneal shape, could then be qualitatively interpreted by the observer. His major problem was in the alignment of the lighting, target, patient, and observer so that the image of the target was centered on the patient's visual axis. Additionally, the reflected image was viewed one-on-one ratio making it very difficult to see minor distortions in corneal shape.

---

[1] It is referred to the excellent review articles by Binder [4] and Levene [24] describing the development of technology for assessing corneal topography in details.

Fig. 3.1. Placido's disc.

Quantification of corneal curvature became possible in 1854 with the development of a keratometer (also called ophthalmometer) by Herman von Helmholtz [14]. It was the first true keratometer[2]. The distance measured between two pairs of reflected points gave the spherocylindrical curvature of the central 3 mm of the cornea in two meridians.

The Cuignet's problem was overcome in 1882 by Placido, who placed an observation hole in the center of the target [36]. His target was a disc with alternating black and white concentric rings that had a hole in its center through which the observer could visualize the patient's cornea (Fig. 3.1). This was crucial for improving target alignment with the patient's visual axis. Not only could the observer grossly center the target on the patient's cornea, but the patient was also able to directly align his or her visual axis with the center of the target disc. This technique is the origin of Placido disc-based systems that are the basis of many topography systems commonly used today.

This technique, while providing a visual representation of the corneal surface, does not provide quantitative information. Although Placido's disc certainly ameliorated the problem with target alignment, the observer still had no magnification capabilities and was incapable of detecting small degree of corneal topographic distortion.

The issue of magnification was addressed by Javal. In 1889, in order to extend the area of cornea that could be analyzed, Javal attached a Placido-type disc to his keratometer. The benefit of this system was that the ophthalmometer had an eyepiece telescope system that magnified the observed keratoscopy image. He realized the need to "fix" the image and measure the size of the rings, but this was not practical until 1896, when Gullstrand applied photography to keratoscopy and captured the reflection on film. So the first photokeratoscope was developed [**?**]. Numerous attempts were made to quantify keratographs by comparing them to photographs of spheres of known radius of curvature, but all methods were laborious, very time consuming, and not

---

[2] To learn the principle of operation of an ophthalmometer, see Section 3.2.2 or [53].

really practical. This was the main reason that, until quite recently, the assessment of corneal topography was almost totally confined to keratometry.

In the 1970's, several photokeratoscopes were designed with attached Polaroid camera. In 1981, Rowsey et al. reported a modified photokeratoscope, called the Corneascope, which used a "Comparator" allowed fast, in-office evaluation of the Polaroid keratograph to determine the corneal radius of curvature [37]. Rowsey and coworkers developed some of the earliest methods to provide quantitative information from photokeratoscope images by comparing the mire diameter from corneas to those reflected from standard reference spheres and by measuring hemichord length from the center of the mire pattern to each keratoscope ring along several hemimeridians. Doss et al. introduced a mathematical technique to determine the corneal profile from keratoscopic images [11]. A little bit later Cohen developed statistical indices to describe the geometrical distortions of the reflected mires [6].

Little progress was then made until the interest was renewed by the introduction of contact lenses. But perhaps the factor most responsible for the resurgence of interest in corneal topography has been the introduction of microsurgical and refractive technique when interest turned to the optical power provided by the cornea. As the visual results of refractive procedures have improved, fine-tuning of the refractive outcome has become increasingly important. It became necessary to have information about the shape of the whole corneal surface with great details and accuracy. This was first possible with the explosion of video and computer technology. The computer analysis applied to the data opened the way for detailed mathematical analysis of corneal shape.

Corneal topography as we know it now became available in 1984, when Klyce combined computer analysis and digital imaging into the videokeratoscope [23]. Since then computerized topography (videokeratography) has continued to be an evolving technology providing very fast, detailed, and precise corneal topography. This technique is now widely available and is the most commonly used in clinical practice today. Additionally, Klyce refined Doss algorithm by using statistical methods to reduce errors inherent in manual digitizing [23]. Interpretation of the shape anomalies and clinical utility were augmented with the adding of color coded topographic maps by Maguire in 1987 [31]. And recently, Wilson introduced recommendations to the scales to evaluate color coded maps [52].

The more recent explosion of refractive surgery has also opened up new avenues for the development of topographic systems. As results, new topography systems based on the principle of projection rather than that of reflection have been developed and marketed. Additional instruments that use interferometry or raster stereography for reconstructing the corneal surface have been reported.

3.2 Methods for Measuring Corneal Topography

This section describes several techniques for measuring corneal topography.
In Tab. 3.1 some available corneal topographers are listed.

Tab. 3.1. Some currently available corneal topography systems.

Type	Name of unit	Provider
Placido-based systems	ATLAS	Humphrey Systems
	EyeSys 2000	EyeSys Technologies, Inc.
	TMS-2N	Tomey Corporation
Slit Scanning Photography	Orbscan II	ORBTEK, Inc.
Raster photogrammetry	PAR CTS	PAR Technology Corporation
Interferometric	ET-800	Euclid Systems Corporation
Laser Holographic Interferometry	CLAS-1000	Kerametrics Corporation

3.2.1 Basic Principle for Measuring Corneal Topography

From an optical perspective, the cornea is similar to a convex mirror. This fact is used by the most instruments measuring corneal topography.

Let O be the size of an object, placed at a distance o in the front of a convex mirror of radius r (Fig. 3.2). The magnification m produced by the mirror is the ratio of the image size I to the object size O, and this is in turn proportional to the ratio of the distances of the image and of the object from the mirror

$$m = \frac{I}{O} = \frac{a}{o}\,,$$

where a is the image distance from the mirror, and o is the object distance from the mirror.

Due to the comparatively small radius of curvature of the anterior corneal surface, the image is located very close to the focal point F, which lies halfway between the anterior corneal surface and the center of curvature C. To a first approximation, the image distance from mirror may be taken to be equal to half the radius of the curvature of the mirror $a \approx r/2$. Substituting

$$I = O\frac{r}{2o}\,.$$

From this equation the radius of curvature is obtained as

$$r = 2o\frac{I}{O}\,. \tag{3.1}$$

Therefore the magnification of the image can be used to determine the radius of curvature of the anterior surface of the cornea.

Clinicians think of curvature in terms of diopters (D). The radius of curvature r_{Cornea} can be converted into the refractive power of the cornea P_{Cornea} because of simple relationship between them by the following equation

$$P_{Cornea} = \frac{n_{Cornea} - n_{Air}}{r_{Cornea}}\,, \tag{3.2}$$

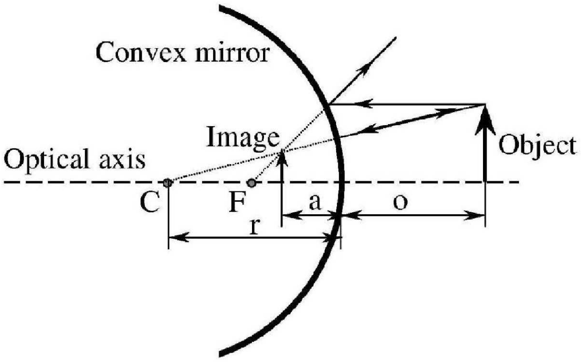

Fig. 3.2. Image formation by a convex mirror. The image can be constructed using two rays starting from the top of the object: a ray going parallel to the optical axis and being reflected away from the principal focus F and a ray passing towards the center of curvature C and then back along its own path.

where n_{Cornea} and n_{Air} are the refractive indices of the cornea and the air, respectively.

For any case, the refractive index of the air n_{Air} is 1, and the anterior corneal curvature r_{Cornea} is measured by keratometer or corneal topographer. For the refractive index of the cornea n_{Cornea} there are two possibilities (Tab. 2.1). The first one is to use the refractive index of the anterior corneal surface (corneal index of refraction) which is 1.376. The second possibility is to set the refractive index of the cornea to the refractive index of the entire cornea (Standard Keratometric Index or SKI) which value represents a combined refractive index for the anterior and posterior corneal surfaces and is 1.3375[3]. In clinical practice, the standard keratometric index is used to calculate the corneal refractive power from the radius of curvature. Therefore

$$P_{Cornea} = \frac{SKI - 1}{r_{Cornea}} = \frac{0.3375}{r_{Cornea}}, \tag{3.3}$$

where the radius of the curvature r_{Cornea} is expressed in meters. Or, if the radius of curvature is expressed in millimeters rather than meters

$$P_{Cornea} = \frac{337.5}{r_{Cornea}}. \tag{3.4}$$

It should be noted, that the calculation of the refractive corneal power is performed using paraxial formulas (Eq. (3.1)), which is acceptable only for small central area of

---

[3] The standard keratometric index (SKI) is a combined estimate of the posterior corneal curvature and the refractive indices of the cornea and the aqueous. This concept is a simplification ignoring the fact that the refracting surface is air-tear interface, and it does not account for the oblique incidence of incoming light in the corneal periphery. As a result, it miscalculates a true corneal refractive index of 1.376 to 1.3375 to correct some of these factors. That is the way those diopters more correctly are termed as keratometric diopters to distinguish them from the diopters expressing more precisely the true refractive power at certain corneal power. Most commercially available instruments convert the radius of curvature to dioptric power using the standard keratometric index.

the cornea, where this paraxial approximation is valid. Out of this area the Snell's low must be used

$$P = \frac{n}{f}, \tag{3.5}$$

where f is distance from the corneal surface to the point, where the parallel rays pass through the optical axis, and n is the refractive index of the cornea.

3.2.2 Keratometer (Ophthalmometer)

Until the mid 1980s the most common clinical method for monitoring corneal shape was keratometry.

Keratometer (also called ophthalmometer) is an optical instrument used to determine the radius of the anterior corneal surface along one meridian. It was first described by Herman von Helmholtz in 1854 [14].

The principle of operation of a keratometer involves an assumption that the anterior corneal surface behaves as a convex mirror (Section 3.2.1). The mires of the keratometer form an image that is reflected from the anterior corneal surface. Using Eq. (3.1) based on the theory of reflection from a convex mirror, one can then determine the radius of curvature of the anterior corneal surface.

Eq. (3.1) shows that the radius of curvature r is proportional to the image size I and is inversely proportional to the object size O. Thus, there are two general methods by which these operation principles may be used to derive radius of curvature, and so there are two types of keratometers[4]. One method uses a variable object size O and a fixed image size I; and this is the method used by the Javal-Schiotz keratometer. The second method involves a fixed object size O and a variable image size I; this is the method used by the Helmholtz keratometer.

By Javal-Schiotz keratometer the object size is varied to achieve a predetermined image size. This type of keratometer uses two colored mires (along a graduated arc) that are able to be moved closer together or further apart, adjusting the size of the object until the distance between the images of the mires has a predetermined size. At this point the image size is known, and the object size can be measured. Then the radius of curvature can be calculated, and corneal dioptric power deduced.

By Helmholtz keratometer (as utilized by the Bausch & Lomb keratometer (Fig. 3.3)) the image size is measured if the object size remains constant. Two reference marks[5] with known distance are projected on the cornea. The distance between the images of these two marks on the corneal surface is measured to determine the radius of curvature in that meridian, based on the assumption that the corneal surface is spherocylindrical (Eq. (3.1)). Then the marks are rotated by 90°, and the measurement is repeated in this new meridian.

---

[4] In all keratometers the distance of the object from the corneal surface is constant (i.e., o=const in Eq. (3.1)), being the focal distance of the viewing telescope.

[5] The marks differ depending on which keratometer is used. As an example the marks of the keratometer manufactured by Bausch & Lomb is presented in Fig. 3.3.

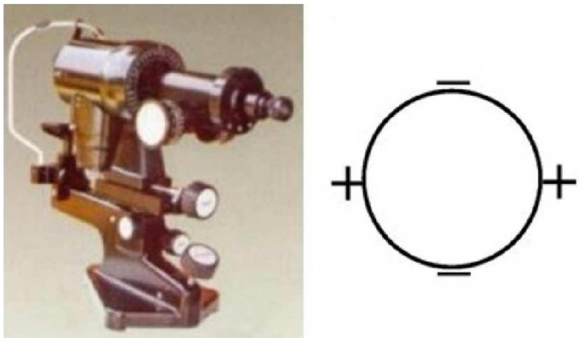

Fig. 3.3. The keratometer manufactured by Bausch & Lomb and its marks.

The keratometer has the capacity to measure a regular surface with an accuracy of better than 0.25 diopters.

Keratometry provides only a limited amount of information (the sphere and regular astigmatism for two orthogonal meridians) about the shape of the small area of central optical zone of the corneal surface about 3 mm in diameter. The curvature changes occurring over this region and the peripheral flattening of the cornea are ignored. Additionally, the keratometer provides no information regarding the topography central or peripheral to the points of measurement, and mild corneal surface irregularity causes mire distortion that precludes meaningful measurements.

The limitation of the keratometer is also the assumption that the cornea is symmetric around the visual axis and has a spherocylindrical surface with a single radius of curvature in each meridian and major and minor axis of curvature separated by 90°. However, the normal cornea is aspheric and flattens from the center to the periphery. Thus, even for normal corneas, the keratometer provides a curvature that may be flatter centrally and steeper peripherally than the true topography.

The keratometer is also not useful if the cornea varies from the spherocylindrical shape, what is the case after surgical procedures or by keratoconus and others corneal abnormalities, because no corneal irregularities or deformations of the corneal shape can be assessed, however.

3.2.3 Videokeratoscopy

Videokeratoscopy (also called videokeratography) represents a significant advance in the measurement of corneal curvature over keratometry and provides much more details about curvature variations over a large portion of the corneal surface than the keratometry[6].

The videokeratoscope contains a target, an imaging system (an objective lens and a camera), and a computer system. The target is a disc or cone (modified Placido

---

[6] Most corneal topographers evaluate 8000 to 10000 specific points across the entire corneal surface. By contrast, keratometers measure only four data points within the cornea's central 3-4 mm; the small size of this area can lead to errors in determining precise toricity.

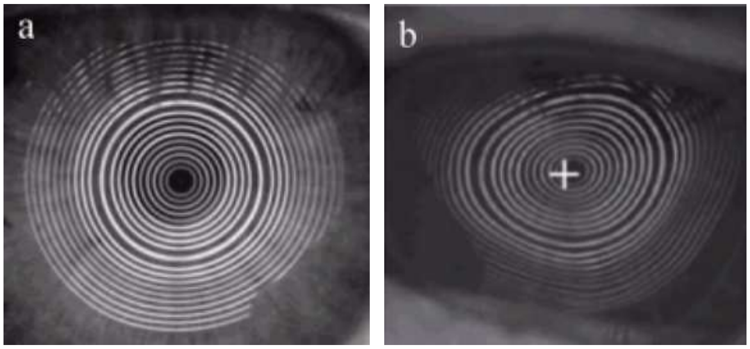

Fig. 3.4. An image of the videokeratoscopic mires on a human cornea: **a** - on a normal cornea, **b** - on an astigmatic cornea.

disc) consisting of a set of concentric circular rings[7]. When the disc is placed in front of the eye, the illuminated rings are reflected by the corneal surface that acts as a convex mirror and forms a virtual image of target that is captured by a video camera positioned at the videokeratoscope axis. The position, size, and spacing of the rings in the reflected image are determined by the corneal shape. This two-dimensional image is digitized and exported to various computer software program for rapid quantitative analysis.

If the cornea is spherical, the rings appear round and regularly spaced (Fig. 3.4a). But the reflective mires are closer together and narrower in areas of steeper cornea (it indicates a greater refractive power of the cornea compered to that of a sphere), and father apart and wider on flatter parts (it shows a less refractive power than that of a sphere). If the cornea is oval or corneal astigmatism is present to more than a minimal degree (0.5 D), it will change reflected circles to an elliptical shape, with the steep axis of the cornea corresponding to the minor axis of the ellipse where rings appear closer together (Fig. 3.4b). Localized changes, as irregularities of the surface, will cause distortion of the mires in the area of the cornea where they are available.

An algorithm[8] incorporating a number of approximations is used to reconstruct three-dimensional shape of the cornea from two-dimensional photokeratoscopic image based on the geometry of the videokeratoscope. The size and distortion of the rings on the cornea are starting point for reconstruction of the corneal shape. The radial distance is derived from the position of the rings regarding the center of the mires cone. The radius of curvature is obtained from the size and spacing between the rings. The corneal topography is then displayed in a clinically-useful format (Section 3.3).

This technique has certain limitations which reduce their clinical usefulness. First, to get the "true" surface information, the measured slope date must be integrated for

---

[7] The number of rings, its thickness, color, and position of the rings relative to each other vary from system to system.

[8] Actual algorithms used by the commercial instruments are closely guarded secrets. They may not be the same as those that appear in the open literature.

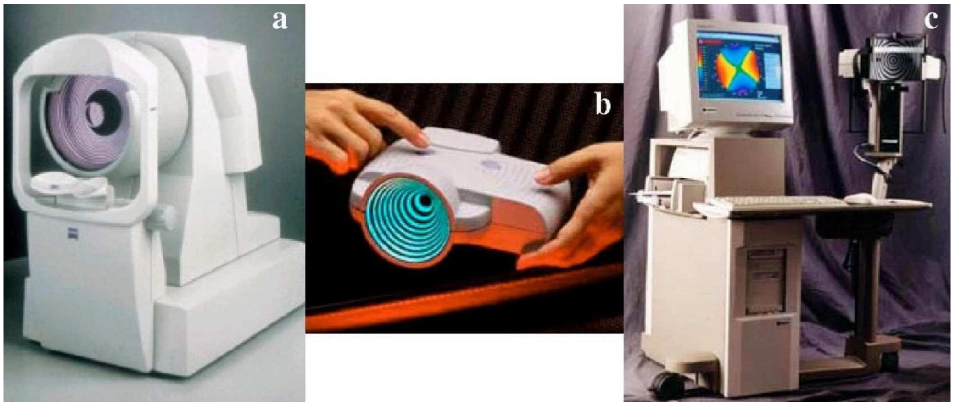

Fig. 3.5. Several videokeratoscopes: **a** - ATLAS, **b** - EyeSys Vista, **c** - ORBSCAN II.

calculation of corneal height. This integration process is biased by assumptions about the corneal shape. Second, these systems will not work on corneas which do not have the necessary qualities to reflect an image of the disk due to conditions such as epithelial defects, scarring, or highly irregular shape. In addition, these systems are sensitive to image centration and focusing errors.

Videokeratography provides both a qualitative and quantitative evaluation of corneal curvature. Although the field of measurement is extend to the corneal periphery and is about 8-10 mm in diameter, only limited information about the most central portion of the cornea (1.5 mm or more) is provided because that area is not covered by the mires. These devices do not have mires at the central zone because a camera is placed in the center of the rings, and the rings cannot be made arbitrarily small in diameter. Thus, the extrapolation and approximation of data in this region is required. The used mathematical models such as spheric, aspheric, conic, and toric models are suitable for normal cornea but can be the error source in the case of abnormal or postoperative cornea.

The accuracy and reproducibility of the videokeratoscope is within 0.25 D.

Placido-based videokeratoscopes comprise the vast majority of the units used in clinical practice today (Fig. 3.5).

3.2.4 Raster photogrammetry

Raster photogrammetry (or raster stereography) is a method of obtaining topographic information using a stereotriangulation technique [48].

In these systems a raster stereographic grid is projected onto the corneal surface, and a camera captures the image of the grid from a known angle. Because the cornea is a transparent nondiffusing surface, the projected grid is not visible unless a diffusing material is used to provide a surface on which an image can be visualized. Therefore these systems require a small amount of fluorescein dye to be placed as a thin film

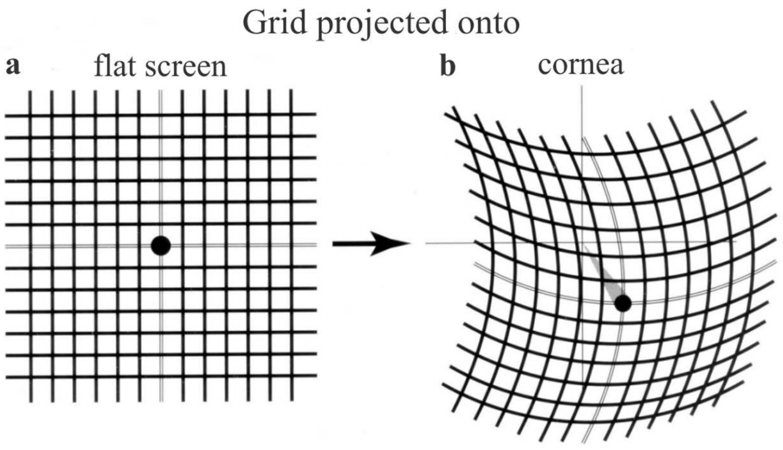

Fig. 3.6. Diagrammatic representation of the measurement of corneal height by raster photogrammetry [8].

on the corneal surface. The flash illumination passes through a cobalt blue excitation filter causing the stained corneal tear film to fluoresce in an alternating light and dark grid pattern. This image is then viewed by the video camera and digitized for analysis.

The position and separation of the grating lines on the cornea provide information for determining the corneal topography. A computer calculates the topographic elevation trigonometrically by comparing the displacement and distortion of the projected grid components on the cornea to their known positions when the grid is projected onto a flat surface (Fig. 3.6).

The projected image covers the full cornea, including the central optical zone and the limbus, thus, the elevation data over the whole cornea can be created.

One advantage of this technology seems to be that this methodology does not require a smooth reflective surface (i.e., an intact epithelium), because it relies on projection of the grid onto a film of fluorescein rather than on reflection from the tear film. Thus, it is not affected by surface defects and irregularities and, therefore intraoperative use of this methodology is possible. Images from corneas with irregular or nonreflective surfaces can be also obtained. But because only the thin film of surface fluorescence is photographed, this system cannot measure the actual anterior surface of the cornea. Also, pooling of fluorescence may be a reason for image distortion. Additionally, the use of the fluorescein is not ideal, because it is not sufficiently known if it affects the thickness and the distribution of the tear film on the corneal surface.

The number of data points used by this method is initially limited by the number of grid intersection. A far greater number of data points can be obtained if the lines of the grid have a sinewave function, and the grey-scale value of each pixel is measured to detect local changes in grating intensity.

The PAR Corneal Topography System was the first topography system used this methodology [2].

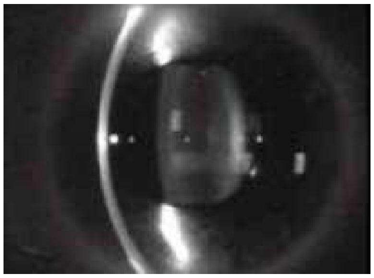

Fig. 3.7. A slit of a human eye with the slit-lamp.

3.2.5 Slit Scanning Photography

Slit scanning photography (also called scanning slit topography or scanning slit imaging) uses a scanning slit-beam and direct stereotriangulation to measure the anterior corneal surface [55]. The mathematical computation and the technique of direct stereotriangulation are similar to that of the raster stereography.

When observing the cornea on the slit-lamp using a narrow beam, the shape of the anterior and posterior corneal surface can be seen in one meridian due to the curved appearance of the beam (Fig. 3.7). The projected beam of light produces diffuse reflection from the cornea that is detected by a camera. If a slit beam scans across the cornea, a series of 40 independent images (20 slits to the right and 20 to the left) can be recorded from a known angle by a calibrated video camera positioned at 45 degrees to the right and to the left of the video axis. Then those series of the cornea "slices" are overlapped to reconstruct the corneal shape.

One exam provides multiple diagnostic data - including topography of anterior and posterior corneal surfaces and full corneal pachymetry[9] over the entire cornea.

Slit scan imaging is not based on spherical assumptions that can distort or misrepresent data. The system is tolerant of focus and centering errors because the measurements are independent of the relative position of the instrument. The main limitation of this technology is the relatively long time needed to image each slit individually (0.8-1.5 seconds) and the resultant possibility of introducing artefacts due to eye movements[10].

The only one available system using this method is Orbscan manufactured by Orbtek [55].

3.2.6 Moiré Interferometry

Moiré interferometry is an easy and precise measurement of the configuration of three-dimensional objects [45].

---

[9] Pachymetry is a measurement of the corneal thickness.

[10] During the examination the patient fixes on a light source, whose reflex is aligned with the instrument axis. An "eye tracking" software attempts to minimize the influence of involuntary eye movement during an examination.

Moiré interference occurs when two set of parallel lines are superimposed at direct orientations. When two parallel gratings are projected onto a surface from different angles, the image on the surface is a series of curved lines (Fig. 3.8). Grating projected from the left and right sides produce images curved in opposite directions. Addition of these two images results in moiré interference which generates ring-shaped interference fringes visible on the corneal surface. The fringes follow contour lines representing points of equal height and can be viewed directly on the cornea without any recourse to mathematical assumptions or computations [18].

The width of the moiré fringes is partially determined by the spatial frequency of the gratings. Their orientation is dependent upon the relative orientation of two grating images and therefore upon the shape of the surface on which they are formed. The number of contour lines produced is dependent upon the frequency and angular displacement of the gratings used. As with raster stereography, if the gratings have a sinewave function, a huge number of data point can be generated.

The fact that the moiré technique can be used on a diffusing and opaque surface makes it difficult to generate moiré fringes on the cornea because the cornea is a transparent structure reflecting the light specularly on its surface. Therefore the moiré contours on the corneal surface can be generated only with some kind of surface coating - the instillation of a fluorescein solution on the cornea. This way, the contour map can be directly obtained using the moiré fringes.

Using this methodology, the corneal shape can be measured even on the corneal periphery (with a very high resolution in the z-axis being $5\,\mu m$ [7]). And this can be done in the case of normal cornea as well as abnormal irregular cornea whose shape cannot be expressed mathematically.

3.2.7 Laser Holography Interferometry

These systems utilize laser holographic interferometry fringe pattern to depict deviation of the corneal surface from a sphere by recording of an interference pattern generated on the corneal surface by the interference of two coherent wavefronts. Two wavefronts may be generated by light from separate illuminating and reference laser, or the light from an illuminating laser may be directed through two distinct optical pathways using a beam splitter.

The light of a laser diode (a spherical wavefront) is projected onto the corneal surface, and the reflected light is captured by a camera. The interference of the illuminating and the reflected beam consisting of two frequency bands, the sum and the difference frequency, is imaged by a CCD chip via a beam splitter. The phase of the difference frequency signal characterizes the aberration of the wavefront, indicating the differential height between "best-fit sphere" and actual corneal height. By varying the working distance the system can be adapted to different "best-fit sphere". By analysis of the reflected wavefront towards the reference wavefront the three-dimensional corneal shape (i.e., the deviations from a spherical surface) can be reconstructed. The result is a three-dimensional surface map without interpolation.

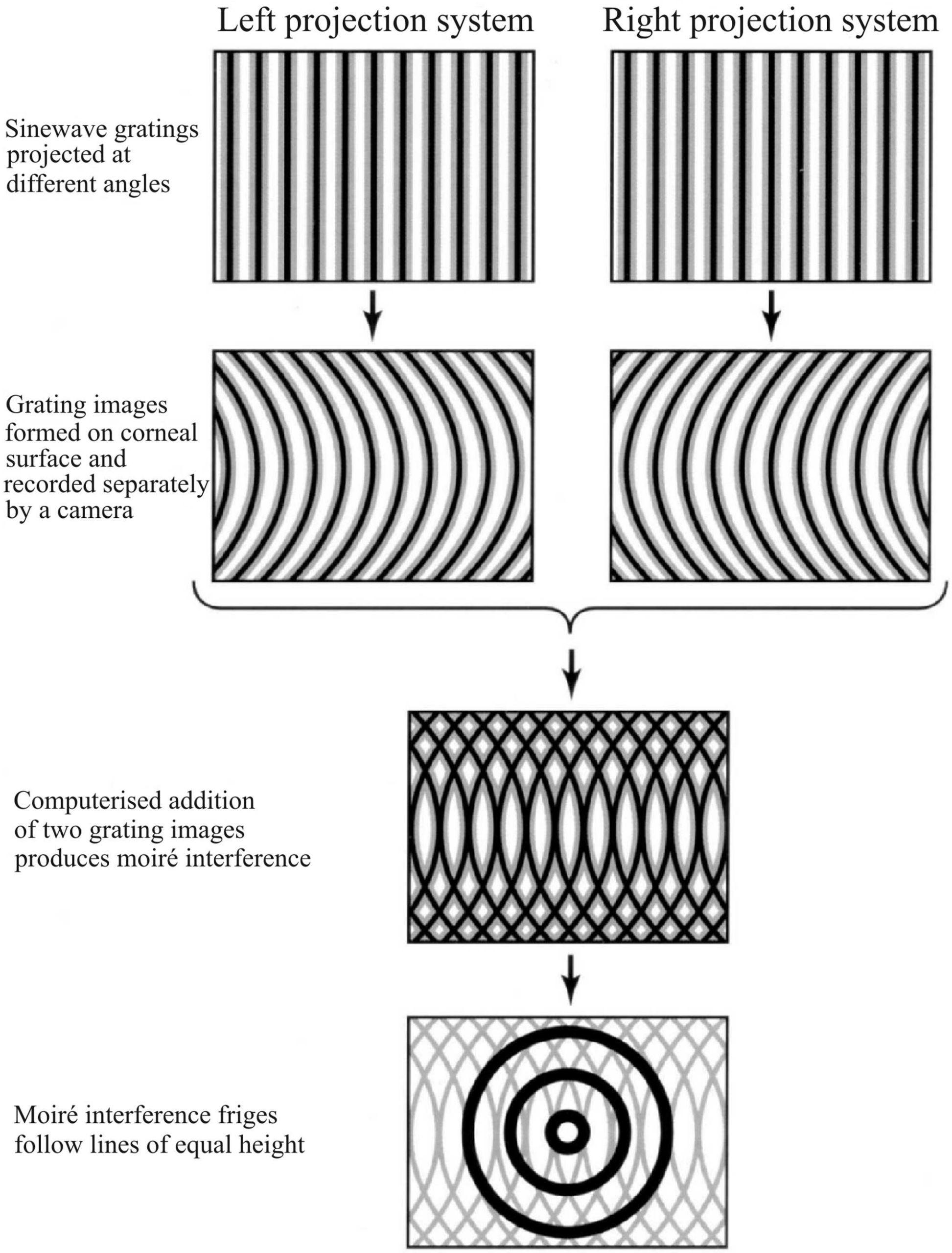

Fig. 3.8. Schematic diagram of generating moiré contour fringes on a surface [8].

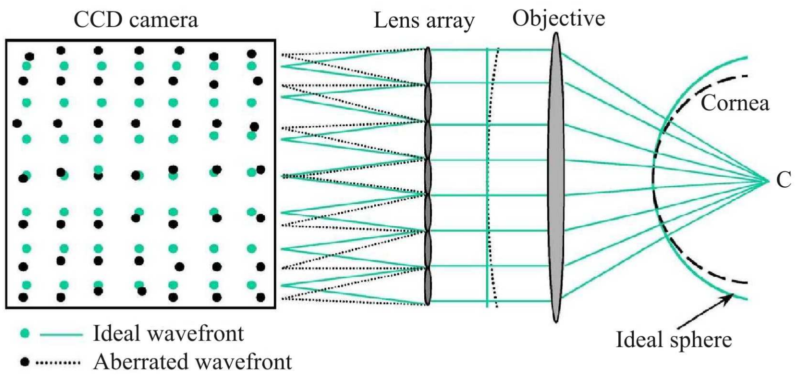

Fig. 3.9. The principle of the corneal topography measurement using a Hartmann-Shack wavefront sensor.

The density of data points generated is dependent upon the wavelength of the light.

One major advantage of this methodology is the high resolution in detection of differences to a spherical surface. Disadvantages are that an excellent centration of the cornea is necessary, and there are limitations in highly aspheric or irregular surfaces because of the periodicity of the phase signal.

3.2.8 Wavefront Analysis with Hartmann-Shack Wavefront Sensor

This method is presented in details in Chapter 5. Here only a short description follows.

Fig. 3.9 shows the principle of a Hartmann-Shack wavefront sensor (HSS) applied to measure the corneal topography. A laser beam is focused by an objective in such way that the center of the corneal curvature C lies exactly in the focal point of the objective. If the corneal surface is perfect spherical, the laser beam is reflected back onto itself at every point on the surface. If it is not the case, and the corneal shape varies from a perfectly sphere, the laser beam is reflected in other direction on locations where there are the differences. The information about the differences in the elevation of the shape are "saved" in the phase of the wavefront. The light reflected from the cornea falls on a lens array. Every micro lens of the lens array focuses the subbeam on a CCD chip lying behind in the focal plane of the lens array. A spot pattern seen on the CCD camera is imaged and analysed (Fig. 4.3). From replacements of the spots toward the reference (a spot pattern from a perfectly spherical surface) the wavefront can be reconstructed, and then the corneal elevation can be calculated.

The area measured on the cornea depends on the optics used (Section 5.4). The advantage of this method is that the optically important cental zone of the corneal surface is also measured directly. But requirements on the optics of the system are very high, because optical aberrations of the system affect the spot pattern quality (Section 5.4). The exact positioning of the corneal surface is also difficult.

3.3 Displaying Corneal Topography

After calculations have been done, and the corneal shape has been reconstructed, the data regarding the corneal topography can be presented in any of several ways depending on the individual patient requirement and user preferences. Each different display presents the information differently.

In this section types of maps, how they are calculated and displayed, and also some important definitions of statistical indices are explained. They answer critical questions about how well and in what regions the cornea focuses light coherently onto the retina and provide an approximation of what the patient actually sees.

3.3.1 Maps

Topographic information is commonly presented as a map in two dimensions (X and Y). The third dimension (height, curvature, refractive power, elevation etc.) is encoded in a color scheme that the areas with the same values are depicted in the same color. The color schemas vary from system to system, that sometimes makes a direct comparison of the data difficult. Normally, warm colors (red, orange, yellow) represent steeper areas of the cornea (i.e., small radius of curvature), while cool colors (blue, violet) mark the flatter portions (i.e., large radius of curvature). Green detects intermediate values. But an interpretation should never base on color alone.

Scaling is another important consideration with corneal topography. The normalized and absolute scales are the most popular.

In most topographers, the user can utilize the auto-size (or normalized, relative) scale. This strategy essentially subdivides the cornea being examined into dioptric intervals based on its actual curvature range (usually a 0.4 D to 0.6 D range per color). Actual colors are not specific to a dioptric value when using the normalized scale, but rather are relative to that particular patient's eye.

By contrast, the absolute (or standard) scale assigns a specific color to each dioptric value and constrains the data to fit within that range. This strategy allows clinicians to directly compare images from different eyes or from significant curvature changes in one eye (e.g., pre- vs. postoperative refractive surgery status). The downside of using the standard scale is that the dioptric range is greatly expanded; hence, clinically significant irregularities may become somewhat obscured when comparing eyes with very different curvature readings.

Clinically, it is probably best to use normalized maps when evaluating one particular eye and use standard maps when comparing two different eyes or comparing the same eye over time.

Maps come in several basic types: curvature maps, refraction power map, elevation map, and (ir)regularity maps. Each map reveals something different about the cornea and can have different degrees of sensitivity and specificity according to the pathology or condition of an eye being observed. No one particular map is always the "best" or "most accurate", but all of these maps combined give clinician an overall perspective

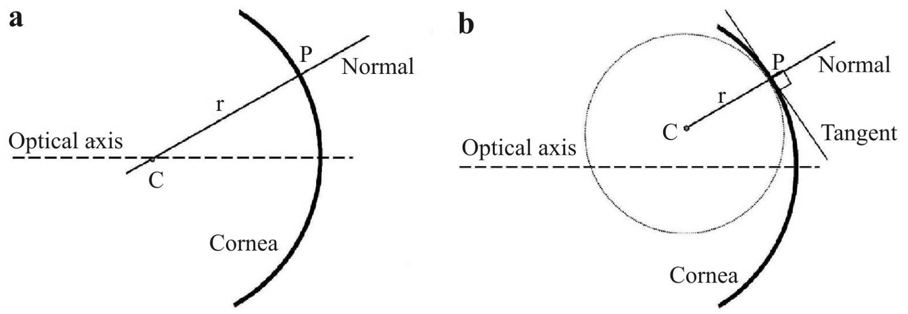

Fig. 3.10. **a** - The axial map calculation. **b** - The tangential map calculation.

about the curvature, refractive potential, shape, and optical quality of the corneal surface. A lot of another numerous displays, including difference map, ray tracing display, astigmatic analysis, are available. Displays discussed below represent those most commonly used in clinical practice.

Axial Map

Axial map shows the global (or sagittal) radius of corneal curvature with the assumption that all light rays striking the corneal surface from infinity are being refracted at the same angel, explaining why this map is sometimes referred to as "spherically biased" map. Its downside is its tendency to ignore minor variations in curvature.

For calculation of the axial radius of curvature the normal at every point of interest P of the corneal surface is determined (Fig. 3.10a). The spherical bias in the calculation stems from the fact that this normal to the point of interest passes through the optical axis of the corneal topography system. From this point C the distance r along the normal from the point of interest P to the optical axis defines the local radius of curvature at that point of the cornea.

Axial map is a simple way of describing the overall shape of the cornea and is most common to users of corneal topography systems.

Tangential Map

Tangential map is another type of curvature map. It shows the instantaneous (or local) curvature.

The calculation of the curvature is based on a tangent to the normal without a constraint that the center of rotation fall on the optical axis of the topography system.

The location of the center of curvature for each point of the interest P is calculated by a best fit line normal to the tangent, while the distance along the normal from the point of interest on the corneal surface to the local center of curvature C defines the local radius of curvature r at that point of the cornea (Fig. 3.10b).

Mathematically, this algorithm is more alike the standard mathematical definition of the radius of curvature. The calculation has less spherical bias because curvature is

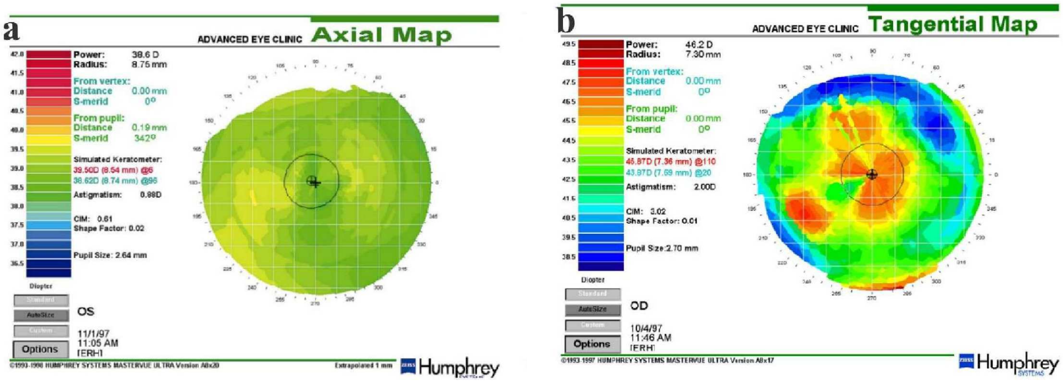

Power: 38.6 D
Radius: 8.75 mm
From vertex:
Distance 0.00 mm
S-merid 0°
From pupil:
Distance 0.19 mm
S-merid 342°
Simulated Keratometer:
39.50D (8.54 mm) @6
38.62D (8.74 mm) @96
Astigmatism: 0.88D
CIM: 0.61
Shape Factor: 0.02
Pupil Size: 2.64 mm
OS
11/1/97
11:05 AM
[ERH]
©1993-1998 HUMPHREY SYSTEMS MASTERVUE ULTRA Version A8x20
Extrapolated 1 mm

Power: 46.2 D
Radius: 7.30 mm
From vertex:
Distance 0.00 mm
S-merid 0°
From pupil:
Distance 0.00 mm
S-merid 0°
Simulated Keratometer:
45.87D (7.36 mm) @110
43.87D (7.69 mm) @20
Astigmatism: 2.00D
CIM: 3.02
Shape Factor: 0.01
Pupil Size: 2.70 mm
OD
10/4/97
11:46 AM
[ERH]
©1993-1997 HUMPHREY SYSTEMS MASTERVUE ULTRA Version A8x17

Fig. 3.11. **a** - Axial map of a cornea. **b** - Tangential map of a cornea. Warm colors such as red and orange show steeper areas; cool colors such as blue denote the flatter areas; green represents mean radius of corneal curvature. Important note: these maps represent not the same cornea.

calculated for individual small group of points without reference to the visual axis or the overall shape of the cornea. Therefore there is a greater accuracy in the periphery of the cornea and a better representation of local irregularities. In fact, it is the map that more closely represents the actual curvature of the cornea over the axial map. It does not assume the eye is spherical and does not have as many presumptions as the axial map regarding corneal shape.

Compared with axial map, tangential map is more sensitive to local or immediate change on the corneal surface. Tangential map also offers a better visualization of the precise location of corneal defects. This view is most useful in following trends in the post-surgical or pathologic eye. The tangential map is also best used in identifying or locating a corneal pathology, where the exact apex of the cone can be established.

Axial and tangential maps can give the value of the radius of curvature in meters or diopters, although these two values are intimately related (Eq. (3.3)) (Fig. 3.11).

Refractive Map

Refractive map (also sometimes called power map or Snell's law map) shows the refractive power of the cornea in its refractive state, measured in diopters. This map applies Snell's law to calculate the cornea's actual refractive power (Eq. (3.5)). Taking into account spherical aberration, the refractive map more closely illustrates how light rays behave as they strike an aspheric surface, such as a human cornea (Fig. 3.12).

Refractive power map may differ from axial map in their reading of power and radius. The biggest difference can be seen in the periphery and on eyes that have unusual or abnormal shapes. This is due to the effect of the spherical aberration that the refractive power map takes into account.

Clinicians use refractive map to evaluate visual performance of a postoperative

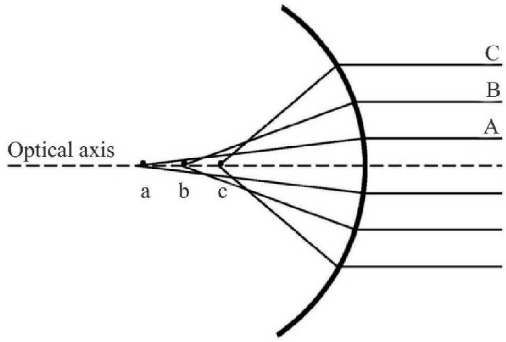

Fig. 3.12. Demonstration of spherical aberration. A surface with increasing refractive power from the center to the periphery: If parallel light rays pass through a surface from infinity they are refracted: Ray C crosses the optical axis at the shortest focal distance, *c*, and thus, it has the greatest refractive power. Rays B and A have longer focal lengths, *b* and *a*, respectively, and therefore have the least refractive power.

patient or the result of a refractive surgical procedure. This map is useful in understanding the effect of surgery and the optical properties of the cornea and identifies central islands in patients who have undergone PRK or LASIK.

Elevation Map

Elevation map gives information about how the cornea departs from sphericity. This map describes the difference in height (or elevation) of the cornea, in microns, from a reference spheric surface[11]. When displaying elevation map, the software chooses a surface that will be the "best fit" for a particular corneal surface. The software then attempts to fit, or superimpose, this model[12] onto the corneal surface, measuring the difference between the model and the real corneal surface.

Fig. 3.13 illustrates the basis for the elevation map calculation. Elevation can be measured as difference in height from a reference surface as positive or negative microns. The reason for this is that the corneal surface can fall above or below the best fit reference sphere. Positive elevation measurements indicate that the corneal surface rises above the reference sphere at that point, while negative measurements show that the corneal surface is below the reference sphere. If the cornea is perfectly spherical, the map would be an uniform shade of one color (Fig. 3.14a).

This map is most useful in predicting fluorescein patterns with rigid lenses. Higher elevations represent potential areas of lens bearing, while the lower areas will likely show fluorescein pooling.

---

[11] Different manufactures use either an aspheric surface as reference.

[12] This reference model varies from patient to patient.

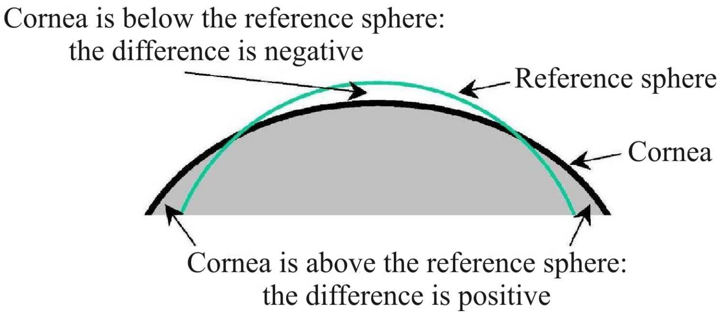

Fig. 3.13. The elevation map calculation. An elevation map shows differences in height between a corneal curvature and a computer-generated reference surface.

Irregularity Map

Irregularity map (also called distortion map or surface quality map) shows the amount of surface irregularity on the cornea and uses the same technique as the elevation map to obtain this information, expect it takes the best fit surface methodology one step further. It uses a best fitted spherocylindrical surface as a reference surface. This eliminates any toricity, which the eye may have, and displays the elevation difference which cannot be accounted for a spherocylindrical model. The difference between the actual surface and the best-fit toric surface represents that part of the cornea that cannot be optically corrected with a spherocylindrical lens or spectacles.

After the system has subtracted out both the spherical and cylindrical components, the irregularity map displays the higher orders of the optical aberrations beyond sphere and cylinder or irregularity which is left as wavefront error (Fig. 3.14b). The deviation can be positive or negative that has equal effect on vision. Wavefront error describes the condition of the light rays as they pass through the corneal surface and are refracted onto the retina through the clear media and crystalline lens in the human eye. The greater the concentration of wavefront error, the more the light is not refracted properly onto the retina. This can result in aberrations, often described by patients as ”ghosting”, ”halos”, or ”glare”.

Green color marks the areas that most closely matche a smooth fitted toric surface. These areas are ”normal” or regular. Red indicates high wavefront error (i.e., greater irregularity). Conversely, as the wavefront error becomes more negative and therefore more blue, the irregularity can also become visually significant.

Difference Map

Difference map represents the change in corneal contour from one time point to another. It is calculated by subtracting the first map from the second one. This is useful for demonstrating the change occurring as result of a surgical procedure or during the subsequent healing phase.

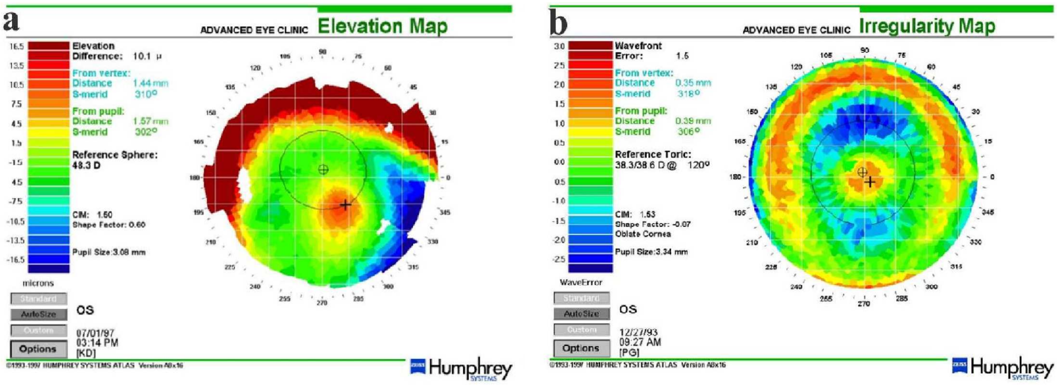

Elevation Difference: 10.1 μ
From vertex:
Distance 1.44 mm
S-merid 310°
From pupil:
Distance 1.57 mm
S-merid 302°
Reference Sphere:
48.3 D
CIM: 1.60
Shape Factor: 0.60
Pupil Size:3.08 mm
OS
07/01/97
03:14 PM
[KD]

Wavefront Error: 1.5
From vertex:
Distance 0.35 mm
S-merid 318°
From pupil:
Distance 0.39 mm
S-merid 306°
Reference Toric:
38.3/38.6 D @ 120°
CIM: 1.53
Shape Factor: -0.07
Oblate Cornea
Pupil Size:3.34 mm
OS
12/27/93
09:27 AM
[PG]

Fig. 3.14. **a** - Elevation map of a cornea. Warm colors depict points that are higher than the reference surface; cool colors designate lower points. Locations with no differences from reference sphere are marked with green. **b** - Irregularity map of a cornea.

3.3.2 Statistical Indices

Statistical indices are numbers which summarize a particular feature of the optical quality of the cornea to help predict visual performance. Those can be compared to a normal range or grouped to summarize the topography of several patients, as in clinical trials.

However, different commercial systems may give indices different names, but most of them are calculated in a similar way and perform the same function.

By understanding the statistical indices the clinicians become better adept at interpreting the results and uncovering corneal irregularities and abnormalities.

Some important statistical indices are described below.

Simulated Keratometry Value

The simulated keratometry value (SimK) provides information equivalent to that measured by the keratometer and is therefore primarily for historical reference.

Normally, both spherocylindrical and nonspherocylindrical values are given. The spherocylindrical SimK value provides the power and the location of the steepest meridian and the meridian 90° away. The nonspherocylindrical SimK value provides the power and location of the actual flattest meridian regardless of the angle between the steepest and flattest meridian. The cylinder is given as difference between the major and minor axes. These readings have the same limitations as keratometry.

Often total astigmatism (Tot Astig) measured as the difference between the steep refractive power and the flat refractive power and regular astigmatism (Reg Astig) measured as the amount and axis of the astigmatism that can be neutralized with a spherocylindrical correction are also listed. The display between total astigmatism and regular astigmatism is a measure of irregular astigmatism.

Surface Asymmetry Index

Surface asymmetry index (SAI) is a weighted summation of differences in corneal power between corresponding points 180° apart on equally spaced meridians. It is calculated from over the entire corneal surface, although the central points are given more weighting.

SAI approaches zero for a perfectly radially symmetrical surface and increases as the contour becomes more asymmetric. Since the normal cornea usually has a high degree of central radial symmetry (SAI<0.5), the SAI can be an useful quantitative parameter for monitoring changes that occur in patient's cornea and an indicator of the progression of corneal diseases such as keratoconus or peripheral corneal gutters.

The SAI is often higher than normal in keratoconus, penetrating keratoplasty, de-centered myopic refractive surgical procedures, trauma, and contact lens warpage. An adequate spectacle correction is often not achieved when SAI is high.

Surface Asphericity Index or Shape Factor

The surface asphericity index (SAI) indicates how much the curvature changes upon movement from the center to the periphery.

As it will be mentioned in Section 3.4, most investigators use the conic equation (Eq. (3.10)) with the asphericity parameter Q to describe the corneal shape. A normal cornea is prolate (i.e., the cornea becomes flatter towards the periphery) and has the asphericity Q of -0.26. If the cornea is flatter in the mid-periphery, the asphericity parameter will be more negative. If it is steeper, as after radial keratotomy, the asphericity parameter will be less negative or even positive.

In some cases instead of asphericity Q the shape factor p is used (Section 3.4). The relation between the asphericity and the shape factor is described by simple equation p=1+Q. Shape factor is also a measurement of the asphericity of the cornea and a derivative of eccentricity, which is a well known calculation of corneal shape used by contact lens fitters.

The shape factor can be also used to determine the asphericity and shows if the cornea is more oval or elliptical in shape in vertical or horizontal meridian (Fig. 3.15). The less spherical and more elliptical the cornea is in the horizontal meridian, the more the cornea will remember a prolate shape - a positive shape factor. Highly positive shape factor may imply that a pathology (such as keratoconus) exists. The less spherical and more elliptical the cornea is in the vertical meridian, the more the cornea will remember an oblate shape - a negative shape factor. A negative shape factor would mimic a post-refractive surgery eye, with the center being flatter than the periphery. A perfect sphere would have a shape factor of zero.

The shape factor distribution ranges in the human population are divided in three groups as shown in Tab. 3.2 [56].

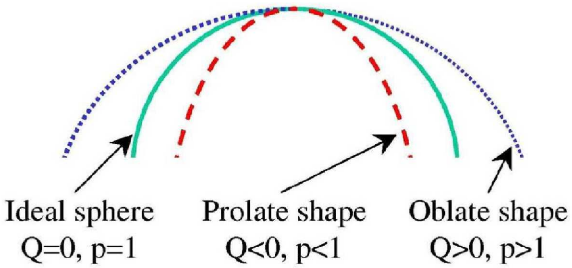

Fig. 3.15. How corneal shape relates to asphericity Q and shape factor p.

Surface (Ir)Regularity Index

Corneal (ir)regularity measurement is a number, or index, assigned to represent the smoothness of the corneal surface.

The surface regularity index (SRI) is a measure of the local fluctuations in corneal power. Within the central corneal surface of 4.5 mm in diameter, the power of each point is compared with that of the point immediately surrounding it. This index approaches zero for a normally smooth corneal surface and increases directly with increasing irregular astigmatism. Normal corneas have low SRI values (SRI<1.0), whereas those with poor visual potential due to irregular astigmatism have high values. When SRI is elevated, the corneal surface will be irregular, leading to a reduction in best spectacles-corrected visual acuity.

Some manufactures use the irregularity index instead of regularity index. The calculation uses thousands of data point of the corneal topography data to determine the difference in "height" or elevation between the patients cornea and a toric model of a cornea. The difference between the model and the actual cornea is measured in microns, and the standard deviation is taken. This is defined as corneal irregularity measurements.

Higher values of irregularity index, then, would tend to indicate a worsening pathology such as keratoconus, stemming from the inherent thinning and "wrinkling" of the corneal surface that the pathology causes. High index can also be observed in post-refractive surgery cornea due to the irregularity that the surgical procedure and subsequent healing process cause.

An ideal even surface has an irregularity index equal to zero. The higher the irregularity index, the more uncorrectable or uneven the surface is optically. This index calls attention to irregular astigmatism that often results in visual distortions.

Irregularity index distribution rages in the human population are shown in Tab. 3.2 [56]. The distribution appears in the human population with a mean irregularity index value of 0.63 microns, where 67% of the population falls between 0.03 and 0.64 microns. Inherent noise in the topography data itself accounts for the values between 0.00 and 0.03, which explains the reason for the normal range beginning at 0.03.

A similar measure is also the corneal uniformity index (CUI), which is a measure of the uniformity of the distortion of the corneal surface within the 3 mm pupil expressed

Tab. 3.2. Distribution ranges of the shape factor and irregularity index in the human population [56].

	Shape factor	Irregularity index
Borderline	0.20 to 0.12; 0.36 to 0.46	0.69 µm to 1.00 µm
Normal Cornea	0.13 to 0.35	0.03 µm to 0.68 µm
Abnormal Cornea	-1.00 to 0.10; 0.47 to 1.00	1.10 µm to 5.00 µm

as percentage. It varies from 0% if the cornea is completely irregular to 100% if the optical quality of the cornea is almost perfectly uniform[13]. Normal values usually exceed 80%.

In systems measuring corneal height, surface smoothness can be calculated from the Root-Mean-Square (RMS) deviation from the best-fit surface.

All these indices correlate well with potential visual acuity (PVA) [51] and can be used to predict the optical performance that might be expected in a particular patient based on the corneal topography, if other components of the visual system are functioning normally.

Potential Visual Acuity

The potential visual acuity (PVA) or predicted corneal acuity (PCA) is the estimated range of visual acuity which could be expected if the cornea was the only one factor limiting vision.

The predicted corneal acuity (PCA) is proposed to provide a single value in units of Snellen acuity of the optical quality of a corneal surface within 3 mm zone, ranging from 20/10 to 20/200. The PCA can be very helpful in differentiating corneal from lenticular disease. A regular corneal surface has a high PCA. Corneas with irregular astigmatism have lower potential acuities.

Keratoconus Prediction Index

The keratoconus prediction index (KPI) is a much more specific, but more complex index derived from the SimK and five other indices [30].

Some manufactures add extra maps, indices or functions to their software for more detailed presentation of the corneal topography [17]. They serve for the extensive description of the performance of the cornea as an optical system.

---

[13] This does not indicate that the cornea has good optical quality, simply that it is uniform; it could be uniformly bad or good.

3.4 Basic Corneal Models

The corneal shape can be described using of some mathematical models and several parameters.

The anterior corneal surface is asymmetrically aspheric. That is, the radius of curvature changes from the center to the limbus and does so at a different rate along different semi-meridians. Such a complex shape is difficult to measure mathematically, difficult to represent graphically, and difficult to understand and treat optically. Therefore the cornea is simplified by conceiving of the cornea as a spherocylindrical lens or as a section of an ellipse, a practical assumption as proven of wearers of spectacles and contact lenses. This simplification will some day be replaced by more accurate "shape factors", mathematical indices, or ray tracing diagrams.

An useful simplification to understand the overall topographic pattern of the cornea is to consider the corneal profile as a section of an ellipse (Fig.3.16). For ellipses (ellipsoids in one section only), the following equation is popular

$$\frac{(z-a)^2}{a^2} + \frac{y^2}{b^2} = 1\,, \tag{3.6}$$

where a and b are the major and the minor ellipse axis semi-lengths, and the z-axis is the optical axis. The vertex radius of curvature R is related to a and b by the equation

$$R = \frac{b^2}{a}\,. \tag{3.7}$$

The shape of an ellipse (i.e., the degree of elongation) is described by the eccentricity parameter e defined by the equation

$$e = \frac{c}{a} = \frac{\sqrt{a^2-b^2}}{a} = \sqrt{1-\left(\frac{b}{a}\right)^2}\,, \tag{3.8}$$

where c is the distance from the origin O to a focus F. The eccentricity of an ellipse has a value, $0 < e < 1$, where a value of e=0 represents a sphere, and a value of e=1 is associated with another conic section, the parabola[14]. The ellipsoidal surface has been described as an appropriate first-order model for the human cornea.

Another general mathematical expression for conic section, including ellipse, is Barers formula (Eq.(3.10)), that has been popular among vision scientists for modelling the corneal profile. This formula places the origin at the corneal apex and can describe a wide range of normal corneal shapes by varying just two parameters, the apical radius R and conic constant k.

If the cornea is to be represented by an aspheric mathematical model, the simplest model is to assume that the cornea is rotationally symmetric and can be represented by

---

[14] Specifying asphericity using e is not completely satisfactory because e^2 may be negative, in which case e cannot have a value.

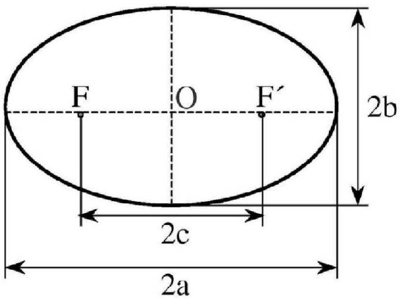

Fig. 3.16. Basic geometry of an ellipse: O is the origin, F and F' are the focal points, a and b are the major and minor axis length, respectively.

a conicoid in three dimensions or by a conic in two dimensions. A standard symmetric conic surface (i.e., optical conicoid) can be expressed in the form[15]

$$h^2 + (1+k)z^2 - 2zR = 0\,, \tag{3.10}$$

where R is the apical radius of curvature (i.e., at the point (0,0,0)), the z-axis is the axis of resolution of the conicoid and also the optical axis of the cornea, and $h^2 = x^2 + y^2$, where x and y represent lateral distances from the optical axis. The quantity k is a conic constant whose value and sign specifies the type of conicoid (Tab. 3.3). The the conic constant k is related to a and b by the equation

$$k = \left(\frac{b}{a}\right)^2 - 1\,. \tag{3.11}$$

The conicoid described by Eq. 3.10 cannot account for corneal asymmetries. Some asymmetries of corneal shape can be described mathematically by a conicoid in which k and R are functions of azimuth[16].

A number of studies have assumed a conicoid form but expressed the asphericity in terms of "shape factor" (or "form factor") p, which is related to conic parameter k and eccentricity e by the simple equation

$$k = e^2 = p - 1 \quad or \quad p = 1 + k = 1 - e^2\,. \tag{3.13}$$

---

[15] Sometimes the conicoid pole lies not at the origin of the coordinate axes, so Eq. 3.10 is modified to

$$(x - x_0)^2 + (y - y_0)^2 + (1+k)(z - z_0)^2 - 2(z - z_0)R = 0\,, \tag{3.9}$$

where the variables x_0, y_0, z_0 are the coordinates of the conicoid vertex.

[16] A mathematical model of a non-rotational conicoid considers the variation of radius and asphericity with meridian or azimuth in the surface. Thus, Eq. 3.10 should be modified to allow the asphericity k and radius R to vary with azimuth θ

$$k(\theta) = k_1 + k_2\,\cos^2(\theta - \alpha) \qquad R(\theta) = R_1 + R_2\,\cos^2(\theta - \beta)\,, \tag{3.12}$$

where θ is the azimuth angle measured from the horizontal. The angles α and β specify one of the angles of the azimuth containing either a maximum or minimum value of k or R.

Tab. 3.3. The conic constant (asphericity) and shape factor of several surface types.

Conic constant k or Asphericity Q	Shape factor p	Shape type	Description	Example
less than -0.26		Prolate	Marked peripheral flattering	Keratoconus
-0.26		Prolate	Mild peripheral flattering	Normal human cornea
0	1	Spherical	Uniform curvature	Steel calibration ball
more than 0		Oblate	Peripheral steepening	Radial Keratotomy

In most normal corneas, the central zone is steeper than the paracentral and peripheral zones, a configuration referred to as having a positive shape factor (positive because the radius of curvature becomes larger from the center to the periphery) and a prolate shape (the shape of a section across the steep end of an ellipse) (Fig. 3.15). The opposite topographic pattern occurs rarely in normal eyes but commonly after radial keratotomy: the central zone is flatter than the paracentral and peripheral zones, a configuration referred to as have a negative shape factor and an oblate shape (the shape of a section across the flatter side of an ellipse).

In the corneal topography the conic parameter k is often called the asphericity parameter Q ($k \equiv Q$).

According to the study by Kiely the means and standard deviations of R and Q in studied eyes were $R = 7.72 \pm 0.27$ mm and $Q = -0.26 \pm 0.18$ [20]. He found also that the non-rotationally symmetric conicoid (Eq. (3.8)) gives a more accurate representation of corneal shape than the rotationally symmetric conicoid (Eq. (3.7)). Other investigators found that the eccentricity e ranges from 0.4 to 0.9 (the corresponding range for Q is therefore -0.16 to -0.81), but the values of Q was usually negative, indicating that the cornea flattens away from the vertex.

3.5 Clinical Application of Corneal Topography

Clinicians need to know the shape and refractive power of the cornea for several reasons. So the corneal topography may be indicated in many clinical situations.

At present, the most profitable and practical use of the corneal topography is the refractive surgery for the purpose of vision correction. Corneal topography before and after refractive surgery (LASIK, PRK) helps to evaluate patients[17]. Preoperatively, corneal maps give insight into potential obstacles, such as scarring or irregular astigmatism. Postoperatively, topography provides clues about the success or failure[18] of a particular procedure, and corneal mapping certainly records what happened and

---

[17] There are also software simulating a planned refractive surgery.

[18] The failure of a refractive procedure results in residual refractive error and irregular astigmatism.

documents changes in an individual cornea. It can also help follow the healing phase.

The corneal topography may have its application in the fitting of contact lenses. The optical and fit properties of the lenses are now set by trial-and-error. Having an understanding of a patients corneal shape provides the eye care practitioners with a better initial guess to fit contact lenses effectively. Most corneal topographers provide software that can design an appropriate contact lens based upon the topography. They recommend lens material, size, design, and even simulate a fluorescein pattern. One can manually alter diameter, base curve, and edge design and observe the impact on the simulated pattern. There are even bitoric fitting programs designed for highly astigmatic patients. This software can greatly simplify the gas permeable fitting process, reduce chair time, and increase patient satisfaction. The information that corneal topography provides, can greatly enhance the ability to manage complex contact lens fits and increase overall success rate. Also, a current area of research is providing fully customized rigid contact lenses with hundreds of parameters individually tailored to a patients needs. Shape construction would help to optimize the back surface of the lens for maximum comfort.

Corneal topography is also useful for annually evaluating the topographical impact of corneal changes in soft contact lens patients. It is also virtually mandatory in corneal reshaping (Corneal Refractive Therapy or orthokeratology) to monitor the corneal changes occurring as well as the lens positioning from overnight wear.

Topography can assist with diagnosis of eye conditions that can deleteriously affect a patients vision. Degenerative eye conditions such as keratoconus and pellucid marginal degeneration may exhibit corneal steepening before any biomicroscopic signs are evident. In keratoconus, the topographical maps provide information of the location, size, and curvature of the cones apex and so can help follow the progression of the disease. Although contact lenses offer the potential of visual correction, it is difficult to fit a contact lens to a keratoconic cornea. In addition, these patients need to be screened out as poor candidates for refractive surgery. In order to effectively follow the progression of the disease and to fit a keratoconic cornea with contact lenses, it is helpful to know the precise shape of the cornea.

Finally, corneal maps can also reveal peripheral irregularities produced by surgery, trauma, or disease[19].

---

[19] Standard keratometry will not detect such irregularities unless they are central, and they may not be obvious with a slit-lamp unless there is some opacification.

Chapter 4

WAVEFRONT ANALYSIS

This chapter presents the principle of a measurement of wavefront aberrations with a Hartmann-Shack wavefront sensor.

4.1 Hartmann-Shack Wavefront Sensor

The Hartmann-Shack wavefront sensor (HSS), sometimes also called Shack-Hartmann sensor, is a sensor for measuring wavefront aberrations [25].

The idea of a wavefront sensor based on a single lens is shown in Fig. 4.1. An ideal plane wavefront falling on a lens is focused at the focal point of the lens F. In contrast, the focal point of an aberrated wavefront is shifted in the focal plane to F'. The displacement d in x- and y-direction depends on the angle of incidence α and the focal length of the lens f as follow

$$d_x = f\,\tan\alpha_x \quad d_y = f\,\tan\alpha_y\,. \tag{4.1}$$

That way the mean slope of the wavefront can be directly calculated from the focal point displacement.

A Hartmann-Shack wavefront sensor consists of many micro lenses that build a two-dimensional lens array (Fig. 4.2). Due to this lens array a beam is divided into many individual beams. Every micro lens focuses the light in the focal plane to a spot. An ideal wavefront is imaged as a regular grid of spots in the focal plane of the micro lens array. A distorted wavefront causes lateral dislocations of the spots, so the imaging is given by an irregular grid of spots. The spot of each micro lens is located at a position whose dislocations δx and δy in x- and y-direction are linearly related to the local average slope of the wavefront taken across the respective micro lens aperture

$$\delta x = f\,\tan\alpha_x \qquad \delta y = f\,\tan\alpha_y\,. \tag{4.2}$$

Usually, a CCD camera is used to detect the spot pattern of the Hartmann-Shack wavefront sensor (Fig. 4.3). The image is digitized and then analyzed towards a reference using computer software. The shape of an aberrated wavefront can be reconstructed from the spot displacements based on appropriate curve fitting algorithm and then presented using mathematical functions.

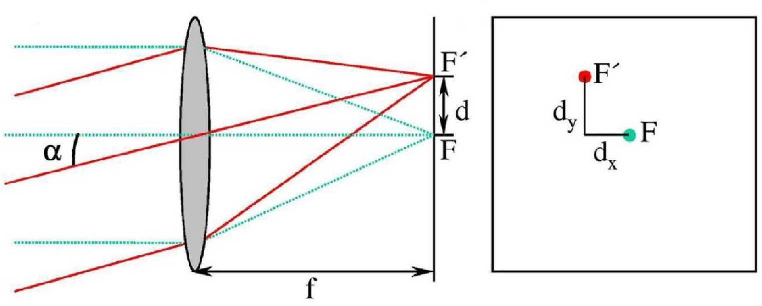

Fig. 4.1. The basic idea for measuring wavefront aberrations with a single lens. F is the focal point of the lens having the focal length f, d is the displacement of the focal point in the focal plane in the case of an aberrated wavefront, and α is the angle of incidence. The mean slope of an aberrated wavefront can be calculated from the focal point displacements d_x and d_y.

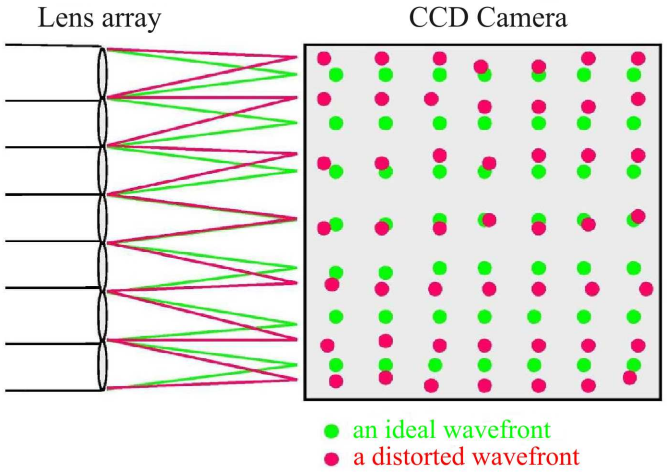

Fig. 4.2. A schematic diagram of the principle of a Hartmann-Shack wavefront sensor for measuring wavefront aberrations. An ideal plane wave is presented as a square grid of spots coded green. The spots of an aberrated wavefront are shown in red.

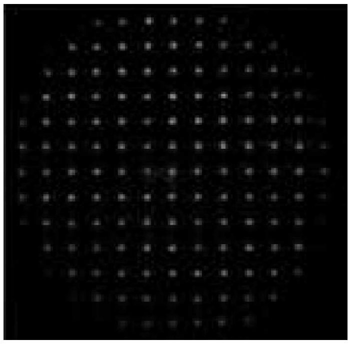

Fig. 4.3. A spot pattern as seen on a CCD camera.

Normally, the dynamic range of a Hartmann-Shack sensor is limited by the maximum slope angle that can be measured (Fig. 4.4). If the wavefront tilt is too large, the spots leave their original subapertures and may overlap or change places with the surrounding spots. Generally, this means that they cannot be separated or attached directly to their respective subapertures[1].

A micro lens of a lens array focuses a beam to a roughly round spot[2] whose diameter s equals to

$$s = 1.22\frac{\lambda f}{D_A}\,, \tag{4.3}$$

where λ is the wavelength, f is the focal length of the micro lens array, and D_A is the diameter of the micro lens.

According to Rayleigh criterion for a diffraction-limited system two neighboring spots can be separated from each other if the distance between them is more than the half of the spot diameter $s/2$. Thus, the maximal lateral shift of one spot is determined by

$$d_{max} = D_A - s\,. \tag{4.4}$$

The corresponding maximal local tilt α_{max} is

$$\alpha_{max} = \arctan\left(\frac{d_{max}}{f}\right) = \arctan\left(\frac{D_A - s}{f}\right). \tag{4.5}$$

The finest detectable shift d_{min} of a spot is limited by the pixel size S_{Pixel} of a CCD camera. The finest resolvable local tilt is

$$\alpha_{min} = \arctan\left(\frac{d_{min}}{f}\right) = \arctan\left(\frac{S_{Pixel}}{f}\right). \tag{4.6}$$

---

[1] In the meantime, some methods to overcome this problem have been developed [35].

[2] If the system is assumed to be diffraction-limited with a circular aperture, the spot size is equal to an airy disc size.

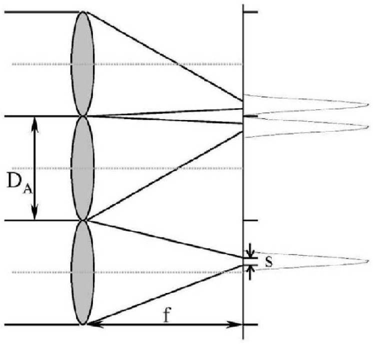

Fig. 4.4. The dynamical range of a Hartmann-Shack wavefront sensor is limited by the numerical aperture of the micro lens.

The values of α_{max} and α_{min} describe the resolution of a Hartman-Shack wavefront sensor[3]. Using a CCD camera with a finest pixel size or a lens array with a small focal length the resolution of the Hartmann-Shack wavefront sensor can be increased.

4.2 Wavefront Reconstruction

A Hartmann-Shack wavefront sensor measures a set of lateral dislocations δx_n and δy_n ($n = 1, 2, ..., N$, where N is the number of subapertures) of each spot relative to the optical axis of the corresponding micro lens, i.e., the reference points. These displacements can be interpreted as partial derivatives of the wavefront $W(x, y)$

$$\frac{\partial W(x_n, y_n)}{\partial x} = \tan\alpha_x = \frac{\delta x_n}{f} \qquad \frac{\partial W(x_n, y_n)}{\partial y} = \tan\alpha_y = \frac{\delta y_n}{f}\,, \tag{4.8}$$

where f is the focal length of the micro lens array.

The general problem is to find a way to reconstruct the wavefront using these discrete slope measurements, i.e., to determinate the phase of a wavefront from its gradient.

Many approaches have been proposed to accomplish wavefront reconstruction [43]. Basically, each approach may be categorized as being either zonal [15] or modal estimation [9] depending on whether the estimate is a phase value in a local zone or a coefficient of an aperture function. In either case, a least squares estimation algorithm can be used to construct the wavefront from the measurement of derivative information.

The modal estimation appears to be superior to zonal estimation, especially when only a fixed number of modes are of interest. The modal estimation has advantages

---

[3] If the tilt angle α is small enough ($\tan\alpha \approx \alpha$), than Eqs. (4.5), (4.6) can be simplified to

$$\alpha_{max} = \frac{D_A - s}{f} \qquad \alpha_{min} = \frac{S_{Pixel}}{f}\,. \tag{4.7}$$

on many aspects, for example the reconstruction is known to be less sensitive to noise, and the reconstructed wavefront is easy to be interpreted. Furthermore, the modal estimation is computationally easier and faster. Finally, both of these advances for the modal estimation, noise propagation, and computational difficulty are enhanced as the number of the measured data N increases.

In modal estimation, the estimated wavefront $W(x, y)$ is primarily assumed to be expanded in a set of basic functions in the form of

$$W(x, y) = \sum_{m} f_m F_m(x, y) , \tag{4.9}$$

where $F_m(x, y)$ are the basic functions, also called spatial modes, and f_m is the coefficient of the m-th mode. The base function may be Legendre polynomials, complex exponentials, Taylor polynomials (Section 4.3.2), or Zernike polynomials (Section 4.3.3). The wavefront is estimated by optimal fitting the coefficients of a functional basis to the measured local wavefront derivatives at several locations distributed over the sensor entrance pupil. An evaluation method using a least-squares fitting algorithm for wavefront reconstruction from the spot displacements is described in details in Section 5.5.2.

4.3 Wavefront Representation

The reconstructed wavefront $W^*(x, y)$ can be represented with several mathematical functions. In many cases, the wavefront is described by a few coefficients multiplying the terms of a well-chosen polynomials (Eq. (4.9)). Typically the Taylor or Zernike polynomials are used. One particular case to representation the primary aberrations is the expression given by the Seidel polynomials.

The Zernike polynomials are complete, orthonormal basis sets of functions defined on an unit circle and therefore natural candidates for describing an arbitrary wavefront over a circular pupil. Taylor polynomials are also complete, but they are typically defined in Cartesian coordinates. In practical terms, little difference exists between these two sets of polynomials, but the common used functions to describe the optical aberrations are the Zernike polynomials [54].

The wavefront is presented in rectangular coordinates, rather than polar coordinates, to accommodate the usual design of wavefront sensor that measure tilt in the subapertures in the x- and y-directions, rather than ρ- and θ-directions.

4.3.1 Seidel Polynomials

The Seidel aberrations were developed in the mid 19th century to account for the monochromatic geometrical aberrations of centered optical systems, i.e., defects from perfect imagery in optical systems that have an optical axis. The types of aberrations can be developed from considerations of symmetry, and are given names such as spherical aberration, coma, astigmatism, field curvature, and distortion. In addition

Tab. 4.1. The Seidel polynomials.

Index	Polynomial expression		Meaning
i	monomial	polar	
1	x	$\rho\cos\theta$	Tilt
3	x^2+y^2	ρ^2	Curvature of field (Defocus)
4	x^2+3y^2	$\rho^2\cos^2\theta$	Astigmatism
5	$y(x^2+y^2)$	$\rho^3\cos\theta$	Coma
6	$(x^2+y^2)^2$	ρ^4	Spherical aberration

Tab. 4.2. The Taylor polynomials up to fourth degree.

Index			Polynomial	Index			Polynomial	Index			Polynomial
k	n	m	expression	k	n	m	expression	k	n	m	expression
0	0	0	1								
1	1	0	x	6	3	0	x^3	10	4	0	x^4
2	1	1	y	7	3	1	x^2y	11	4	1	x^3y
3	2	0	x^2	8	3	2	xy^2	12	4	2	x^2y^2
4	2	1	xy	9	3	3	y^3	13	4	3	xy^3
5	2	2	y^2					14	4	4	y^4

to their type, aberrations are usually specified according to their order (third-order, fifth-order, etc.), although sometimes they are called primary, secondary, etc.

The magnitude of the aberrations is expressed in terms of an aberration polynomial (Tab. 4.1). The aberration polynomial coefficients can be found either from a series expansion of the law of refraction.

The Seidel polynomials (in polar coordinates) are commonly used in optical design to represent the wavefront phase of a rotationally symmetric optical system, but are not recommended as a basis for wavefront fitting in the case of a Hartmann-Shack wavefront sensor.

4.3.2 Taylor Polynomials

An alternative representation of a wavefront is in terms of monomials, i.e., powers of x and y given by Taylor polynomials

$$W_T(x,y)=\sum_{n=0}^{I}\sum_{m=0}^{n} t_{nm}T_{nm}(x,y)\,, \tag{4.10}$$

where t_{nm} are Taylor coefficients, $T_{nm}(x,y)=x^{n-m}y^m$ are Taylor polynomials (Tab. 4.2), and I is the degree of Taylor polynomial.

For an appropriate wavefront representation it is essential that the chosen set of polynomials allows to compare the classical aberrations easily. Therefore Taylor polynomials are not well suited for wavefront representation.

4.3.3 Zernike Polynomials

The Zernike polynomials were introduced by Zernike in the early 20th century and later developed by several workers to describe the diffraction theory of aberrations [54].

Like the Seidel aberration polynomials, Zernike polynomials describe defects from perfect imagery, but the nature of the Zernike expansion is different from the Seidel expansion. The Zernike polynomials describe the properties of an aberrated wavefront without regard to the symmetry properties of the system that gave rise to the wavefront.

An expansion of a wavefront $W(x, y)$ in Zernike polynomials to order I has the general form

$$W_Z(\rho,\theta) = \sum_{n=0}^{I} \sum_{m=-n}^{n} z_{nm} Z_n^m(\rho,\theta)\,, \tag{4.11}$$

where z_{nm} are the coefficients of the Zernike polynomials $Z_n^m(\rho,\theta)$.

The Zernike polynomials have some interesting and useful properties: they form a complete set, they are readily separated into radial and angular functions, and the individual polynomials are orthogonal over an entire unit circle[4]. The orthogonality of the Zernike terms is the best advantage because it is useful for introducing higher-order terms that are independent of the lower-order terms.

The Zernike polynomials are usually defined in polar coordinates $Z_n^m(\rho,\theta)$, where ρ is the radial coordinate ranging from 0 to 1, and θ is the azimuthal component ranging from 0 to 2π. Sometimes the Zernike polynomials are also expressed in monomials coordinates[5] $Z_n^m(x, y)$.

Each of the Zernike polynomial consists of three components: a normalization factor, a radial dependent components, and an azimuthal dependent component. The radial component is a polynomial, whereas the azimuthal component is sinusoidal.

There are two different numbering schemes for Zernike polynomials in common use: the single and double index scheme.

The double index scheme is useful for unambiguously describing the functions, with the index n describing the highest power or order of the radial polynomial and the index m describing the azimuthal frequency of the azimuthal component. In general, the Zernike polynomials are defined in this case as

$$Z_n^m(\rho,\theta) = \begin{cases} N_n^m R_n^{|m|}(\rho)\cos m\theta & for\ m \geq 0 \\ -N_n^m R_n^{|m|}(\rho)\sin m\theta & for\ m < 0 \end{cases}\,, \tag{4.11}$$

---

[4] Although the Zernike polynomials are orthogonal over an entire unit circle, they are not orthogonal over a portion of an unit circle, so that if the polynomials are generated by fitting to a limited set of data points, the orthogonality relationship may not be maintained.

[5] By the conversion of the Zernike polynomials defined in polar coordinates into Cartesian coordinates the following relations used here are: $x = \rho\cos\theta$ and $y = \rho\sin\theta$. But some authors use the reverse definition $x = \rho\sin\theta$, $y = \rho\cos\theta$.

where (ρ, θ) are polar coordinates in the unit circle. The radial function $R_n^{|m|}(\rho)$ are polynomials in ρ, containing the powers ρ^n, ρ^{n-2}, ..., ρ^m and are closely related to Jacobi's polynomials given by the following equations

$$R_n^{|m|}(\rho) = \sum_{s=0}^{(n-|m|)/2} (-1)^s \frac{(n-s)!}{s!(0.5(n+|m|)-s)!(0.5(n-|m|)-s)!} \rho^{n-2s} .$$

The normalization factor N_n^m is defined as

$$N_n^m = \sqrt{\frac{2(n+1)}{1+\delta_{m0}}} ,$$

where δ_{m0} is the Kronecker delta function[6].

The orthogonality and normalizing properties are expressed by the formulae

$$\int_0^{2\pi}\int_0^1 Z_n^{*|m|}(\rho,\theta)\, Z_{n'}^{|m'|}(\rho,\theta)\, \rho\, d\rho\, d\theta = \frac{\pi}{n+1}\delta_{mm'}\delta_{nn'} , \tag{4.12}$$

where δ_{ij} is the Kronecker symbol[6], and the asterisks denotes the complex conjugate; or in Cartesian coordinates

$$\int\int Z_{nl}^*(x,y)\, Z_{mk}(x,y)\, dx\, dy = \frac{\pi}{n+1}\delta_{mn}\delta_{kl} , \tag{4.13}$$

where the integration is over the unit circle $x^2+y^2 \leq 1$.

The single index scheme provides a unique ordering of two index parameters n and m in terms of one index parameter, i. The conversion between these indexing schemes can be different. One of many possibilities is given by the following equation [46]

$$i = \frac{n(n+2)+m}{2} \tag{4.14}$$

suggested in the report by Thibos et al. [46]. This report gives recommendations on definitions, conventions, and standard for reporting of optical aberrations of human eyes. To avoid confusion, when describing individual Zernike terms, the double index scheme should always be used. A standard single index scheme (Eq. (4.14)) should only be used for bar plots of expansion coefficients.

The Zernike polynomials identified by the single and double index schemes are shown in Tab. 4.3. There are also given the monomial form of the Zernike polynomials and their meaning.

---

[6] The Kronecker symbol (Kronecker delta function) is defined as

$$\delta_{ij} = \begin{cases} 1, & if\ \ i=j \\ 0, & if\ \ i \neq j \end{cases} .$$

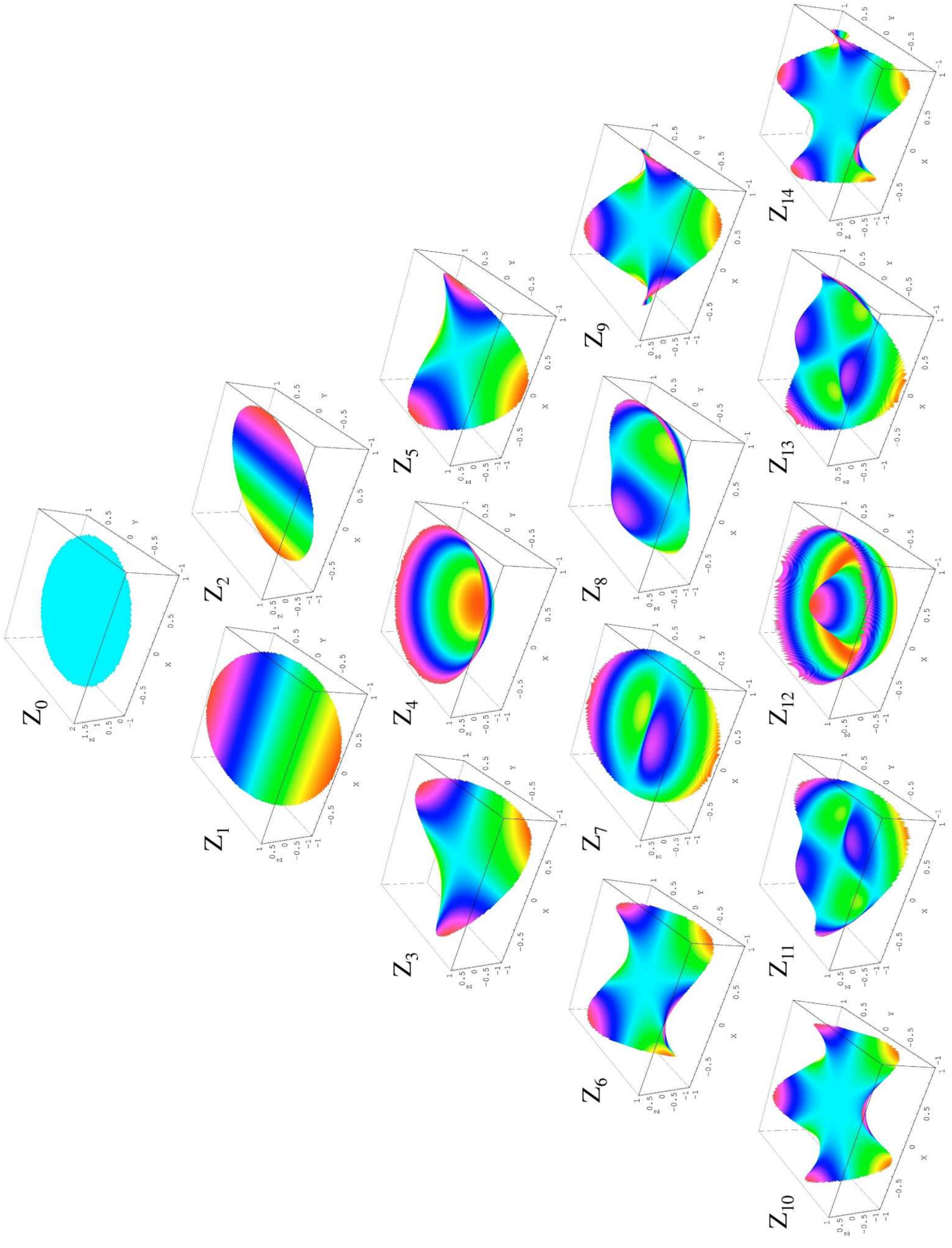

Fig. 4.5. Three-dimensional form of Zernike polynomials up to fourth order.

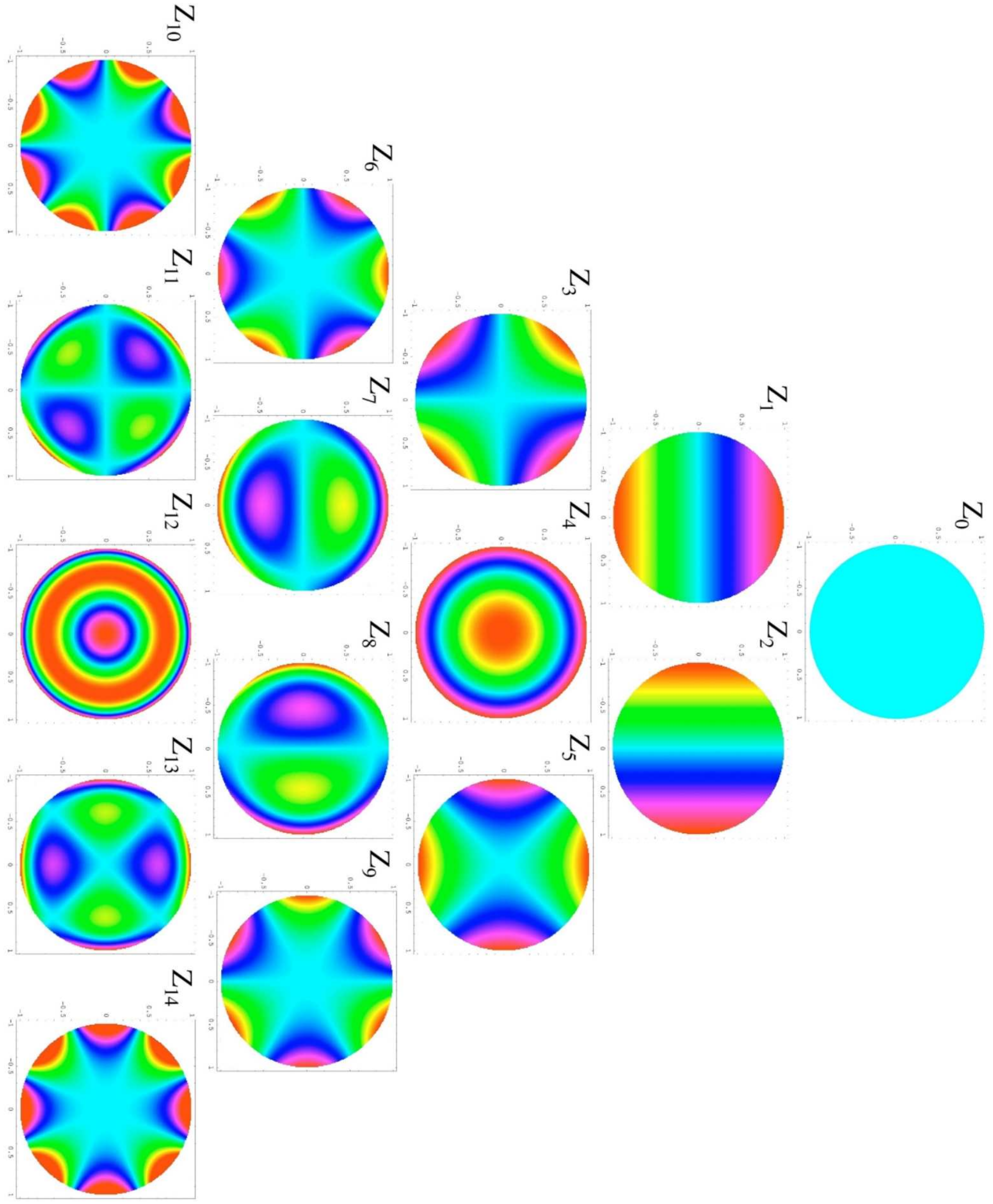

Fig. 4.6. Two-dimensional (x-y) projections of Zernike polynomials up to fourth order.

Tab. 4.3. The Zernike polynomials up to fourth order.

Single index* i	Order n	Frequency m	Normalization factor	Polar coordinates	Monomial coordinates	Meaning
0	0	0	1	1	1	Piston (constant term)
1	1	-1	2	$\rho \sin\theta$	y	Tilt about y axis
2	1	1	2	$\rho \cos\theta$	x	Tilt about x axis
3	2	-2	$\sqrt{6}$	$\rho^2 \sin 2\theta$	2xy	Astigmatism with axis at 45°
4	2	0	$\sqrt{3}$	$2\rho^2 - 1$	$2x^2 + 2y^2 - 1$	Defocus
5	2	2	$\sqrt{6}$	$\rho^2 \cos 2\theta$	$x^2 - y^2$	Astigmatism with axis at 0° or 90°
6	3	-3	$\sqrt{8}$	$\rho^3 \sin 3\theta$	$3x^2y - y^3$	Triangular astigmatism (Trefoil) with base on y axis
7	3	-1	$\sqrt{8}$	$(3\rho^3 - 2\rho) \sin\theta$	$3x^2y + 3y^3 - 2y$	Third-order coma along y axis
8	3	1	$\sqrt{8}$	$(3\rho^3 - 2\rho) \cos\theta$	$3x^3 + 3xy^2 - 2x$	Third-order coma along x axis
9	3	3	$\sqrt{8}$	$\rho^3 \cos 3\theta$	$x^3 - 3xy^2$	Triangular astigmatism (Trefoil) with base on x axis
10	4	-4	$\sqrt{10}$	$\rho^4 \sin 4\theta$	$4x^3y - 4xy^3$	Quadrangular astigmatism (Tetrafoil) with axis at 22.5°
11	4	-2	$\sqrt{10}$	$(4\rho^4 - 3\rho^2) \sin 2\theta$	$8x^3y + 8xy^3 - 6xy$	
12	4	0	$\sqrt{5}$	$6\rho^4 - 6\rho^2 + 1$	$6x^4 + 12x^2y^2 - 6x^2 + 6y^4 - 6y^2 + 1$	Third-order spherical aberration
13	4	2	$\sqrt{10}$	$(4\rho^4 - 3\rho^2) \cos 2\theta$	$4x^4 - 3x^2 - 4y^4 + 3y^2$	
14	4	4	$\sqrt{10}$	$\rho^4 \cos 4\theta$	$x^4 - 6x^2y^2 + y^4$	Quadrangular astigmatism (Tetrafoil) with axis at 0°

*The single index schema may be different by several authors.
In this work the single numbering schema recommended by Thibos was used (Eq. 4.14) [46].

Chapter 5

HARTMANN-SHACK CORNEAL TOPOGRAPHER

In this chapter the topography unit and the software are presented. The evaluation algorithm is also described.

5.1 Optical Principle

The optical principle behind the method for measuring corneal shape with a Hartmann-Shack wavefront sensor is shown in Fig. 5.1.

An objective is used to focus a beam on an ideal reference ball whose center of the curvature lies exactly in the focus of the objective F. Because the ball is perfectly spherical the beam rays are reflected back at every point of the surface into the same direction they have come from[1]. If the shape of the ball has some variations from the perfect sphericity, the rays are reflected into other directions at every point of the surface where there are differences. That way the information regarding the differences in the elevation of the surface is "saved" in the wavefront. The wavefront can be analyzed using a Hartmann-Shack wavefront sensor by the comparison of the spot positions of the reference wavefront (reflected from an ideal sphere) and of the one reflected from the actual surface (Chapter 4). The shape of the surface can be reconstructed using some mathematical algorithms. It should be noted that by the reflection the light runs a distance equal to the double value of the real elevation. Thus, this must be taken into account for the shape reconstruction.

5.2 Experimental Optical Setup

Fig. 5.2 shows the schematic diagram of the experimental system (HSS Corneal Topographer) used for the measurements.

The system consists of four main components: a laser as a light source, a Hartmann-Shack wavefront sensor as an image detector, a Z-tracker to control the position of the

---

[1] Assumed, the beam is an ideal wavefront and has not been aberrated by the objective. The beam rays fall then on the ball surface exactly perpendicular and according to the laws of optics are reflected back into themselves.

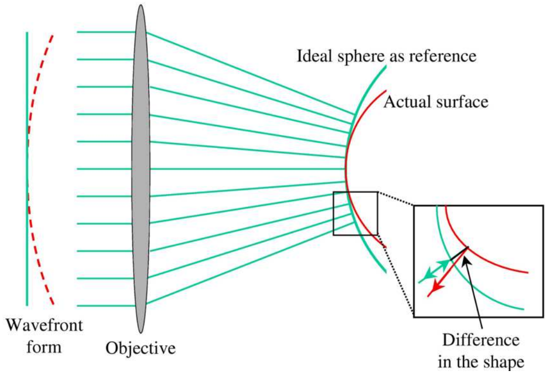

Fig. 5.1. Optical principle behind the corneal elevation measurement using a Hartmann-Shack wavefront sensor. Note, the differences in the elevation between the reference and the actual surface that are "saved" in the phase of the wavefront as double value.

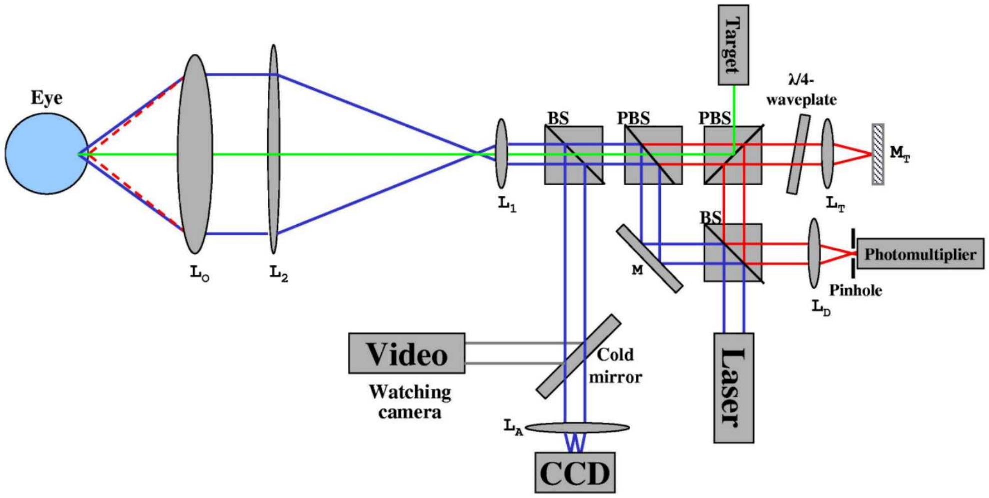

Fig. 5.2. Optical setup of the Hartmann-Shack Corneal Topographer.

cornea, and a computer system with an image acquisition unit. Additionally, there are some other optical components for beam transformations.

The used laser is an UV-laser with an output of 20 µW at 780 nm. The laser beam is collimated and formed with an anamorphic lens into a round beam having a diameter of about 7 mm and s-linear polarization state. The Hartman-Shack wavefront sensor uses a micro lens array with 53 mm focal length and 400 µm diameter of each micro lens. The video image module consists of a CCD camera with 656x581 pixels on 6.4x8.3 mm^2 chip.

The computer system with a frame grabber card allows to digitize video signals into images of 756x656 pixels at 8 bit. The images are analyzed with a software to reconstruct the corneal shape.

The optical path is as follows (Fig. 5.2). The s-linearly polarized beam from the laser is divided in two beams by a non-polarizing 50/50 beamsplitter. One beam (shown in blue in Fig. 5.2) is used for the measurement of the corneal topography, the other one (shown in red) for the positioning of the eye (or a sample) by a Z-tracker.

The first beam (which is colored blue) is reflected one time by the mirror M and then by the 90/10 polarizing beamsplitter. The second beam (which is colored red) is reflected by the 90/10 polarizing beamsplitter, goes trough the $\lambda/4$-waveplate that changes the beam polarization from s-polarization to circular polarization. This beam is focused by the lens L_T on the mirror M_T. After the beam has been reflected by the mirror M_T, the $\lambda/4$-waveplate transforms the beam polarization to p-polarization, and so the beam passes trough two 90/10 polarizing beamsplitters. Both beams widened by two lenses, L_1 and L_2, building a telescope. The objective L_O focuses the beams on a patient's eye.

The light reflected from the anterior surface of the cornea goes trough the objective and telescope back. A portion of the light from the first beam is reflected by the beamsplitter and falls on the lens array L_A. So the spot pattern can be seen on the charge-coupled device (CCD) camera. The light from the second beam passed through the beamsplitters is reflected by the mirror M_T. After it has passed the $\lambda/4$-waveplate it is s-linearly polarized again. Now the second beam is reflected by the 90/10 polarized beamsplitter and falls on the lens L_D that focuses the light on the detector indicating the maximum intensity if the cornea is at the correct axial position.

To have a correct measurement, the position of the anterior corneal surface must be accurate. For this purpose the video camera is used to center the patient's eye in the lateral position (x- and y-directions). The tracking of the anterior corneal position with the Z-tracker is used to determine the eye's position in axial direction (z-direction). The patient has also to fix on a visible target.

To start a measurement, the anterior surface of the cornea is feeded forward to a new axial position by the distance that is equal to the reference radius. The reference radius of the anterior corneal curvature R_{ref} is set to 7.8 mm.

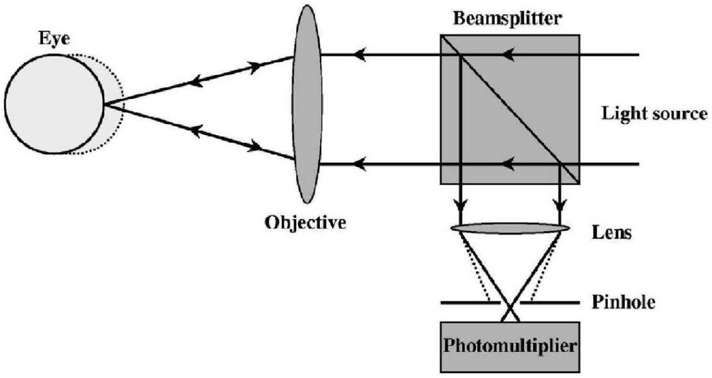

Fig. 5.3. A simplified schematic diagram of a confocal Z-tracker used in the HSS Corneal Topographer.

5.3 Z-Tracker

The Z-tracker is used for the positioning of the cornea at the correct axial position. The Z-tracker works by reflecting a beam off the anterior surface of the cornea. An adequate reflection occurs only when the corneal surface is sufficiently perpendicular to the beam. Because the cornea is spherical, the surface will no longer be perpendicular to the beam if the eye moves in x- or y-direction relative to the system. Therefore the requirement that the Z-tracker works imposes a limit on eye motion in lateral directions.

5.3.1 Ray Path

Fig. 5.3 shows a simplified optical path of the Z-tracker used in the Hartmann-Shack Corneal Topographer. The tracking of the corneal position is based on the confocal principle[2]. The basic idea behind confocal Z-tracking is to illuminate the apex of the cornea, and at the same time have a small detector aperture detect the reflected illumination.

The illumination light source is a laser whose beam is focused by an objective to a spot on the anterior corneal surface. Reflected light is travelling back through the objective. A lens focuses the light onto a pinhole positioned in the focal plane of the

---

[2] "Confocal" is defined as "having the same focus". What this means in the Z-tracker is that the final image has the same focus as or the focus corresponds to the point of focus in the object. The object and its image are "confocal". The Z-tracker is able to filter out the out-of-focus light from above and below the point of focus in the object. The confocal Z-tracker eliminates the out-of-focus information by means of a confocal pinhole situated in front of the image detection plane which acts as a spatial filter and allows only the in-focus portion of the light to be detected. Light from above and below the plane of focus of the object is eliminated from the final image. So the illuminated area and pinhole are in conjugate planes.

lens. As a detection device a highly sensitive photomultiplier is employed. The light is converted to an electrical signal by the detector. An analog digital card is used to convert the electrical signal from the photomultiplier into a digital signal that can be shown on a computer.

If the apex of the cornea is directly at the focus of the objective - "in-focus position" of the cornea, the reflected beam after passing through the objective is goes the same way through the optical system back. The lens focusses this parallel beam on the pinhole, so the beam passes completely through the pinhole, and thus, the light intensity registered on the photomultiplier is maximal. If the anterior corneal surface is at "out-of-focus position" (indicated in Fig. 5.3 with a dotted line), a larger area of the corneal surface is illuminated, and the beam is defocused. The reflected light is taking a different path through the optical system and is not focussed onto the detector aperture. Thus, it gives a much weaker light intensity on the detector that acts for right positioning of the anterior surface of the cornea as a Z-tracker. That way the detection of the axial corneal position is achieved[3].

5.4 Requirements on the Optics

The diameter of the area measured on the cornea depends on the numerical aperture of the objective L_O (Fig. 5.4a). From simple geometry it is defined as follow

$$AB = 2r_c \sin\left(\arctan\left(\frac{D}{2f_O}\right)\right), \tag{5.1}$$

where AB is the diameter of the area measured on the cornea, r_c is the corneal radius of curvature, D is the diameter of the illuminating beam, and f_O is the focal length of the objective.

It can be seen from Eq. (5.1) that the diameter of the area measured on the cornea would be larger if the focal length of the objective would be smaller by the beam diameter held constant[4]. Fig. 5.4b shows the relationship between the focal length of the objective f_O and the diameter of the field measured on the cornea AB calculated for a beam diameter D being 46.7 mm and a corneal radius of curvature r_c of 7.8 mm.

Due to optical components used in the Hartmann-Shack Corneal Topographer the beam diameter D is about 46.7 mm. This means the minimal aperture of the objective should be around 50 mm. In order to achieve a minimal area of 6 mm in diameter covering the apical zone of the cornea, an objective having a focal length of about 55 mm or less is required. Such an objective having a f-number[5] of 1.0 is difficult to design, and therefore it is very expensive.

---

[3] The effectuality of the tracking depends on the optics being used.

[4] But it should be not forgotten that there is a limit because it is impossible to manufacture an objective having a very short focal length and a large aperture at the same time.

[5] The f-number of an objective is the ratio of its focal length and the diameter of the aperture.

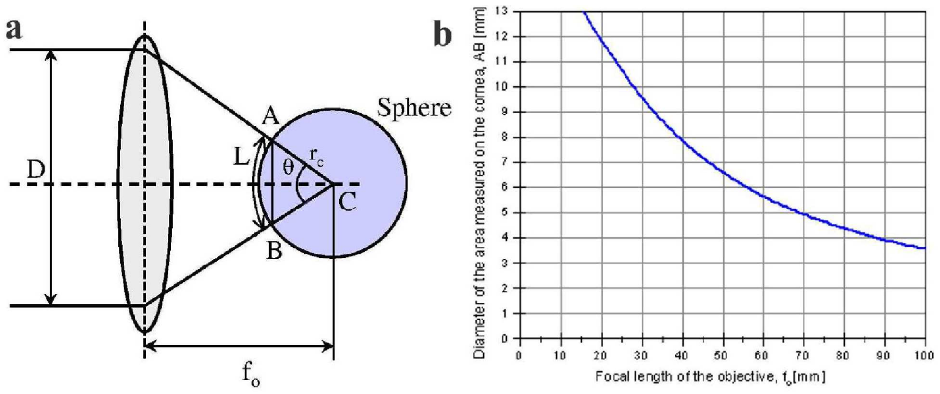

Fig. 5.4. **a** - The geometry of the calculation of the field measured on the cornea. **b** - The relationship between the focal length of the objective f_O and the field measured on the cornea AB demonstrates the high requirement on the optical quality of the objective used in the Hartmann-Shack Corneal Topographer. For the calculation (Eq. (5.1)) the beam diameter D has been set to 46.7 mm and the corneal radius of curvature r_c to 7.8 mm.

In the actual setup a Leica Noctilux M 50 mm/1.0 objective was used[6]. This objective is designed with seven elements and with "air lenses" for additional correction and has the focal length of f_O=50 mm and the f-number of 1.0. According to Eq. (5.1), the theoretical possible diameter of the area that can be measured on the cornea is about 6.6 mm. Actually, the measured area is around 6 mm.

5.5 Evaluation Algorithms

The topography of the cornea is determined by the analysis of the spot pattern seen on the CCD camera of the Hartmann-Shack wavefront sensor. These images provide the information about the wavefront reflected from the anterior corneal surface. The elevation of the cornea is "saved" in the wavefront shape that is measured with the Hartmann-Shack wavefront sensor (Section 5.1).

From the measurement a discrete field of partial derivatives δx_n and δy_n ($n = 1, 2, ..., N$, where N is the number of subapertures) is obtained. An approximation of the wavefront $W^*(x, y)$ can be calculated from these measurements by zonal or modal methods and expanded in a power series (Section 4.2). Thus, the estimation is to determine optimal expansion coefficients to best fit the measured directional derivatives.

---

[6] In the previous work an Olympus photo objective 55 mm/1.2 was used [22]. The area measured on samples simulating the human cornea was 4.9 mm in diameter. This is less than the theoretical possible value because of the strong optical aberrations of this objective for the IR light. The area measured on human corneas was smaller being 4.2 mm in diameter.

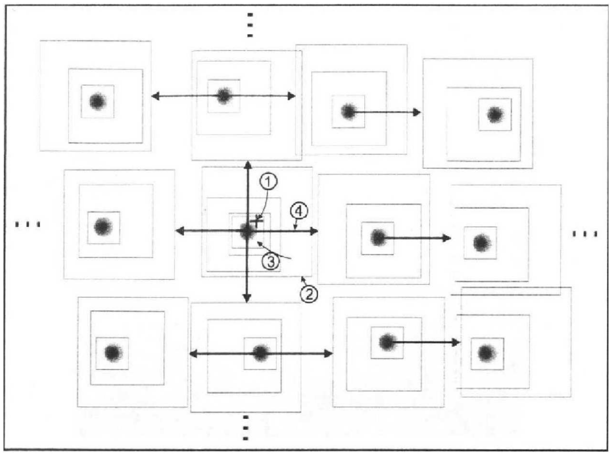

Fig. 5.5. Scheme of the spot finding algorithm [32].

5.5.1 Method for Spots Finding

Before the wavefront can be reconstructed the positions of the actual spots must be found[7].

As centroid of the spot (X_C,Y_C) the gravity point having the maximum of the gray value is mean. It is defined as the center of mass and can be determined by

$$X_C = \frac{\sum\limits_i \sum\limits_j x_{ij} g_{ij}}{\sum\limits_i \sum\limits_j g_{ij}} \qquad Y_C = \frac{\sum\limits_i \sum\limits_j y_{ij} g_{ij}}{\sum\limits_i \sum\limits_j g_{ij}},$$

where (x_{ij}, y_{ij}) is the position of pixel (i, j) and g_{ij} is its gray value [44].

Fig. 5.5 illustrates the spot finding algorithm. First, a start point near the expected centroid of a spot is given (1). The creation of the gravity point is taking place on the area of micro lens size (2). After the first rough centroid of the spot has been found, the mask is made smaller (3), and a new gravity point creation is performed on this smaller area around the first found centroid of the spot. If the new gravity point has been found, the mask around this point is made smaller again, and the precess is repeated. The iterations are continued iterative on always smaller areas until the area size achieves the expected size that has been set before or the specified iteration number has been achieved. The search for the next spot begins at the micro lens distance (4).

---

[7] The method for spot finding is described in details in the diploma thesis presented by F.Mueller [32].

5.5.2 Least Squares Method for Wavefront Reconstruction

In this work the wavefront reconstruction is realized using the least squares method[8]. This section describes the technique of best fitting a set of polynomial functions to a set of experimental determined data.

The measured dislocations of each spot in x- and y-direction δx_n, δy_n ($n = 1, 2, ..., N$, where N is the number of subapertures) have been determined from Hartmann-Shack wavefront sensor measurement. Now, a problem is to obtain the wavefront $W^*(x_n, y_n)$ by "fitting" a mathematical function to the measured spot shifts δx_n, δy_n.

The field of the measured dislocations δx_n, δy_n can be transformed to a set of local wavefront derivatives P_n and Q_n for each micro lens at the particular location in a subaperture position. That is

$$P_n \equiv \frac{\delta x_n}{f} = \frac{\partial W^*(x_n, y_n)}{\partial x} + \nu_n \qquad Q_n \equiv \frac{\delta y_n}{f} = \frac{\partial W^*(x_n, y_n)}{\partial y} + \mu_n,$$

where f is the focal length of the micro lens array, (x_n, y_n) are the coordinates of the nth measurement, and $n = 1, .., N$ numbers the experimental point data, with N being the number of spots. The ν_n and μ_n represent the noise assumed here to be zero[9].

The estimated wavefront derivatives P_n and Q_n can be expanded in a set of known functions $L_i(x, y)$

$$\frac{\partial W^*(x_n, y_n)}{\partial x} = \sum_{i=1}^{I} k_i L_i(x, y) \qquad \frac{\partial W^*(x_n, y_n)}{\partial y} = \sum_{i=1}^{I} l_i L_i(x, y), \tag{5.2}$$

where k_i and l_i are the coefficients of the estimated wavefront derivatives to be obtained, and the definite number I means that truncated polynomials $L_i(x, y)$ are used.

The wavefront estimation is to find the optimal expansion coefficients k_i and l_i in Eq. (5.2), which make the wavefront function $W^*(x_n, y_n)$ best fit the measurements of P_n and Q_n. For this purpose a least square fit is used.

According to the least squares method, the estimation is the best if the sum of the squares of all differences between the measured values and the estimation is as small as possible. The least squares functional in this case is given by

$$S = \sum_{n=1}^{N} \left(\frac{\partial W^*(x_n, y_n)}{\partial x} - P_n \right)^2 + \sum_{n=1}^{N} \left(\frac{\partial W^*(x_n, y_n)}{\partial y} - Q_n \right)^2 .$$

---

[8] The least squares method is not only one method to reconstruct the wavefront from the Hartmann-Shack wavefront measurement. Another method is presented in [27].

[9] No real sensor measures the directional derivative at a point. In a real sensor the aperture is partitioned into subapertures, and the measurement is actually an average of the directional derivative (tilt) over the subaperture associated with the measurement. Since the wavefront phase is analytic over the subaperture, a noise-free measurement would represent the phase at some point in the subaperture (by the mean-value theorem). However, the measurement is ascribed to be the tilt at the center of the subaperture. Thus, an instrumental error will exist in the estimation of the wavefront, since the measurements are not the tilts at the sampling locations. To minimize the instrumental error, one maximizes the number of subapertures.

The criterion for choosing k_i and l_i is to minimize the squared error, i.e., to minimize

$$S_x = \sum_{n=1}^{N} \left(\frac{\partial W^*(x_n, y_n)}{\partial x} - P_n \right)^2 = \sum_{n=1}^{N} \left(\sum_{i=1}^{I} k_i L_i(x_n, y_n) - P_n \right)^2$$

$$S_y = \sum_{n=1}^{N} \left(\frac{\partial W^*(x_n, y_n)}{\partial y} - Q_n \right)^2 = \sum_{n=1}^{N} \left(\sum_{i=1}^{I} l_i L_i(x_n, y_n) - Q_n \right)^2 .$$

Now, S_x and S_y are to minimize with respect to k_i and l_i, respectively. This results in the following equations

$$\frac{\partial S_x}{\partial k_i} = 2 \sum_{n=1}^{N} \left(\sum_{i=1}^{I} k_i L_i(x_n, y_n) - P_n \right) L_j(x_n, y_n) = 0$$

$$\frac{\partial S_y}{\partial l_i} = 2 \sum_{n=1}^{N} \left(\sum_{i=1}^{I} l_i L_i(x_n, y_n) - Q_n \right) L_j(x_n, y_n) = 0 .$$

This can be transformed to

$$\sum_{n=1}^{N} P_n L_j(x_n, y_n) = \sum_{i=1}^{I} k_i \sum_{n=1}^{N} L_i(x_n, y_n) L_j(x_n, y_n)$$

$$\sum_{n=1}^{N} Q_n L_j(x_n, y_n) = \sum_{i=1}^{I} l_i \sum_{n=1}^{N} L_i(x_n, y_n) L_j(x_n, y_n)$$

to calculate the coefficients k_i and l_i

$$k_i = \frac{\sum\limits_{n=1}^{N} P_n L_i(x_n, y_n)}{\sum\limits_{n=1}^{N} L_i(x_n, y_n) L_j(x_n, y_n)} \qquad l_i = \frac{\sum\limits_{n=1}^{N} Q_n L_i(x_n, y_n)}{\sum\limits_{n=1}^{N} L_i(x_n, y_n) L_j(x_n, y_n)} . \tag{5.3}$$

In the present treatment, where the wavefront estimation over a circular aperture must be carried out, it is more appropriate to expand the reconstructed wavefront $W^*(x, y)$ in terms of a complete set of polynomials $L_i(x_n, y_n)$ that are orthonormal over the interior of the circle, i.e.,

$$\sum_{n=1}^{N} L_i(x_n, y_n) L_j(x_n, y_n) = \delta_{ij} \qquad \forall\, i, j, \tag{5.4}$$

where δ_{ij} is the Kronecker delta. Due to this fact the calculation of the coefficients k_i and l_i can be simplified. So Eq. (5.3) is as follows

$$k_i = \sum_{n=1}^{N} P_n L_i(x_n, y_n) \qquad l_i = \sum_{n=1}^{N} Q_n L_i(x_n, y_n) . \tag{5.5}$$

Many sets of the orthonormal polynomials can be constructed[10]. In this work the following set of the orthonormal polynomials was used[11]

$$\begin{aligned}
L_1(x,y) &= \frac{1}{c_1} \\
L_2(x,y) &= \frac{x}{c_2} \\
L_3(x,y) &= \frac{y}{c_3} \\
L_4(x,y) &= \frac{xy}{c_4} \\
L_5(x,y) &= \frac{x^2+c_5}{c_6} \\
L_6(x,y) &= \frac{x^2+c_7y^2+c_8}{c_9} \qquad (5.6) \\
L_7(x,y) &= \frac{x^2y+c_{10}y}{c_{11}} \\
L_8(x,y) &= \frac{x^3+c_{12}x}{c_{13}} \\
L_9(x,y) &= \frac{x^3+c_{14}xy^2+c_{15}x}{c_{16}} \\
L_{10}(x,y) &= \frac{y^3+c_{17}x^2y+c_{18}y}{c_{19}}
\end{aligned}$$

The polynomial expansion was restricted to the determination of ten polynomials I=10 (if the number of the polynomials would be higher, the more Zernike coefficients could be obtained) [32].

For the orthogonality procedure of these polynomials the following conditions are important:

1. The lenses of the micro lens array are positioned symmetrically with respect to the coordinate axis. Thus, the sums $\sum_n x_n$ and $\sum_n y_n$ as well as all other sums having an odd potency of x or y are zero.

---

[10] However, one such set are the Zernike polynomials.

[11] These polynomials can be used for a circle aperture as well for a square spot sample.

2. The alignment of the micro lenses is invariant for a rotation through the angle 90°. This implies the exchange by the summation and the equality of the sums having an even potency such as the sums like $\sum\limits_n x_n^2$ and $\sum\limits_n y_n^2$.

3. The coordinates x and y are independent from each other. This means summations like $\sum\limits_n x_n y_n$ can be separated into two sums $\sum\limits_n x_n \sum\limits_n y_n$.

4. From conditions 1 and 3 follows that all sums are zero, if x or y occurs with uneven power (as an example $\sum\limits_n x_n^2 y_n{=}0$).

The constants c_i can be found from the orthonormality condition (Eq. 5.4) of the polynomials $L_i(x,y)$ in consideration of the conditions 1-4 listed above. They are as follows

$$c_1 = \sqrt{\sum_{n=1}^{N} 1} = \sqrt{N}$$

$$c_2 = \sqrt{\sum_{n=1}^{N} x_n^2}$$

$$c_3 = \sqrt{\sum_{n=1}^{N} y_n^2}$$

$$c_4 = \sqrt{\sum_{n=1}^{N} x_n^2 y_n^2}$$

$$c_5 = -\frac{c_2^2}{c_1^2}$$

$$c_6 = \sqrt{\sum_{n=1}^{N} x_n^4 + c_2^2 c_5}$$

$$c_7 = -\frac{\sum\limits_{n=1}^{N} x_n^4 + c_2^2 c_5}{c_4^2 + c_3^2 c_5}$$

$$c_8 = -\frac{c_2^2 + c_3^2 c_7}{c_1^2}$$

$$c_9 = \sqrt{\sum_{n=1}^{N} x_n^4 + c_7^2 \sum_{n=1}^{N} y_n^4 + c_1^2 c_8^2 + 2c_2^2 c_8 + 2c_3^2 c_7 c_8 + 2c_4^2 c_7}$$

$$c_{10} = -\frac{c_4^2}{c_3^2} \tag{5.7}$$

$$c_{11} = \sqrt{\sum_{n=1}^{N} x_n^4 y_n^2 + c_4^2 c_{10}}$$

$$c_{12} = -\frac{\sum_{n=1}^{N} x_n^4}{c_2^2}$$

$$c_{13} = \sqrt{\sum_{n=1}^{N} x_n^6 + c_{12} \sum_{n=1}^{N} x_n^4}$$

$$c_{14} = -\frac{\sum_{n=1}^{N} x_n^6 + c_{12} \sum_{n=1}^{N} x_n^4}{\sum_{n=1}^{N} x_n^4 y_n^2 + c_4^2 c_{12}}$$

$$c_{15} = -\frac{\sum_{n=1}^{N} x_n^4 + c_4^2 c_{14}}{c_2^2}$$

$$c_{16} = \Big[\sum_{n=1}^{N} x_n^6 + c_{14}^2 \sum_{n=1}^{N} x_n^2 y_n^4 + 2c_{14} \sum_{n=1}^{N} x_n^4 y_n^2 + c_{15} \sum_{n=1}^{N} x_n^4 + c_4^2 c_{14} c_{15}\Big]^{1/2}$$

$$c_{17} = -\frac{\sum_{n=1}^{N} x_n^2 y_n^4 + c_{10} \sum_{n=1}^{N} y_n^4}{\sum_{n=1}^{N} x_n^4 y_n^2 + c_4^2 c_{10}}$$

$$c_{18} = -\frac{\sum_{n=1}^{N} y_n^4 + c_4^2 c_{17}}{c_3^2}$$

$$c_{19} = \Big[\sum_{n=1}^{N} y_n^6 + c_{17}^2 \sum_{n=1}^{N} x_n^4 y_n^2 + 2c_{17} \sum_{n=1}^{N} x_n^2 y_n^4 + c_{18} \sum_{n=1}^{N} y_n^4 + c_4^2 c_{17} c_{18}\Big]^{1/2}$$

Thus, the analytical expressions of the coefficients of the partial derivations k_i and l_i (Eq. (5.5)) are as follow

$$k_1 = \frac{\sum_{n=1}^{N} P_n}{c_1}$$

$$k_2 = \frac{\sum\limits_{n=1}^{N} P_n x_n}{c_2}$$

$$k_3 = \frac{\sum\limits_{n=1}^{N} P_n y_n}{c_3}$$

$$k_4 = \frac{\sum\limits_{n=1}^{N} P_n x_n y_n}{c_4}$$

$$k_5 = \frac{\sum\limits_{n=1}^{N} P_n x^2 + c_5 \sum\limits_{n=1}^{N} P_n}{c_6}$$

$$k_6 = \frac{\sum\limits_{n=1}^{N} P_n x_n^2 + c_7 \sum\limits_{n=1}^{N} P_n y_n^2 + c_8 \sum\limits_{n=1}^{N} P_n}{c_9}$$

$$k_7 = \frac{\sum\limits_{n=1}^{N} P_n x_n^2 y_n + c_{10} \sum\limits_{n=1}^{N} P_n y_n}{c_{11}}$$

$$k_8 = \frac{\sum\limits_{n=1}^{N} P_n x_n^3 + c_{12} \sum\limits_{n=1}^{N} P_n x_n}{c_{13}}$$

$$k_9 = \frac{\sum\limits_{n=1}^{N} P_n x_n^3 + c_{14} \sum\limits_{n=1}^{N} P_n x_n y_n^2 + c_{15} \sum\limits_{n=1}^{N} P_n x_n}{c_{16}}$$

$$k_{10} = \frac{\sum\limits_{n=1}^{N} P_n y_n^3 + c_{17} \sum\limits_{n=1}^{N} P_n x_n^2 y_n + c_{18} \sum\limits_{n=1}^{N} P_n y_n}{c_{19}} \tag{5.8}$$

$$l_1 = \frac{\sum\limits_{n=1}^{N} Q_n}{c_1}$$

$$l_2 = \frac{\sum\limits_{n=1}^{N} Q_n x_n}{c_2}$$

$$l_3 = \frac{\sum_{n=1}^{N} Q_n y_n}{c_3}$$

$$l_4 = \frac{\sum_{n=1}^{N} Q_n x_n y_n}{c_4}$$

$$l_5 = \frac{\sum_{n=1}^{N} Q_n x^2 + c_5 \sum_{n=1}^{N} Q_n}{c_6}$$

$$l_6 = \frac{\sum_{n=1}^{N} Q_n x_n^2 + c_7 \sum_{n=1}^{N} Q_n y_n^2 + c_8 \sum_{n=1}^{N} Q_n}{c_9}$$

$$l_7 = \frac{\sum_{n=1}^{N} Q_n x_n^2 y_n + c_{10} \sum_{n=1}^{N} Q_n y_n}{c_{11}}$$

$$l_8 = \frac{\sum_{n=1}^{N} Q_n x_n^3 + c_{12} \sum_{n=1}^{N} Q_n x_n}{c_{13}}$$

$$l_9 = \frac{\sum_{n=1}^{N} Q_n x_n^3 + c_{14} \sum_{n=1}^{N} Q_n x_n y_n^2 + c_{15} \sum_{n=1}^{N} Q_n x_n}{c_{16}}$$

$$l_{10} = \frac{\sum_{n=1}^{N} Q_n y_n^3 + c_{17} \sum_{n=1}^{N} Q_n x_n^2 y_n + c_{18} \sum_{n=1}^{N} Q_n y_n}{c_{19}}$$

5.5.3 Wavefront Presentation

After the coefficients of the partial derivations k_i and l_i have been found, the wavefront can be represented.

One simple way for the wavefront representation is the Taylor expansion of the wavefront[12]

$$W_T(x, y) = \sum_{m=0} t_m T_m(x, y)\,, \tag{5.9}$$

---

[12] In Section 4.3.2 it has been noted that the Taylor polynomials are not commonly used for the wavefront representation. The fact that they are used here is an easier way to simplify the procedure to obtain the information relating the wavefront from its derivative data in terms of the Taylor coefficients first and then convert them to the Zernike coefficients using a matrix form (Eq. (5.20)).

where t_m are the Taylor coefficients, and the functions $T_m(x,y)$ are Taylor polynomials (Section 4.3.2).

In this work the Taylor polynomials as defined in Section 4.3.2 are used (Tab. 4.2). The expansion of the wavefront into the Taylor polynomials is truncated by 14th polynomials; that allows to calculate 14 Zernike coefficients. So the wavefront is represented as follow

$$\begin{aligned} W_T(x,y) &= t_0 + t_1x + t_2y + t_3x^2 + t_4xy + t_5y^2 + t_6x^3 + t_7x^2y + t_8xy^2 + \\ &\quad + t_9y^3 + t_{10}x^4 + t_{11}x^3y + t_{12}x^2y^2 + t_{13}xy^3 + t_{14}y^4 \,. \end{aligned} \tag{5.10}$$

The coefficients of the partial derivations k_i and l_i as obtained by Eq. (5.8) can be converted into the Taylor coefficients t_m as described below using Eq. (5.2).

$$\frac{\partial W_T(x,y)}{\partial x} = \frac{\partial}{\partial x}\sum_{m=0}^{14} t_mT_m(x,y) = \sum_{i=1}^{10} k_iL_i(x,y) \tag{5.11}$$

$$\frac{\partial W_T(x,y)}{\partial y} = \frac{\partial}{\partial y}\sum_{m=0}^{14} t_mT_m(x,y) = \sum_{i=1}^{10} l_iL_i(x,y) \,. \tag{5.12}$$

Using the expansion of the wavefront into the Taylor polynomials (Eq. (5.10))

$$\begin{aligned} \frac{\partial W_T(x,y)}{\partial x} &= t_1 + 2t_3x + t_4y + 3t_6x^2 + 2t_7xy + t_8y^2 + \\ &\quad + 4t_{10}x^3 + 3t_{11}x^2y + 2t_{12}xy^2 + t_{13}y^3 \end{aligned} \tag{5.13}$$

$$\begin{aligned} \frac{\partial W_T(x,y)}{\partial y} &= t_2 + t_4x + 2t_5y + t_7x^2 + 2t_8xy + 3t_9y^2 \\ &\quad + t_{11}x^3 + 2t_{12}x^2y + 3t_{13}xy^2 + 4t_{14}y^3 \end{aligned} \tag{5.14}$$

and the orthonormal polynomials (Eqs. (5.6))

$$\begin{aligned} \sum_{i=1}^{10} k_iL_i(x,y) &= \frac{k_1}{c_1} + \frac{k_2}{c_2}x + \frac{k_3}{c_3}y + \frac{k_4}{c_4}xy + \frac{k_5}{c_6}x^2 + \frac{k_5c_5}{c_6} + \frac{k_6}{c_9}x^2 + \\ &\quad + \frac{k_6c_7}{c_9}y^2 + \frac{k_6c_8}{c_9} + \frac{k_7}{c_{11}}x^2y + \frac{k_7c_{10}}{c_{11}}y + \frac{k_8}{c_{13}}x^3 + \\ &\quad + \frac{k_8c_{12}}{c_{13}}x + \frac{k_9}{c_{16}}x^3 + \frac{k_9c_{14}}{c_{16}}xy^2 + \frac{k_9c_{15}}{c_{16}}x + \\ &\quad + \frac{k_{10}}{c_{19}}y^3 + \frac{k_{10}c_{17}}{c_{19}}x^2y + \frac{k_{10}c_{18}}{c_{19}}y \,. \end{aligned} \tag{5.15}$$

$$\begin{aligned} \sum_{i=1}^{10} l_iL_i(x,y) &= \frac{l_1}{c_1} + \frac{l_2}{c_2}x + \frac{l_3}{c_3}y + \frac{l_4}{c_4}xy + \frac{l_5}{c_6}x^2 + \frac{l_5c_5}{c_6} + \frac{l_6}{c_9}x^2 + \\ &\quad + \frac{l_6c_7}{c_9}y^2 + \frac{l_6c_8}{c_9} + \frac{l_7}{c_{11}}x^2y + \frac{l_7c_{10}}{c_{11}}y + \frac{l_8}{c_{13}}x^3 + \end{aligned}$$

$$
\begin{aligned}
&+\frac{l_8 c_{12}}{c_{13}}x+\frac{l_9}{c_{16}}x^3+\frac{l_9 c_{14}}{c_{16}}xy^2+\frac{l_9 c_{15}}{c_{16}}x+\\
&+\frac{l_{10}}{c_{19}}y^3+\frac{l_{10} c_{17}}{c_{19}}x^2y+\frac{l_{10} c_{18}}{c_{19}}y\,. \qquad (5.16)
\end{aligned}
$$

Now, the Taylor coefficients[13] can be calculated by simple coefficients comparison by the equal potency of x and y variables of Eq. (5.13) with Eq. (5.15) and of Eq. (5.14) with Eq. (5.15) as follows. Note, that some coefficient comparisons give the double equations, thus, they are summarized, and the half of the summation is taken to calculate the appropriate Taylor coefficients.

$$
\begin{aligned}
t_1 &= \frac{k_1}{c_1}+\frac{k_5 c_5}{c_6}+\frac{k_6 c_8}{c_9}\\
t_2 &= \frac{l_1}{c_1}+\frac{l_5 c_5}{c_6}+\frac{l_6 c_8}{c_9}\\
t_3 &= \frac{1}{2}\left(\frac{k_2}{c_2}+\frac{k_8 c_{12}}{c_{13}}+\frac{k_9 c_{15}}{c_{16}}\right)\\
t_4 &= \frac{1}{2}\left(\frac{k_3}{c_3}+\frac{k_7 c_{10}}{c_{11}}+\frac{k_{10} c_{18}}{c_{19}}\right)+\frac{1}{2}\left(\frac{l_2}{c_2}+\frac{l_8 c_{12}}{c_{13}}+\frac{l_9 c_{15}}{c_{16}}\right)\\
t_5 &= \frac{1}{2}\left(\frac{l_3}{c_3}+\frac{l_7 c_{10}}{c_{11}}+\frac{l_{10} c_{18}}{c_{19}}\right)\\
t_6 &= \frac{1}{3}\left(\frac{k_5}{c_6}+\frac{k_6}{c_9}\right)\\
t_7 &= \frac{1}{4}\frac{k_4}{c_4}+\frac{1}{2}\left(\frac{l_5}{c_6}+\frac{l_6}{c_9}\right)\\
t_8 &= \frac{1}{2}\frac{k_6 c_7}{c_9}+\frac{1}{4}\frac{l_4}{c_4} \qquad (5.17)\\
t_9 &= \frac{1}{3}\frac{l_6 c_7}{c_9}\\
t_{10} &= \frac{1}{4}\left(\frac{k_8}{c_{13}}+\frac{k_9}{c_{16}}\right)\\
t_{11} &= \frac{1}{6}\left(\frac{k_7}{c_{11}}+\frac{k_{10} c_{17}}{c_{19}}\right)+\frac{1}{2}\left(\frac{l_8}{c_{13}}+\frac{l_9}{c_{16}}\right)
\end{aligned}
$$

---

[13] The Taylor coefficient t_0 can not be calculated. Besides also uninteresting because it represents a constant only.

$$t_{12} = \frac{1}{4}\left(\frac{k_9 c_{14}}{c_{16}} + \frac{l_7}{c_{11}} + \frac{l_{10} c_{17}}{c_{19}}\right)$$

$$t_{13} = \frac{1}{2}\frac{k_{10}}{c_{19}} + \frac{1}{6}\frac{l_9 c_{14}}{c_{16}}$$

$$t_{14} = \frac{1}{4}\frac{l_{10}}{c_{19}}\,.$$

The best and commonly used wavefront representation is the expansion of the wavefront into the Zernike polynomials[14] $Z_m(x, y)$ (Section 4.3.3)

$$W_Z(x, y) = \sum_{m=0} z_m Z_m(x, y)\,. \tag{5.18}$$

Because the functions $W_T(x, y)$ (Eq. (5.9)) and $W_Z(x, y)$ (Eq. (5.18)) represent the same wavefront, the Zernike coefficients z_m can be computed from the Taylor coefficients t_m by simple coefficients comparison

$$W_T(x, y) \equiv W_Z(x, y) \quad \Rightarrow \quad \sum_{m=0}^{14} t_m T_m(x, y) \equiv \sum_{m=0}^{14} z_m Z_m(x, y)\,. \tag{5.19}$$

The last equation can be rewritten in a matrix form

$$\vec{\mathbf{T}} = \mathbf{M}\,\vec{\mathbf{Z}}\,, \tag{5.20}$$

where $\vec{\mathbf{T}}$ and $\vec{\mathbf{Z}}$ are the column vectors containing the coefficients of the Taylor and Zernike polynomials, respectively

$$\vec{\mathbf{T}} = \begin{pmatrix} t_0, & t_1, & t_2, & \ldots, & t_{14} \end{pmatrix}$$

$$\vec{\mathbf{Z}} = \begin{pmatrix} z_0, & z_1, & z_2, & \ldots, & z_{14} \end{pmatrix}.$$

The square matrix $\mathbf{M}$ can be calculated easily

$$\mathbf{M} = \begin{pmatrix}
1 & 0 & 0 & 0 & -1 & 0 & 0 & 0 & 0 & 0 & 0 & 0 & 1 & 0 & 0 \\
0 & 0 & 1 & 0 & 0 & 0 & 0 & 0 & -2 & 0 & 0 & 0 & 0 & 0 & 0 \\
0 & 1 & 0 & 0 & 0 & 0 & 0 & -2 & 0 & 0 & 0 & 0 & 0 & 0 & 0 \\
0 & 0 & 0 & 0 & 2 & 1 & 0 & 0 & 0 & 0 & 0 & 0 & -6 & -3 & 0 \\
0 & 0 & 0 & 2 & 0 & 0 & 0 & 0 & 0 & 0 & 0 & -6 & 0 & 0 & 0 \\
0 & 0 & 0 & 0 & 2 & -1 & 0 & 0 & 0 & 0 & 0 & 0 & -6 & 3 & 0 \\
0 & 0 & 0 & 0 & 0 & 0 & 0 & 0 & 3 & 1 & 0 & 0 & 0 & 0 & 0 \\
0 & 0 & 0 & 0 & 0 & 0 & 3 & 3 & 0 & 0 & 0 & 0 & 0 & 0 & 0 \\
0 & 0 & 0 & 0 & 0 & 0 & 0 & 0 & 3 & -3 & 0 & 0 & 0 & 0 & 0 \\
0 & 0 & 0 & 0 & 0 & 0 & -1 & 3 & 0 & 0 & 0 & 0 & 0 & 0 & 0 \\
0 & 0 & 0 & 0 & 0 & 0 & 0 & 0 & 0 & 0 & 0 & 0 & 6 & 4 & 1 \\
0 & 0 & 0 & 0 & 0 & 0 & 0 & 0 & 0 & 0 & 4 & 8 & 0 & 0 & 0 \\
0 & 0 & 0 & 0 & 0 & 0 & 0 & 0 & 0 & 0 & 0 & 0 & 12 & 0 & -6 \\
0 & 0 & 0 & 0 & 0 & 0 & 0 & 0 & 0 & 0 & -4 & 8 & 0 & 0 & 0 \\
0 & 0 & 0 & 0 & 0 & 0 & 0 & 0 & 0 & 0 & 0 & 0 & 6 & -4 & 1
\end{pmatrix}.$$

---

[14] In Section 4.3.3 it is shown how these circle polynomials of Zernike may be derived, and some of their properties are discussed. The Zernike coefficients are useful for describing the shape of a cornea, as well as an aberrated wavefront in the pupil of an optical system [50].

So the Zernike coefficients can be now calculated from Eq. (5.20) by a simply matrix conversation

$$\vec{\mathbf{Z}} = \mathbf{M}^{-1}\,\vec{\mathbf{T}}\,, \tag{5.21}$$

where the matrix M^{-1} is

$$\mathbf{M^{-1}} = \begin{pmatrix}
1 & 0 & 0 & \frac{1}{4} & 0 & \frac{1}{4} & 0 & 0 & 0 & 0 & \frac{1}{8} & 0 & \frac{1}{24} & 0 & \frac{1}{8} \\
0 & 0 & 1 & 0 & 0 & 0 & 0 & \frac{1}{6} & 0 & \frac{1}{2} & 0 & 0 & 0 & 0 & 0 \\
0 & 1 & 0 & 0 & 0 & 0 & \frac{1}{2} & 0 & \frac{1}{6} & 0 & 0 & 0 & 0 & 0 & 0 \\
0 & 0 & 0 & 0 & \frac{1}{2} & 0 & 0 & 0 & 0 & 0 & 0 & \frac{3}{16} & 0 & \frac{3}{16} & 0 \\
0 & 0 & 0 & \frac{1}{4} & 0 & \frac{1}{4} & 0 & 0 & 0 & 0 & \frac{3}{16} & 0 & \frac{1}{16} & 0 & \frac{3}{16} \\
0 & 0 & 0 & \frac{1}{2} & 0 & -\frac{1}{2} & 0 & 0 & 0 & 0 & \frac{3}{8} & 0 & 0 & 0 & -\frac{3}{8} \\
0 & 0 & 0 & 0 & 0 & 0 & 0 & \frac{1}{4} & 0 & -\frac{1}{4} & 0 & 0 & 0 & 0 & 0 \\
0 & 0 & 0 & 0 & 0 & 0 & 0 & \frac{1}{12} & 0 & \frac{1}{4} & 0 & 0 & 0 & 0 & 0 \\
0 & 0 & 0 & 0 & 0 & 0 & \frac{1}{4} & 0 & \frac{1}{12} & 0 & 0 & 0 & 0 & 0 & 0 \\
0 & 0 & 0 & 0 & 0 & 0 & \frac{1}{4} & 0 & -\frac{1}{4} & 0 & 0 & 0 & 0 & 0 & 0 \\
0 & 0 & 0 & 0 & 0 & 0 & 0 & 0 & 0 & 0 & 0 & \frac{1}{8} & 0 & -\frac{1}{8} & 0 \\
0 & 0 & 0 & 0 & 0 & 0 & 0 & 0 & 0 & 0 & 0 & \frac{1}{16} & 0 & \frac{1}{16} & 0 \\
0 & 0 & 0 & 0 & 0 & 0 & 0 & 0 & 0 & 0 & \frac{1}{16} & 0 & \frac{1}{48} & 0 & \frac{1}{16} \\
0 & 0 & 0 & 0 & 0 & 0 & 0 & 0 & 0 & 0 & \frac{1}{8} & 0 & 0 & 0 & -\frac{1}{8} \\
0 & 0 & 0 & 0 & 0 & 0 & 0 & 0 & 0 & 0 & \frac{1}{8} & 0 & -\frac{1}{8} & 0 & \frac{1}{8}
\end{pmatrix}$$

Finally, the Zernike coefficients[15] are derived from the following relations

$$\begin{aligned}
z_0 &= t_0 + \frac{1}{4}(t_3 + t_5) + \frac{1}{8}(t_{10} + t_{14}) + \frac{1}{24}t_{12} \\
z_1 &= t_2 + \frac{1}{6}t_7 + \frac{1}{2}t_9 \\
z_2 &= t_1 + \frac{1}{2}t_6 + \frac{1}{6}t_8 \\
z_3 &= \frac{1}{2}t_4 + \frac{3}{16}(t_{11} + t_{13}) \\
z_4 &= \frac{1}{4}(t_3 + t_5) + \frac{1}{16}(3t_{10} + t_{12} + 3t_{14}) \\
z_5 &= \frac{1}{2}(t_3 - t_5) + \frac{3}{8}(t_{10} - t_{14}) \\
z_6 &= \frac{1}{4}(t_7 - t_9) \\
z_7 &= \frac{1}{12}t_7 + \frac{1}{4}t_9 \qquad (5.22) \\
z_8 &= \frac{1}{4}t_6 + \frac{1}{12}t_8
\end{aligned}$$

---

[15] Here the single numbering schema is used (Section 4.3.3).

$$z_9 = \frac{1}{4}(t_6 - t_8)$$

$$z_{10} = \frac{1}{8}(t_{11} - t_{13})$$

$$z_{11} = \frac{1}{16}(t_{11} + t_{13})$$

$$z_{12} = \frac{1}{16}(t_{10} + t_{14}) + \frac{1}{48}t_{12}$$

$$z_{13} = \frac{1}{8}(t_{10} - t_{14})$$

$$z_{14} = \frac{1}{8}(t_{10} - t_{12} + t_{14})$$

Using these Zernike coefficients the estimated wavefront $W^*(x,y)$ and also the corneal shape can be displayed as a two-dimensional map as well as a wire net.

5.5.4 Evaluation Performance

The performance of the wavefront estimation can be expressed in terms of the root mean square errors (RMS) $<(\delta W)^2>$ in the estimated wavefront $W^*(x,y)$, where $<>$ indicates the statistical expectation value.

The quality of the wavefront estimation $<(\delta W)^2>$ can be obtained from the differences between the spot positions actually measured $(x_{n\,measured}, y_{n\,measured})$ and reconstructed $(x_{n\,reconstructed}, y_{n\,reconstructed})$ as follows

$$\begin{aligned} <(\delta W)^2> \;\; &= \;\; \Big(\frac{1}{2N}\sum_{n=1}^{N}[(x_{n\,measured} - x_{n\,reconstructed})^2 + \\ &\qquad + (y_{n\,measured} - y_{n\,reconstructed})^2]\Big)^{1/2} . \end{aligned} \tag{5.23}$$

Thereby, the coordinates of the reconstructed spots $(x_{n\,reconstructed},\, y_{n\,reconstructed})$ are calculated by the following equations

$$x_{n\,reconstructed} = x_{n\,Reference} + \delta x \cdot f$$

$$y_{n\,reconstructed} = y_{n\,Reference} + \delta y \cdot f \,,$$

where δx and δy are the displacements of the reconstructed spots from the reference that can be calculated from the Taylor coefficients t_i obtained by Eq. (5.17)[16]

$$\delta x = t_1 + 2t_3x + t_4y + 3t_6x^2 + 2t_7xy + t_8y^2 + 4t_{10}x^3 + 3t_{11}x^2y + 2t_{12}xy^2 + t_{13}y^3$$

$$\delta y = t_2 + t_4x + 2t_5y + t_7x^2 + 2t_8xy + 3t_9y^2 + t_{11}x^3 + 2t_{12}x^2y + 3t_{13}xy^2 + 4t_{14}y^3 \,,$$

where x and y are the coordinates of the reference spot positions $(x_{n\,Reference}, y_{n\,Reference})$.

---

[16] For the calculation of the displacements δx and δy the Zernike coefficients can be also used, but this way makes the calculation more difficult.

5.6 Calculation of Corneal Parameters

Some corneal parameters can be also calculated to describe the corneal shape and its optical quality.

5.6.1 Corneal Defocus and Astigmatism

The Zernike coefficients of the second order (45° astigmatism - z_3, focal shift - z_4, and 0°/90° astigmatism - z_5) describe optical defects that can be corrected by conventional spectacles, namely sphere and astigmatism. It is possible to convert this portion of the wavefront aberration to the equivalent ophthalmic spectacle prescription of corneal defocus and astigmatism.

The defocus[17] and astigmatism of the cornea can be obtained from the Zernike coefficients z_3, z_4, and z_5 by the following equations [10]

$$Defocus = \frac{4z_4}{R} \tag{5.24}$$

$$Astigmatism = 4\frac{\sqrt{z_3^2 + z_5^2}}{R} \tag{5.25}$$

$$Axis\ of\ astigmatism = \frac{180^\circ}{2\pi}\, atan\frac{z_3}{z_5}\,, \tag{5.26}$$

where R is the physical radius of the expansion on the cornea (in meters), and the Zernike coefficients are expressed in no units[18].

5.6.2 Statistical Indices

Additionally, statistical indices such as irregularity index and asymmetry index can be calculated (for definitions, see Section 3.3.2).

Because the measurement method of the HSS Corneal Topographer is different from that used by a videokeratoscope, the algorithms for calculation of the indices may be also differ.

Surface irregularity index (SII) is the standard deviation of the difference in elevation between the best fitted toric surface and an actual surface

$$SII = \sqrt{\frac{\sum\limits_{i=1}^{N}(h_i - \bar{h})}{N(N-1)}}\,, \tag{5.27}$$

---

[17] A myopic wavefront error has a positive sign, but by clinical conversation, myopic prescriptions are given a minus sign.

[18] The Zernike coefficients z_i can be also expressed in microns if they are normalized on the aperture radius or in wavelengths if they are normalized on the wavelength.

where N is the number of data, h_i is the elevation (in microns) at every point of the surface, and $\bar{h}$ is the mean value of the elevation defined as

$$\bar{h} = \frac{\sum_i^N h_i}{N} \, .$$

Asymmetry index (AI) of the surface is a summation of differences in corneal power between corresponding points 180° apart[19]

$$AI = \sum_i (P_i - P_i^{'}) \, , \tag{5.28}$$

where P_i is the refractive power at each position of the cornea, and $P_i^{'}$ is the refractive power 180° apart at the same radial distance. The refractive power P_i (in diopters) at each point of the cornea is calculated by Eq. (3.3)

$$P_i = \frac{n-1}{h_i + R_{Ref}} = \frac{3.76 \cdot 10^5}{h_i + 7800} \, , \tag{5.29}$$

where n is the refractive index of the cornea being 1.376, h_i is the elevation (in microns) at that point, and R_{Ref} is the reference radius of the cornea set to 7.8 mm.

5.6.3 Optical Quality of the Corneal Surface

From the topographic data, it is possible to calculate sophisticated measures of optical performance.

When studying corneal optics, it is important to remember that each point in an image is formed by all the light passing through the pupil. Description of corneal optical performance should therefore consider the corneal optical zone as a whole. If the goal is to depict optical performance of the cornea, other descriptors such as the point spread function (PSF), the optical transfer function (OTF) may be more appropriate than any of the topographic maps. Each of these functions can be computed from the topography, but they are generally not available on current clinical instruments.

The HSS Corneal Topographer provides some parameters describing the optical quality of the cornea that are obtained from a measurement.

Root-Mean-Square (RMS)

Root-mean-square (RMS) wavefront error provides a general estimate of the variation of the measured wavefront from an ideal one. The higher the RMS wavefront error, the larger the wavefront aberration is (i.e., the more the measured wavefront differs from an ideal wavefront) and the worse the image quality.

---

[19] The surface asymmetry index provided by a standard videokeratograph is defined as a weighted summation.

The RMS wavefront error is calculated as the mean squared value of the wavefront $W(\rho,\theta)$ over the pupil

$$RMS = \sqrt{\frac{\int\limits_0^r \int\limits_0^{2\pi} W^2(\rho,\theta)\rho\, d\rho\, d\theta}{\int\limits_0^r \int\limits_0^{2\pi} \rho\, d\rho\, d\theta}} = \sqrt{\frac{1}{\pi r^2} \int\limits_0^r \int\limits_0^{2\pi} W^2(\rho,\theta)\rho\, d\rho\, d\theta}\,, \tag{5.30}$$

where r is the pupil radius.

If the wavefront is described using Zernike polynomials $Z_n^m(\rho,\theta)$, the RMS wavefront error can be directly calculated from the Zernike coefficients z_{nm}

$$\begin{aligned} RMS &= \sqrt{\frac{1}{\pi r^2} \int\limits_0^r \int\limits_0^{2\pi} [\sum_{n=0}^{I} \sum_{m=-n}^{n} z_{nm} Z_n^m(\rho,\theta)]^2 \rho\, d\rho\, d\theta} = \\ &= \sqrt{\frac{1}{\pi r^2} \sum_{n=0}^{I} \sum_{m=-n}^{n} z_{nm}^2 \int\limits_0^r \int\limits_0^{2\pi} (Z_n^m(\rho,\theta))^2 \rho\, d\rho\, d\theta}\,. \end{aligned} \tag{5.31}$$

The RMS wavefront error can be calculated using Eq. (5.31) for different orders. So if only the second and third order of the Zernike polynomials are considered by the expansion of the wavefront into Zernike polynomials, then the RMS wavefront error is referred as the RMS of the third order[20]. If the expansion of the wavefront is truncated by the fourth order, one speaks about the RMS of the fourth order and so on.

Optical Aberration Index

Optical aberration index (OAI) is defined as

$$OAI = 1 - exp(-RMS)\,, \tag{5.32}$$

where RMS is the RMS wavefront error generally calculated using Eq. (5.30).

The optical aberration index varies between zero and one. An optical system is perfect if its optical aberration index is zero. The optical aberration index equal to one stands for infinity aberrations. This index is very sensitive in the typical range for higher order aberrations.

Strehl Ratio

To quantify the performance of an optical system, the Strehl ratio (SR) of the point spread function (PSF) is used. The point spread function is interpreted as the image plane intensity distribution that results from imaging a point source.

---

[20] The 0th order of Zernike coefficients can be set to zero. The first order Zernike coefficients can be omitted in the calculation because they describe the tilt only (i.e., the position of the eye) and do not give any information about the optical characteristics.

Strehl ratio is defined as the ratio of the peak focal intensities of an aberrated point spread function and a diffraction limited (i.e., ideal) point spread function

$$S = \frac{I(\bar{x}=0)_{aberrated}}{I(\bar{x}=0)_{diffraction-limited}}\,,$$

where $I(\bar{x})$ is the intensity point spread function, and $\bar{x}$ defines a point in the image plane.

The Strehl ratio is given by the zero frequency component of the Fourier transform

$$S = \frac{1}{\pi^2}\Big[\int_0^{2\pi}\int_0^1 e^{2\pi i\Delta W(\rho,\theta)}\rho\,d\rho\,d\theta\Big]^2,$$

where $\Delta W(\rho,\theta)$ is the wavefront aberration relative to the reference sphere for diffraction focus in waves. The integrand may be expanded in a Taylor series

$$S = \frac{1}{\pi^2}\Big[\int_0^{2\pi}\int_0^1 \Big(1 + 2\pi i\Delta W + \frac{1}{2}(2\pi i\Delta W)^2 + ...\Big)\rho\,d\rho\,d\theta\Big]^2.$$

If the aberrations are so small that the third-order and higher-order powers of $2\pi\Delta W$ can be neglected, then

$$\begin{aligned} S &\simeq \Big[1 + 2\pi i\overline{\Delta W} - \frac{1}{2}(2\pi)^2\overline{\Delta W^2}\Big]^2 \simeq 1 - (2\pi)^2(\overline{\Delta W^2} - (\overline{\Delta W})^2) \simeq \\ &\simeq 1 - (2\pi\sigma)^2\,, \end{aligned} \tag{5.33}$$

where $\sigma = \sqrt{\overline{\Delta W^2} - (\overline{\Delta W})^2}$ is the root-mean-square deviation of the wavefront measured in wavelengths.

A better approximation for most types of aberrations is

$$S \simeq e^{-(2\pi\sigma)^2}\,, \tag{5.34}$$

which is good for $S > 0.1$.

5.7 Software Tools

A special software was written to make measurements, analyze the spot pattern, calculate the Zernike coefficients, and reconstruct the corneal shape. This subsection describes the software algorithm. For description of the program user interface, see Appendix A. Tests of the software algorithm are described in Section 6.1.

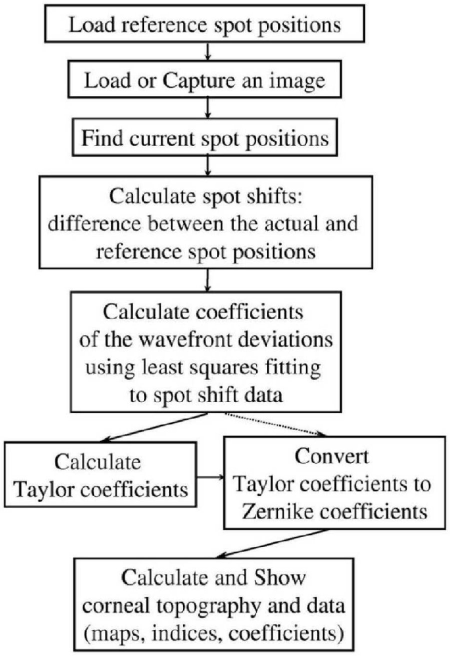

Fig. 5.6. Flow chart diagram of the software evaluation algorithm.

5.7.1 Software description

The flow chart diagram of the software is presented in Fig. 5.6.

First of all the reference spot positions are needed. The reference image can be taken using a calibrated, ideal spherical steel ball. This reference image contains all the optical aberrations of the system taken into account by every measurement.

After a spot pattern of a cornea is taken or an existing image is loaded the actual spot positions can be found (Section 5.5.1). This happens manually by clicking on the middle spot of the spot pattern.

The spot displacements are computed with respect to the spot positions from the reference. The coefficients of the wavefront deviations can be obtained using the least squares fitting to these displacement data as described in Section 5.5.2. Finally, these coefficients are converted to Taylor and then to Zernike coefficients (Section 5.5.3). The corneal topography maps and data are calculated using Zernike coefficients and displayed.

Chapter 6

TESTS AND MEASUREMENTS

The first purpose of measurements was to assess the accuracy[1] and reproducibility[2] of the HSS Corneal Topographer. The second goal was a comparison of two systems - the HSS Corneal Topographer and a standard videokeratograph.

One way to determine the measurement accuracy and precision of a system is to use calibrated test surfaces that more closely model the cornea. Ideally, the accuracy and precision should be also tested on human eyes. But measurements of the human cornea are more difficult because the absolute power of a human cornea is unknown. Therefore only the reproducibility (i.e., the precision and the repeatability) of the instrument on the human eye could be determined.

This chapter presents tests of software and experimental results on tested objects and human eyes. Additionally, the test measurements of the Z-tracker module and the influence of the axial shift on the Zernike coefficients are presented.

The measurement execution is explored in Section A.2.

6.1 Tests of Software Algorithm

The software was tested to warrant that the calculation algorithm works correctly. For this purpose pictures (as they would be seen on a CCD camera of a Hartmann-Shack wavefront sensor) with known optical aberrations were generated and evaluated (Fig. 6.1). So it was possible to test the evaluation algorithm for several Zernike coefficients z_i or for a group of the Zernike coefficients.

The tests showed a perfect reliability of the evaluation and calculation algorithm. The results of the tests are shown in Fig. 6.2.

First, only one of the Zernike coefficients was entered. The value of each Zernike coefficient (for example only z_1, then only z_2, and so on) was set to 0.5 µm. As seen in Fig. 6.2a, if one selected aberration has been set to this value, the output value of the corresponding Zernike coefficient[3] z_i (i=1, 2, ..., 14) was 0.5 µm while all other Zernike coefficients were zero. This situation was observed for all possible aberrations.

---

[1] The accuracy describes the proximity of a value being measured to a real value.

[2] The reproducibility describes the precision and the repeatability.

[3] The Zernike coefficient z_0 was not taken into account.

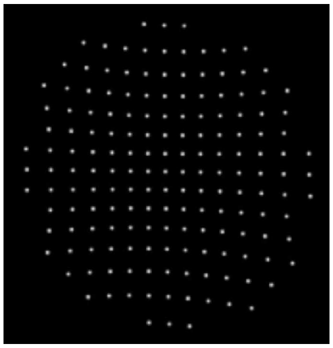

Fig. 6.1. An example of a picture used for the test of the software algorithm.

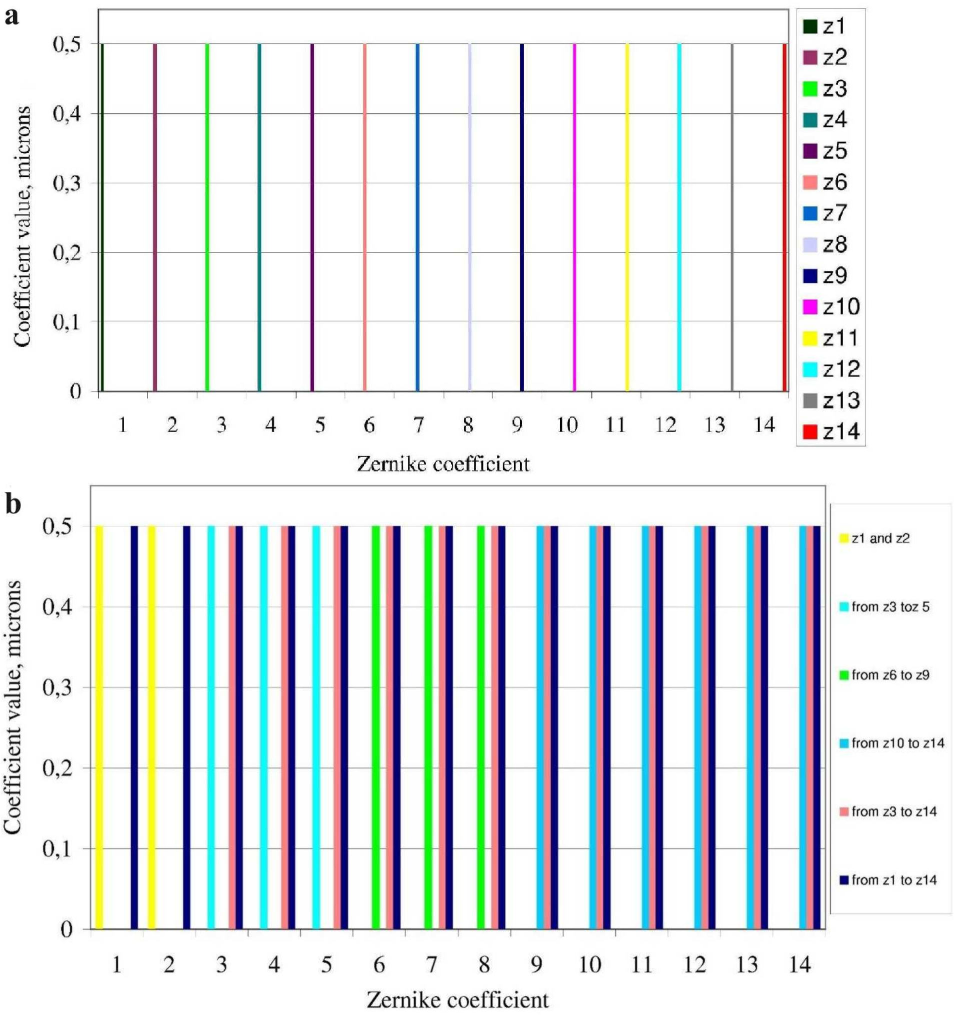

Fig. 6.2. The tests of the software algorithm. **a** - The evaluation of several Zernike coefficients. **b** - The evaluation of the Zernike coefficients composed in groups.

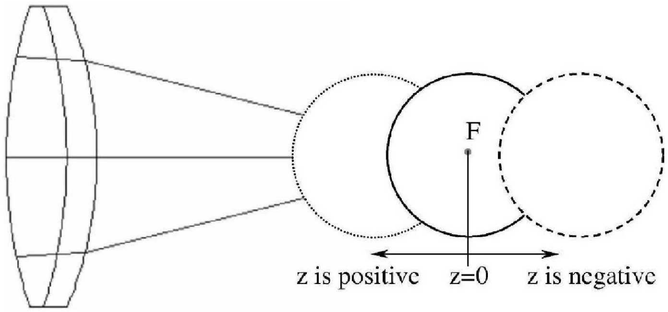

Fig. 6.3. Definition of the positive and negative axial shift for the simulation with the ZEMAX software.

Afterwards, the evaluation of the images with groups of aberrations was estimated. The value of each Zernike coefficient of a group (for example first order aberrations z_1 and z_2, then second order from z_3 to z_5 and so forth) has been set to 0.5 µm. Finally, all aberrations from z_3 to z_{14} and from z_1 to z_{14} were set to 0.5 µm. In all cases the calculated values of the Zernike coefficients were 0.0 µm except the entered coefficients having value of 0.5 µm (Fig. 6.2b).

6.2 Axial Shift

To study the influence of the axial shift on the value of the Zernike coefficients, a simulation with ZEMAX Optical Design Program (Focus Software, Inc.) was performed. The optical system of the HSS Corneal Topographer was modelled with a doublet, while the anterior surface of the cornea was represented by an aspherical mirror having an apical curvature radius R_{apical} of 7.8 mm and an asphericity parameter Q equal to -0.26 (Fig. 6.3). The mirror was moved along the optical axis from the axial position equal to "zero" towards and backwards to the doublet. The axial position equal to "zero" was defined as the position at the focal point F of the doublet[4] when the center of curvature of the mirror lies exactly in the focal plane of the doublet. The "positive" axial shift was chosen as the movement of the mirror towards the doublet and the "negative" axial shift - farther away. The simulation was performed for the light wavelength of λ=780 nm. The values of the Zernike coefficients were calculated at each axial position in intervals of 0.1 mm.

Tab. 6.1 presents changes in the value of the Zernike coefficients with the axial shift. The results of this simulation are also shown graphically in Fig. 6.4.

Only two of the Zernike coefficients, namely z_4 and z_{12} representing the defocus and spherical aberration, respectively, changed with the axial shift, while other Zernike coefficients did not change at all having the value of zero. Thereby, the defocus z_4 has a linear relationship with the axial shift (Fig. 6.4 left). The changes of the spherical

---

[4] As the focal point of the doublet the paraxial focal point (if the madrigal ray height is equal to zero) was chosen.

Tab. 6.1. Simulation of the influence of the axial shift on the value of the Zernike coefficients. The changes in the value of the Zernike coefficients z_4 and z_{12} are given.

Axial shift mm	Defocus z_4 wavelengths	Spherical aberration z_{12} wavelengths
-5	0.86686	0.00265
-4	0.69438	0.00218
-3	0.52146	0.00169
-2	0.34809	0.00116
-1	0.17427	0.00060
0	0.00000	0.00000
1	-0.17472	-0.00064
2	-0.34990	-0.00131
3	-0.52554	-0.00201
4	-0.70173	-0.00276
5	-0.87818	-0.00353

aberration z_{12} can be described with a polynomial of second degree (Fig. 6.4 right).

The test measurements were also performed with the HSS Corneal Topographer to evaluate the influence of the axial shift on the value of the Zernike coefficients using a test sample. The axial position of the sample was changed from -0.5 mm to 0.5 mm at the "zero" axial position with the distance interval of 0.05 mm. The axial position equal to "zero" ("in-focus-position") was the correct axial position detected with the Z-tracker.

The results of the measurements are similar to those of the simulation with the ZEMAX software. Only the Zernike coefficients z_4 and z_{12} were sensitive to the axial shift (Fig. 6.5), while the others did not change significantly (Fig. 6.6). Already a shift around 0.5 mm causes a change of 0.42 D in the measurement of the sphere (defocus). Thus, an incorrect axial placement of a sample (or of an eye) can yield the wrong value of the defocus (z_4) and the spherical aberration (z_{12}) obtained from a measurement. This reemphasizes the need of the use of the Z-tracker in the HSS Corneal Topographer. And indeed, the use of the Z-tracker module increases the reproducibility of the measurements with the instrument (Section 6.4.1).

Additionally, the measurements showed an agreement in the behavior of the Zernike coefficients z_4 and z_{12} compared to the simulations. The Zernike coefficient z_4 has a good linear regression with the axial shift. Also the changes in the value of the Zernike coefficient z_{12} decrease with the axial shift, but it is more difficult to describe these changes with a polynomial function. Note, that the values of the Zernike coefficients could not be compared directly because ZEMAX calculates the value of Zernike coefficients in wavelengths.

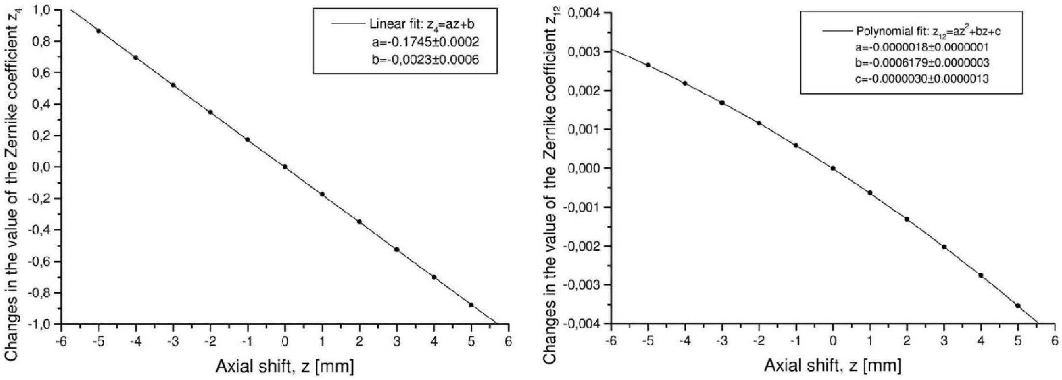

Fig. 6.4. Simulation of the influence of the axial shift on the value of the Zernike coefficients z_4 (left) and z_{12} (right). The changes in the value of the Zernike coefficients z_4 and z_{12} are plotted (Tab. 6.1).

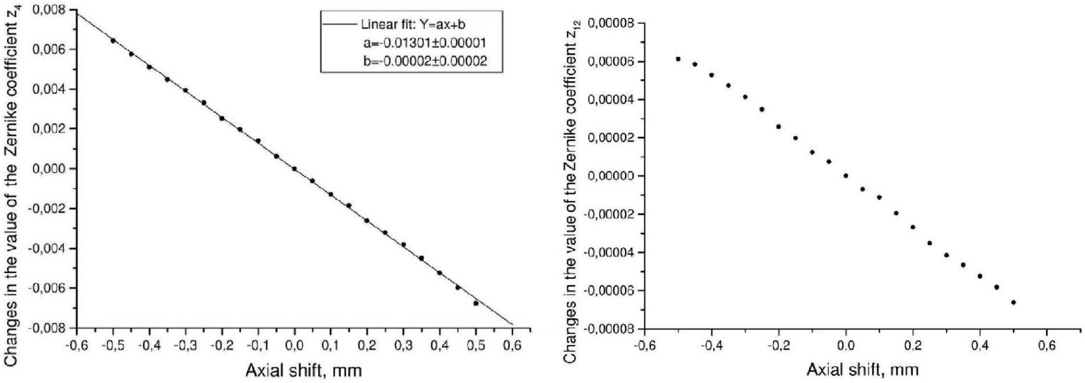

Fig. 6.5. The measurement of the influence of the axial shift on the value of the Zernike coefficients z_4 (left) and z_{12} (right). The changes in the value of the Zernike coefficients z_4 and z_{12} are plotted.

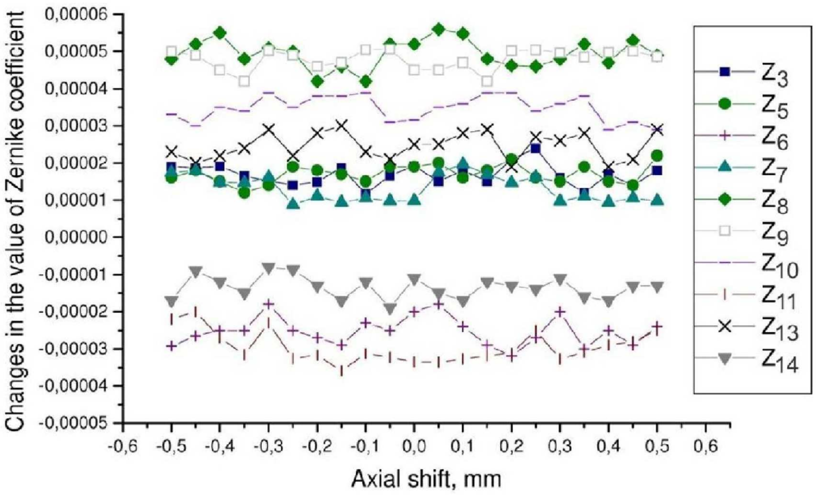

Fig. 6.6. The measurement of the influence of the axial shift on the value of the Zernike coefficients. The changes in the value of the Zernike coefficients are plotted.

6.3 Test Measurements on the Samples

Test surfaces used in these studies were steel balls and calibrated spherical samples[5] made of polymethyl methacrylate (PMMA[6]) representing an ideal spherical anterior surface of the human cornea.

Another class of measured surfaces were toric surfaces. This class of surfaces represents the simplest model of corneal astigmatism[7]. These samples are also made of PMMA.

The accuracy of different instruments and the effect of investigators were assessed using mixed-model analysis of variance that compared the mean deviation scores[8]. As an acceptable performance for clinical instruments the mean of the deviation scores must have a value of about ±0.25 D. The precision of the instrument was assessed by performing the Hartley test for homogeneity of the variance of the deviation scores. The level of significance used in the statistical tests[9] was 0.05.

---

[5] The samples were numbered from 1 to 20 for all measurements presented in this chapter.

[6] The polymethyl methacrylate (PMMA) has properties similar to that of the human cornea. It was earlier used for contact lens manufacturing, but because of its insufficient transmissibility it is not used any more.

[7] A toric surface has two orthogonal meridians, each with circular cross-sections, that are called the principal meridians.

[8] A deviation score was calculated as difference between the given and measured value.

[9] The statistical tests were performed with the computer program Origin^{TM} (Microcal Origin, Inc.).

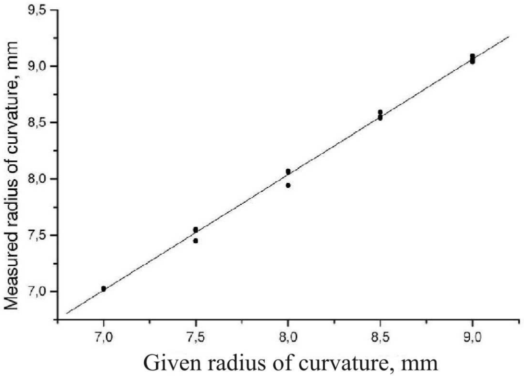

Fig. 6.7. Relationship between the radius of curvature given by the manufacturer and measured by the HSS Corneal Topographer. The measurements were done on the steel balls.

6.3.1 Accuracy

The accuracy of the system was obtained by the use of precision steel balls with the radius of 7.0, 7.5, 8.0, 8.5, and 9.0 mm. They are readily available, low in cost, and provide a precision spherical surface that represents the simplest model of the anterior surface of the cornea. The use of these spherical surfaces to test a topography system is the first logical step in testing the accuracy of the instrument. Additionally, the calibrated PMMA spheres having the known refractive power (+48.2, +45.0, +42.2, and +37.5 D) were used to evaluate the accuracy of the system.

Each test object was measured three times[10]. Then the deviation score as difference between the measured and the given refractive power[11] was calculated. The measurements on the steel balls and the spheres are summarized in Tab. 6.2.

The relationship between the curvature radius of the steel balls given by the manufacture and that measured with the HSS Corneal Topographer is represented graphically by the scatter diagram in Fig. 6.7. The measurements on the steel balls showed a statistically significant correlation (R=1.0025, N=15). The system has a tendency to read generally a higher value of the curvature than the given by the manufacture.

The measurements on the steel balls as well as on the PMMA spheres showed a good accuracy of the instrument. Fifty-three percent of the readings on the steel balls and 67% of the measurements on the PMMA spheres were within ±0.25 D of the given value. The remaining 47% of the measurements on the steel balls showed a difference of 0.26 to 0.41 D from the known value. Thus, the system is able to obtain the curvature radius (or the refractive power) close to the real value of the samples.

---

[10] It was assumed that there are no changes in system alignment or in the sample surface during the measurements.

[11] The given radius of the steel balls as well as that measured was converted into the refractive power using Eq. (3.4) and the refraction index of 1.3375 (SKI) to obtain the clinical performance of the instrument.

Tab. 6.2. Accuracy measurement of the HSS Corneal Topographer.

Ball/Sample number	Data by manufacture		Measured by HSS Corneal Topographer		Deviation score**
	(mm)	(D*)	(mm)	(D*)	(D)
Ball 1	7.0	+48.21	7.03	+48.01	+0.21
	7.0	+48.21	7.02	+48.08	+0.14
	7.0	+48.21	7.02	+48.08	+0.14
Ball 2	7.5	+45.00	7.45	+45.30	-0.30
	7.5	+45.00	7.54	+44.76	+0.24
	7.5	+45.00	7.55	+44.70	+0.30
Ball 3	8.0	+42.19	8.06	+41.87	+0.31
	8.0	+42.19	8.07	+41.82	+0.37
	8.0	+42.19	7.94	+42.51	-0.32
Ball 4	8.5	+39.71	8.55	+39.47	+0.23
	8.5	+39.71	8.59	+39.29	+0.42
	8.5	+39.71	8.54	+39.52	+0.19
Ball 5	9.0	+37.50	9.04	+37.33	+0.17
	9.0	+37.50	9.06	+37.25	+0.25
	9.0	+37.50	9.09	+37.13	+0.37
Mean±SD***					0.17±0.06
1		+48.2		+48.2	+0.05
		+48.2		+48.2	+0.03
		+48.2		+48.3	+0.08
4		+45.0		+45.2	-0.10
		+45.0		+45.1	+0.20
		+45.0		+45.1	+0.20
7		+42.2		+42.3	+0.31
		+42.2		+42.1	+0.33
		+42.2		+42.3	-0.16
10		+37.5		+37.6	+0.17
		+37.5		+37.6	-0.26
		+37.5		+37.7	+0.32
Mean±SD					0.10±0.06

* The given and measured radius of the steel balls were converted to the refractive power using the refractive index of 1.3375 (Eq. (3.4)).

** The deviation score was calculated as difference between the given and the measured refractive power.

*** The abbreviation SD indicates the standard deviation.

Tab. 6.3. Reproducibility measurements of the HSS Corneal Topographer.

Number of measurement	Sphere +45 D Examiner 1	 Examiner 2	Sphere +42.2 D Examiner 1	 Examiner 2
1	+45.24	+45.25	+42.29	+41.93
2	+45.30	+45.30	+42.51	+41.87
3	+44.82	+45.30	+42.40	+41.82
4	+45.12	+45.42	+42.03	+41.93
5	+44.70	+44.94	+42.40	+42.35
6	+45.06	+45.40	+42.35	+42.29
7	+44.94	+44.64	+42.45	+42.08
8	+44.76	+45.52	+41.77	+42.03
9	+45.36	+44.58	+42.56	+41.72
10	+45.18	+45.27	+41.93	+42.03
Mean±SD	+45.05±0.23	+45.16±0.33	+42.27±0.27	+42.00±0.20

The accuracy of the system on the PMMA spheres was a little bit better (Mean±SD: 0.10±0.06) than that on the steel balls (Mean±SD: 0.17±0.06). This may be caused through the high reflection of the steel balls compared to that of the PMMA spheres. This led to a worse signal-noise-ratio on the CCD camera of the Hartmann-Shack wavefront sensor. So the spot finding was more difficult. Because of this fact the steel balls were not included in further analyse.

6.3.2 Reproducibility

To determine the reproducibility of the system, two calibrated spheres (+45 D and +42.2 D) were measured ten times by two investigators. The spheres were repositioned after each reading. The mean refractive power and its standard deviation were then calculated for each sphere and investigator (Tab. 6.3).

Fig. 6.8 shows the deviation scores. The measurements were highly reproducible, but the tests, however, showed an effect of the examiner on the measurements (Tab. 6.4). So the readings obtained by the first examiner are more precise (reproducible) than those obtained by the second examiner. This could be explained by the fact that the first examiner has more practice and is more familiar with the instrument than the second examiner. The greatest difference between measurements by two investigators was 0.84 D.

6.3.3 Measurements of Astigmatism

The measurement of the system accuracy and reproducibility on toric surfaces that represent the regular astigmatism of the cornea was also explored.

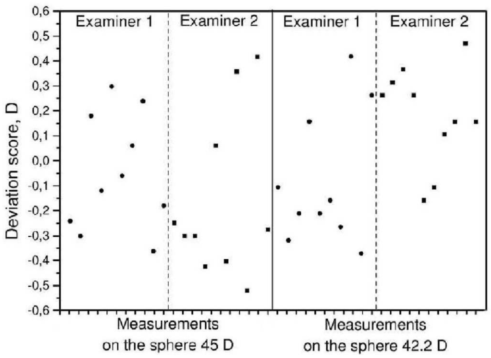

Fig. 6.8. Scatter diagram demonstrating the accuracy of the refractive power measurements in form of deviation scores for two calibrated spheres (+45 D and +42.2 D) measured by two examiners.

Tab. 6.4. Precision measurements of the HSS Corneal Topographer.

	Sphere +45 D		Sphere +42.2 D	
	Examiner 1	Examiner 2	Examiner 1	Examiner 2
Mean±SD	-0.05±0.23	-0.16±0.33	-0.08±0.27	+0.18±0.20

The astigmatic surfaces were positioned at the "best-in-focus" position and rotated. The angle of rotation varied from 0° to 180° and back with the step of 5°. The value of astigmatism and the position of the major axis were calculated using Eq. (5.25) from the Zernike coefficients z_3 and z_5 obtained from the measurement.

Fig. 6.9 shows the results of the measurements on an astigmatic PMMS sample having +1 D of regular astigmatism. The amount of measured astigmatism shows a small variation with a mean value of +0.94 D and standard deviation of +0.10 D. Fig. 6.9 (left) shows the accuracy of the readings as a scatter diagram of the deviation scores. Ninety-nine percent of the readings were within ±0.25 D of the calibrated value (only one measurement had a difference of +0.28 D). Thus, the measurements on the toric surface could be also considered as accurate (Mean±SD of the deviation scores: +0.06±0.10 D). The measurements of the axis were significant with the correlation coefficient R=0.9995, number of points N=74 (Fig. 6.9 right).

These measurements demonstrated that the system is both highly accurate and reproducible in determining the topography of spherical as well as toric surfaces that approximate the curvature of the central human cornea.

6.3.4 Reproducibility of the Zernike Coefficients

The reproducibility of the Zernike coefficients on the calibrated PMMA samples was determined. A sample was measured ten times by two investigators. The sample was

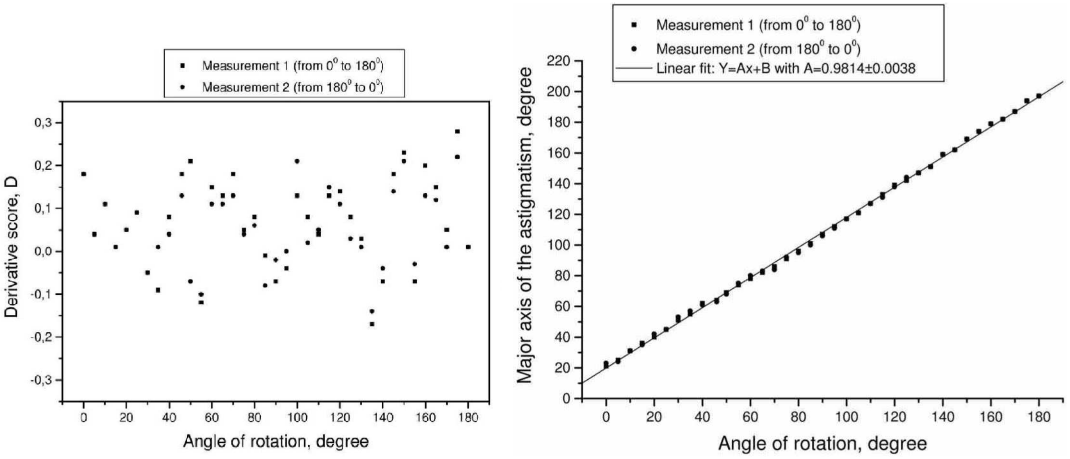

Fig. 6.9. Measurements of the amount and the axis of the regular astigmatism. Left: The scatter diagram of the deviation scores shows the accuracy of the measurement on a toric surface. Right: The measurements of the axis of the regular astigmatism show a good correlation.

repositioned after each reading. The mean value and standard deviation were then calculated for each Zernike coefficient and investigator. The relative errors calculated as the ratio of the standard deviation and the mean value for each Zernike coefficient and investigator were also determined.

One typical measurement is presented in Tab. 6.5. Fig. 6.10 shows the reproducibility of the Zernike coefficients. These measurements demonstrate that the system is reproducible to determine the Zernike coefficients on the PMMA samples. Additionally, no effect of the examiner on the measurements was obtained. The mean relative errors for the first and second investigator were 4.38% and 4.29%, respectively.

6.3.5 Comparison with Videokeratoscopy

The data measured with the HSS Corneal Topographer and those obtained with a conventional corneal topographer based on Placido-disc technology (ATLAS manufactured by Humphrey Systems) were compared.

The measurements were done on the PMMA samples with the surface in the ”best-focus” position for both systems. The statistical comparison of the data was done between these two systems for the keratometric data[12] and the statistical index describing the surface irregularity.

---

[12] Only the amount of astigmatism value could be compared because it was not possible to warrant the equal position of the samples on both systems.

Tab. 6.5. Measurements of the reproducibility of the Zernike coefficients on the PMMA sample. The mean value of each Zernike coefficient with its standard deviation (Mean±SD) and the relative error in percent are given.

Zernike coefficient Z_i^*	Examiner 1		Examiner 2	
	Mean±SD	Relative error**	Mean±SD	Relative error**
Z_1	-0.000192±0.000006	3.22	-0.000192±0.000004	2.10
Z_2	-0.000172±0.000003	1.56	-0.000175±0.000005	2.62
Z_3	-0.000070±0.000003	4.46	-0.000070±0.000003	4.45
Z_4	-0.000420±0.000029	6.91	-0.000422±0.000024	5.76
Z_5	-0.000280±0.000022	7.71	-0.000278±0.000022	7.88
Z_6	-0.000102±0.000006	6.16	-0.000102±0.000006	6.13
Z_7	0.000072±0.000004	5.55	0.000072±0.000004	5.44
Z_8	-0.000102±0.000001	0.35	-0.000102±0.000001	1.36
Z_9	-0.000011±0.000001	6.14	-0.000011±0.000001	4.43
Z_{10}	-0.000010±0.000001	5.22	-0.000010±0.000001	5.10
Z_{11}	-0.000004±0.000000	6.44	-0.000004±0.000000	6.43
Z_{12}	0.000084±0.000002	2.82	0.000085±0.000002	2.81
Z_{13}	-0.000100±0.000002	1.48	-0.000109±0.000002	2.17
Z_{14}	0.000108±0.000004	3.34	0.000109±0.000004	3.31
Sphere (D)	-0.29±0.02		-0.28±0.02	
Cylinder (D)	+0.19±0.02		+0.19±0.02	
Axis (degree)	0.13°±0.02°		0.13°±0.06°	

* The used numbering schema corresponds with that presented in Tab. 4.3.

** The relative error was calculated as $SD/Mean$ and is given in percent.

Comparison of Keratometric Data

The keratometric data (i.e., the astigmatism value[13]) were compared between the Placido-disc and the wavefront sensor systems.

For the measurements a set of precision toric surfaces modelling the regular corneal astigmatism from +1.0 D to +6.0 D was used. The value of astigmatism A for each surface was calculated using the following formula

$$A = 337.5\Big(\frac{1}{r_{great}} - \frac{1}{r_{steep}}\Big), \tag{6.1}$$

---

[13] The sphere could not be compared because ATLAS does not provide this value. Also, the meridians of the astigmatism could not be compared because the samples could not be positioned at the same angle on both systems.

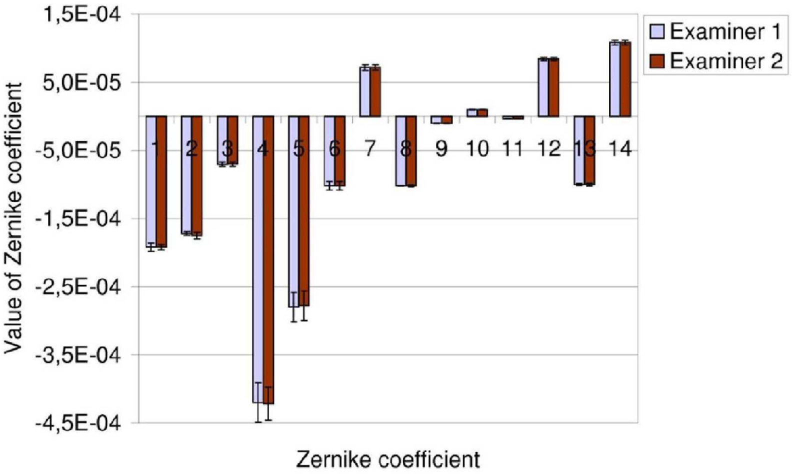

Fig. 6.10. Reproducibility of the Zernike coefficients on a calibrated sample. The mean value of each Zernike coefficient and its standard deviation are presented for two investigators.

where r_{great} and r_{steep} are the curvature radii[14] of the greatest and the steepest meridian given in mm, respectively. The amount of astigmatism in the case of the measurements with the HSS Corneal Topographer were obtained from the Zernike coefficients z_3 and z_5 using Eq. (5.25).

The results are listed in Tab. 6.6. The axis of astigmatism could not be compared because the measurements were done not at the same time, and thus, it could not be warranted that the samples are positioned in the same way on both systems.

The measurements on both systems were significant having the correlation coefficient of R=0.99, N=8 for ATLAS and R=1.01, N=8 for HSS Corneal Topographer (Fig. 6.11 left). But the measurements obtained with ATLAS were more accurate than those obtained with the HSS Corneal Topographer (Fig. 6.11 right). The mean deviation score value and its standard deviation in the case of the Placido-disc topographer and the HSS Corneal Topographer were 0.04±0.08 and -0.06±0.09, respectively. A worse precision of the HSS Corneal Topographer compared to that of ATLAS may be caused through an insufficient placement although the Z-tracker was used.

Comparison of the Surface Irregularity Index

The measurements of the surface irregularity were compared. The data are listed in Tab. 6.7.

Fig. 6.12 shows the correlation of the corneal irregularity measurement between two systems that indicates a low agreement. The correlation coefficient is R=0.771 with the number of points N=20. This may be explained by the fact that the field

---

[14] The curvature radius of the greatest and the steepest meridian for each surface were given by the manufacturer.

Tab. 6.6. Measurements on the toric surfaces.

Sample number	Given value* (D)	Measured by ATLAS (D)	Deviation score** (D)	Measured by HSS Corneal Topographer (D)	Deviation score** (D)
13	+3.72	+3.75	-0.03	+3.70	-0.18
14	+1.42	+1.25	0.17	+1.37	0.05
15	+6.03	+5.88	0.15	+6.11	-0.08
16	+2.81	+2.87	-0.06	+2.72	0.09
17	+1.00	+1.00	0.00	+1.13	-0.13
18	+4.62	+4.62	0.00	+4.72	-0.08
19	+0.89	+0.87	0.02	+0.99	-0.08
20	+2.28	+2.25	0.03	+2.31	-0.03
Mean±SD			0.04±0.08		-0.06±0.09

* The given amount of astigmatism for each surface was calculated using Eq. (6.1) from the known curvature radius of the greatest and the steepest meridian given by the manufacturer.

** The deviation score was calculated as difference between the given and the measured astigmatism.

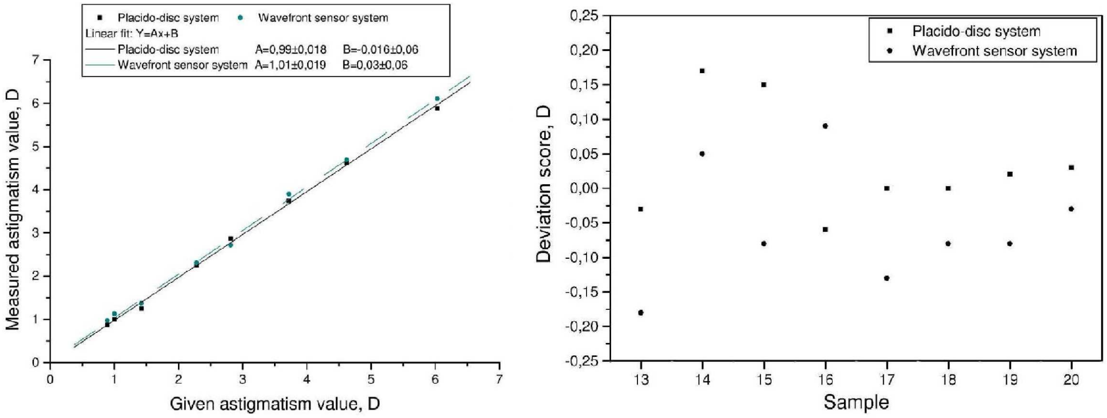

Fig. 6.11. Measurements on the toric surfaces. Left: The accuracy of the Placido-disc (ATLAS) and the wavefront sensor (HSS Corneal Topographer) systems. Right: The scatter diagram of the deviation score values demonstrating a good clinical accuracy of both systems.

Tab. 6.7. Measurements of the surface irregularity index on the PMMA samples.

Sample number	Measured by ATLAS	Measured by HSS Corneal Topographer
1	0.45	0.27
2	0.57	0.31
3	0.78	0.72
4	0.44	0.54
5	0.48	0.45
6	0.77	0.61
7	0.41	0.47
8	0.47	0.37
9	0.54	0.57
10	0.91	0.70
11	0.75	0.59
12	0.90	0.80
13	0.42	0.31
14	0.42	0.12
15	0.38	0.28
16	0.47	0.57
17	0.38	0.33
18	0.53	0.68
19	0.58	0.48
20	0.41	0.29

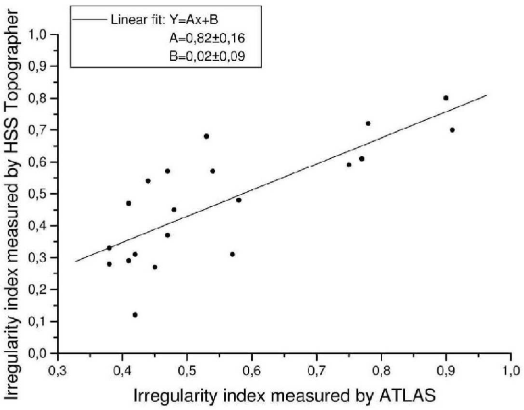

Fig. 6.12. Comparison of the surface irregularity measurement for ATLAS and the HSS Corneal Topographer.

of measurements on the samples are different for these two systems. ATLAS obtains the irregularity index for a great area on the samples being about 8 mm or more in diameter, while the HSS Corneal Topographer measures the area of about 6 mm in diameter only.

6.4 Measurements on the Human Cornea

As mentioned in the introduction to this chapter the tests of the system on human corneas are more difficult than those on the PMMA samples because the absolute power of a human cornea is unknown. Also, it is not possible to assess the accuracy of the instrument. So only the reproducibility of the Zernike coefficients on human eyes could be determined. Additionally, the eye moves permanently complicating the positioning of the anterior surface of the cornea at the correct axial and lateral position.

The keratometric data could not be compared to those measured with a standard videokeratoscope because they was not provided at the time when the measurements were made with the HSS Corneal Topographer.

6.4.1 Reproducibility of the Zernike Coefficients

To determine the reproducibility of the Zernike coefficients on the human cornea, human eyes were measured.

Tab. 6.8 shows a typical measurement on a human cornea. The measurements were made with and without the use of the Z-tracker module to evaluate its need for the measurements. The cornea was measured ten times by two investigators. The eye was repositioned after each reading. The mean value, standard deviation, and relative error were then calculated for each Zernike coefficient and investigator.

The measurements with the Z-tracker demonstrated a worse reproducibility of the Zernike coefficients on the human cornea than that on the calibrated samples (Fig. 6.13). The relative errors were in this case higher for all Zernike coefficients. This fact can be explained through eye movements during the measurement. Although the head and chin of the patient are positioned using the forehead and chin rests, and the patient was asked to look on a target, the position of the cornea is not fixed during the examination compared to that of the PMMA samples. No significant effect of investigators on the measurements was found.

The reproducibility with the use of the Z-tracker is much better than that without the Z-tracker (Fig. 6.14). All Zernike coefficients had a great relative error if no Z-tracker was used for the measurements. The relative error of the Zernike coefficient z_4 was especially high. Also, the correct placement of the anterior surface of the cornea is very important to get a correct measurement. A better reproducibility of the measurements may be obtained if a better Z-tracker module would be used that is able to compensate for the eye movements.

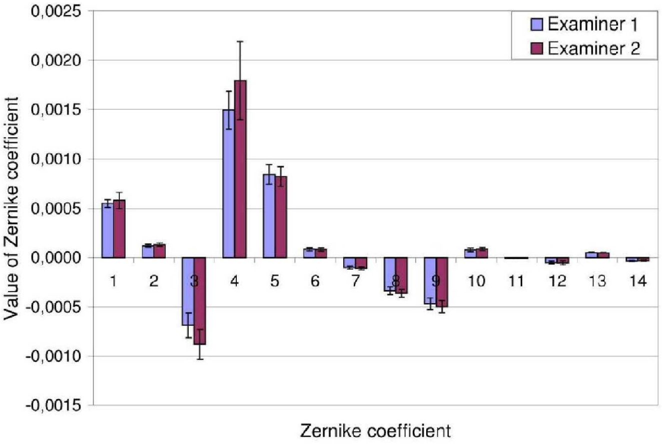

Fig. 6.13. Reproducibility of the Zernike coefficients on a human cornea with the use of the Z-tracker. The mean value of each Zernike coefficient and its standard deviation are presented for two investigators.

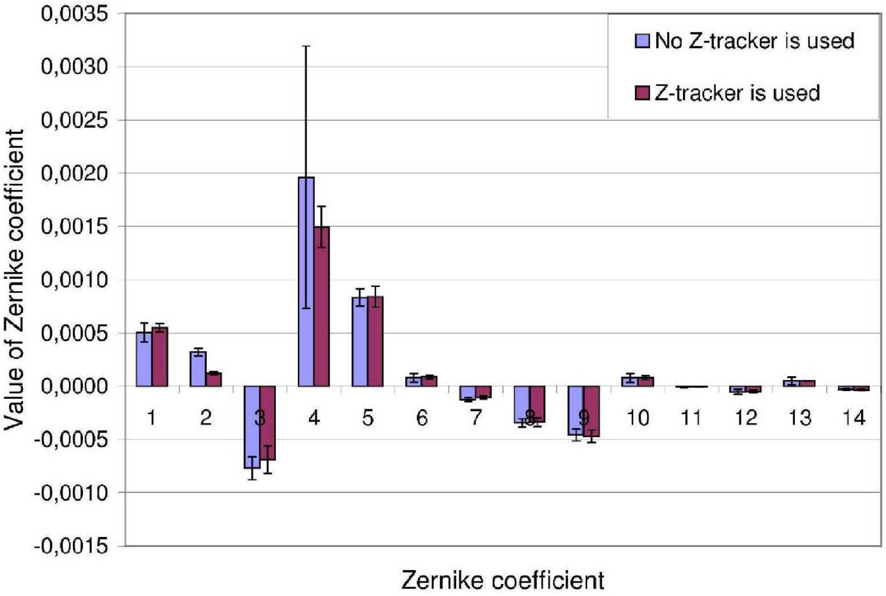

Fig. 6.14. Reproducibility of the Zernike coefficients on a cornea with and without the use of the Z-tracker. The mean value of each Zernike coefficient and its standard deviation are presented. Note, a great relative error for Zernike coefficients z_4 representing defocus if no Z-tracker module is used.

Tab. 6.8. Measurements of the reproducibility of the Zernike coefficients on a human cornea with and without the use of the Z-tracker module. The mean value, standard deviation, and relative error of each Zernike coefficient are given (Mean±SD).

Zernike coefficient	No Z-Tracker is used Examiner 1		Z-tracker is used Examiner 1		Z-tracker is used Examiner 2	
Z_i^*	Mean±SD	Relative error**	Mean±SD	Relative error**	Mean±SD	Relative error**
Z_1	0.000505±0.000090	17.81	0.000550±0.000039	7.15	0.000580±0.000080	13.81
Z_2	0.000321±0.000034	10.53	0.000121±0.000039	11.41	0.000132±0.000017	13.16
Z_3	-0.000769±0.000110	14.31	-0.000688±0.000130	18.91	-0.000880±0.000015	17.16
Z_4	0.000196±0.001230	62.60	0.001496±0.000192	12.85	0.001796±0.000040	22.11
Z_5	0.000834±0.000080	9.55	0.000842±0.000100	11.87	0.000820±0.000100	12.17
Z_6	0.000078±0.000041	52.56	0.000086±0.000017	20.24	0.000084±0.000018	22.01
Z_7	-0.000123±0.000017	13.98	-0.000103±0.000016	15.94	-0.000110±0.000017	15.59
Z_8	-0.000347±0.000039	11.46	-0.000337±0.000040	11.79	-0.000364±0.000039	10.83
Z_9	-0.000457±0.000057	12.47	-0.000471±0.000060	12.68	-0.000497±0.000060	12.01
Z_{10}	0.000077±0.000042	53.92	0.000079±0.000018	22.84	0.000090±0.000017	19.68
Z_{11}	-0.000008±0.000003	37.50	-0.000007±0.000002	27.14	-0.000009±0.000002	22.76
Z_{12}	-0.000052±0.000023	44.32	-0.000049±0.000013	26.57	-0.000052±0.000019	36.94
Z_{13}	0.000495±0.000027	5.45	0.000051±0.000004	7.75	0.000050±0.000004	7.98
Z_{14}	-0.000273±0.000007	25.93	-0.000033±0.000004	12.03	-0.000031±0.000004	11.59
Sphere (D)	+0.13±0.72	553.85	+1.00±0.13	13.00	+1.20±0.09	7.50
Cylinder (D)	+0.76±0.06	7.89	+0.72±0.08	10.46	+0.80±0.05	5.75
Axis (degree)	179.54°±4.55°	2.53	179.59°±5.23°	2.91	179.46°±3.79°	2.11

[*] The used numbering schema corresponds with that presented in Tab. 4.3.

[**] The relative error was calculated as $SD/Mean$ and is given in percent.

Chapter 7

CONCLUSION AND OUTLOOK

Although technique for assessing corneal topography has been available for many years, it is only relatively recently that its use has become more widespread, and the field of corneal topography is rapidly expanding. New principles, methodology, and new software for more realistic interpretation of the corneal surface are currently being investigated.

With the growing use of new surgical procedures such as LASIK that correct refractive errors by modifying corneal shape it is increasingly important that methods for the analysis of corneal topography keep pace.

Nowadays, the standard method for measuring corneal topography in clinical praxis is the videokeratoscopy. A videokeratoscope uses an improved version of Placido's disc that is projected on the cornea to evaluate the topography of the anterior surface. Trained observers can obtain qualitative and semi-quantitative information about the shape of the cornea from simple visual inspection of videokeratoscopic images. More exact quantitative information can only be obtained by more sophisticated analysis of the images using computer software. Modern corneal topographers provide qualitative as well as quantitative information about the corneal shape and condition above a great area of the cornea.

The major deficiency of videokeratoscopy is the assumption about the corneal shape that is approximated as a sphere. In reality, the cornea is asymmetrically aspheric. Therefore the accuracy of the videokeratoscope normally decreases as the corneal surface departs from a sphere.

In this work a corneal topographer using an alternative method for measuring corneal topography than that used by a conventional corneal topographer is presented. This corneal topographer (called the HSS Corneal Topographer) bases on the technique of the wavefront analysis with a Hartmann-Sack wavefront sensor known from astronomy. The Hartman-Shack wavefront sensor has been successfully applied for measurements of the optical aberrations on the human eye since a few years.

The major advantage of the HSS Corneal Topographer over a standard Placido's disc types topographer is its ability to directly obtain data of the corneal topography for the most important central optical zone of the cornea without any approximations.

The optical principle of measuring corneal topography with the HSS Corneal Topographer creates high demands on the optical components of the system. Especially a focussing objective must have a high optical quality to obtain the information about the topography for a large area on the human cornea. Using a wide angle objective[1] having less optical aberrations, the field measured on the cornea could be increased up to 6 mm in diameter.

A special software was written to evaluate the measurements done with the HSS Corneal Topographer. The software is extensive and contains many features providing a lot of information regarding the shape and optical quality of the cornea. It implies standard topographical maps (such as elevation and irregularity maps) and statistical indices (such as irregularity and asymmetry indices) also provided by most modern corneal topographers used by ophthalmologists. The calculation and presentation of the topographical maps and parameters was made in such a way that the data could be easily compared with those obtained by the standard corneal topographers. The user interface was kept simple to make the handling of the computer program and the measurement process for users as easy as possible.

An additional presentation of the corneal topography height data using the Zernike polynomials promises excellent advances toward the calculation of clinically relevant parameters being needed to compare different topography systems. The Zernike coefficients describing the optical quality of the corneal surface are also needed for the wavefront-based refractive surgery that became popular in last years.

The tests of the software calculation algorithm showed a perfect reliability. So it is warranted that the image analysis and evaluation processes run correctly.

The optical setup of the topography unit was improved significantly by adding a Z-tracker module for a more correct and precise positioning of the anterior surface of the cornea.

To evaluate the need of the Z-tracker module, a simulation with an optical design program (ZEMAX) was performed. The simulation showed that the incorrect placement of the cornea yields wrong values of the Zernike coefficients. The use of the Z-tracker is essential to derive an accurate and reproducible measurement on the human cornea.

The measurements with the HSS Corneal Topographer confirmed the importance of the Z-tracker module. Already, a slight displacement of a tested surface from the correct axial position of about 0.1 mm caused changes in the value of defocus of about 0.42 D. The Zernike coefficient describing the spherical aberration was also affected by the displacement. That showed that the Z-tracker module is very important for correct measurements with the HSS Corneal Topographer.

Finally, the HSS Corneal Topographer was tested for its clinical acceptance.

The measurements of the system accuracy and precision on two classes of surfaces representing the human cornea have been explored. First, the accuracy and precision of the HSS Corneal Topographer were evaluated on calibrated steel balls and spherical PMMA samples. Second, the tests on toric surfaces have been established. The

---

[1] A Leica objective with a focal length of 50 mm and a f-number of 1.0.

measurements demonstrated that the system is both highly accurate and reproducible in determining the topography of spherical as well as toric surfaces that approximate the curvature of the central human cornea.

The tests showed a small effect of the examiner on the measurements. So the readings obtained by a trained examiner were more precise (more reproducible) than those obtained by an examiner being less familiar with the instrument. So increasing practice with the instrument will enhance the significance of the measurements.

The data obtained with the HSS Corneal Topographer were also compared to that provided by a videokeratoscope used in clinical praxis (ATLAS corneal topographer manufactured by Humphrey Systems). The comparison showed a good accuracy of the HSS Corneal Topographer, but the measurements obtained with the conventional corneal topographer were more precise than those obtained with the HSS Corneal Topographer.

A comparison of the corneal irregularity measurements between these two systems indicated a low agreement. This may be explained by the fact that the area has been measured on the samples is different for these two systems. ATLAS obtains the irregularity index for a greater area on the samples being about 8 mm or more in diameter, while the HSS Corneal Topographer measures the area of about 6 mm in diameter only.

The Zernike coefficients could not be compared because ATLAS does not provide this kind of information.

The test measurements on human corneas were more difficult than those on the samples because of eye movements.

The studies of the reproducibility of the Zernike coefficients demonstrated the importance of the Z-Tracker for the correct placement of the corneal surface. While the HSS Corneal Topographer achieves such a high degree of accuracy on the samples acceptable for the clinical use, the instrument is not precise enough to be applied for the measurements on the human cornea. Although a patient is asked to fix the look on the target the remaining eye movements still significantly affect the measurements. The Z-tracker module used in the current optical setup helps to adjust the anterior surface of the samples at the correct axial position, but the Z-tracker is not able to compensate for the axial eye movements during a measurement. Thus, a more precise and accurate eye tracking is needed to get better measurements on the human cornea.

No comparison with the videokeratography data was possible for the measurements on the human cornea because the videokeratoscope was not available at this time.

Some additional devices and programs could improve and expand the capabilities of the HSS Corneal Topographer in the future.

First, an objective specially designed for the system[2] would improve the optical quality of the instrument. The images of the spot pattern would be especially good

---

[2] The Leica objective being used is designed for a photo camera, and so it is optimized for visible light. The HSS Corneal Topographer uses an infrared laser as light source. Thus, from the optical perspective the focusing of infrared light by this objective is normally worse than that for visible light.

if this objective would also correct the optical aberrations caused by other optical components of the system.

In present version the software algorithm works manually. This complicates the evaluation process performed by a user. The spot finding algorithm should be programmed to run automatically to eliminate the effect of the investigator on the results of the measurements.

More functions (such as Modulation Transfer Function, Point Spread Function, and so on) describing optical performance of the cornea and corneal visual acuity would help to obtain the corneal contribution to the overall vision. That way the corneal topography will allow a better understanding of correlations between the shape, optical aberrations, and visual acuity of the cornea. Thus, one can determine if visual problems are caused by the cornea or through the inner optics of the eye.

In spite of the Z-tracker, a measurement done with the HSS Corneal Topographer seems to be affected by the placement of a tested surface. In the present optical setup there is no possibility to compensate for eye movements during an examination that strongly affect a measurement. An examiner has to align the axis of the instrument with the visual axis of the patient's eye using a watching camera. The correct axial position is then given by the maximal intensity detected on the photomultiplier. This works correctly for a fixed surface, but is sometimes insufficient for a constantly moving surface such as human cornea. An electronic module for the Z-tracker that is able to persistently and rapidly compensate for the axial eye movements would enhance the reproducibility of the measurements performed on the human cornea.

Additionally, more clinical studies for testing of the HSS Corneal Topographer on human eyes are necessary. This will provide a better statistic and give an evidence for a possible clinical usefulness of the instrument. Also comparisons of the topography data obtained with the HSS Corneal Topographer on human eyes to those provided by the standard corneal topographers are needed to estimate the clinical acceptance of the system.

Appendix A

SOFTWARE DESCRIPTION

Corneal Topography is a computer program specially written for the HSS Corneal Topographer. This software implies the image processing of the spot pattern to reconstruct the corneal shape.

This chapter provides explanation of the conventions used in the computer program and description of available procedures. Tutorials on using the software are also given.

A.1 User Interface

The interface of the software has been designed to be simple to use. Most features are accessed by selecting options from either pop-up or pull-down menus. Keyboard shortcuts are provided for quickly navigation or bypassing the menu structure. In this section the details of the user interface are presented.

A.1.1 Main Menu

There are four menu options in the start up window: **File**, **Edit**, **View**, and **Help**. Every of these menu headings has several drop-down menus. Some menu options are available every time, some only by special conditions. Some of the menu options can be also selected from tool bars.

File

From the **File** menu an exam can be started, an image loaded, saved and printed.

- **New Exam**. This option allows to start a new examination by showing and taking a recent spot pattern.
- **Open Exam**. This option opens an existing exam.
- **Save Exam**. This option saves results of an examination into a file.
- **Print Exam**. This option prints the results of a current examination.

- **Open Image**. This option opens an existing image.
- **Save Image**. This option saves a current image as BMP or TIFF file.
- **Print Image**. This option prints a current spot pattern.
- **Save Spot Positions**. This option allows the user to save the actual spot positions into a file after they have been found.
- **Save Coefficients**. This option allows the user to save the Zernike coefficients into a file after they have been calculated.
- **Exit**. This option closes the computer program.

Edit

The **Edit** menu option contains two basic choices. One choice **Options** is used to show and modify system or calculation specifications. The other choice **Reference** serves for the setting of the reference spot positions.

From the **Edit/Options** menu the system parameters can be changed. The options dialog window, as shown in Fig. A.1, contains several dialog tabs that allow global preferences for the features in computer program to be specified.

- **Calculation Algorithm**. This dialog tab allows the user to specify some of the important calculation parameters such as number of iterations, spot size, and number of spots used for the image analysis. The user can determine the corneal reference radius and the order of Zernike polynomials. The file with the current reference spot positions is also shown here.
- **CCD Chip**. The user can specify the chip parameters of the used CCD camera.
- **Lens Array**. The characteristics of the micro lens array should be set here.
- **Optical System**. The parameters of the optical system can be changed here.

The user can navigate between the dialogs tabs by clicking on the tab with the mouse. To change the parameters, move the cursor to the desired cell and type the new value in. Some parameters are limited, and those value can be modified only by clicking with the mouse on their up-and-down button near the cell to increase or minimize the parameter value. The **Options** dialog window can be also quickly selected from the tool bar.

From the **Edit/Reference** menu the reference spot positions can be set. To change the reference spot positions, a reference image should have been opened. After the spots have been found as described in Example 3, the user have to select **Edit/Reference** and click an **OK** button in the message window. The reference spot positions will be overwritten and set to those that have been even found.

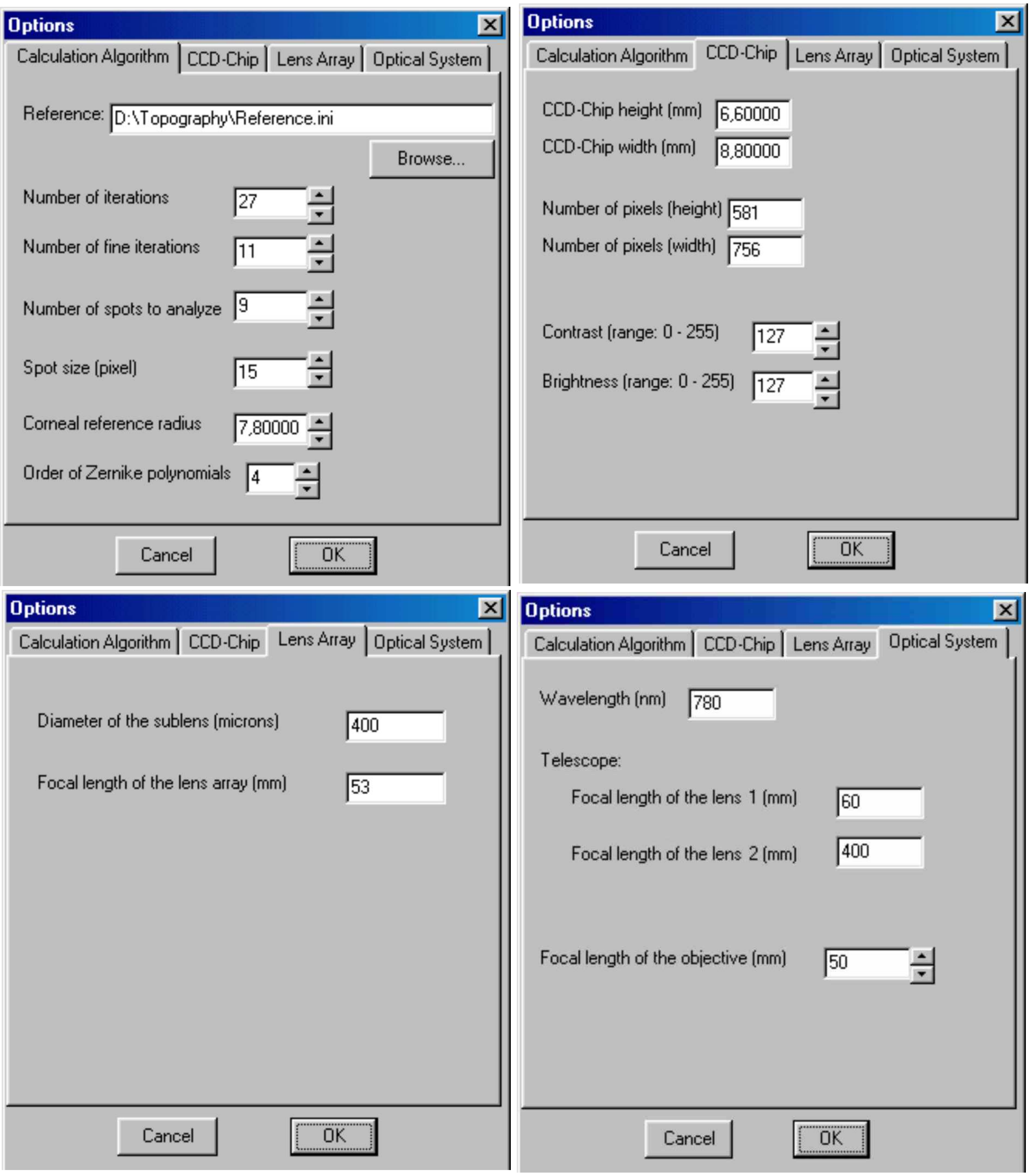

Reference: D:\Topography\Reference.ini
Number of iterations 27
Number of fine iterations 11
Number of spots to analyze 9
Spot size (pixel) 15
Corneal reference radius 7,80000
Order of Zernike polynomials 4

CCD-Chip height (mm) 6,60000
CCD-Chip width (mm) 8,80000
Number of pixels (height) 581
Number of pixels (width) 756
Contrast (range: 0 - 255) 127
Brightness (range: 0 - 255) 127

Diameter of the sublens (microns) 400
Focal length of the lens array (mm) 53

Wavelength (nm) 780
Telescope:
Focal length of the lens 1 (mm) 60
Focal length of the lens 2 (mm) 400
Focal length of the objective (mm) 50

Fig. A.1. Option dialog tabs.

View

The **View** menu option has the following items:

- **Positions**. This option allows to show the current reference and actual spot positions as well as the differences between them.
- **Coefficients**. This menu option lists the Zernike coefficients that have been calculated.
- **Topography**. This option shows the topographical maps and corneal parameters.

Help

The **Help** menu option provides help information.

A.1.2 Tool Bars

The main window also displays a row of buttons just below the menu bar. This toolbar buttons are used to quickly select some of common operations. All of the buttons represent functions and features available on the menu.

The tool bars are as follow (from left to right): New Exam, Open Exam, Save Exam, Print Exam, Open Image, Save Image, Show Reference, Show Spots, Show Difference, Show Topography, Show Zernike coefficients, Set Options, and Help.

A.1.3 Keyboard Shortcuts

Most of the commonly used menu options have keyboard equivalent which may be faster to use. The hot keys for common window operations are given in Tab. A.1.

Tab. A.1. Hot keys.

Key combination	Description
Ctrl+N	Start a new exam
Ctrl+O	Open an existing image
Ctrl+S	Save a current spot pattern into a file
Ctrl+P	Print a current exam
Ctrl+Z	Save the Zernike coefficients into a file
Ctrl+Q	Close the computer program (Exit)
F1	Help
F9	Edit options

A.1.4 Panels

The software has different types of panels, each of which serves a different purpose.

Live Image Panel

"Live Image" panel allows to show and take a current live image from the CCD camera (Fig. A.2).

Using the scroll bars, the contrast and brightness of the CCD camera can be changed. By clicking on "Take Image" button the image will be taken and shown in "Do Analysis" panel.

Additionally, an image from the watching camera with a patient's eye can be viewed that helps to center the eye on the visual axis of the instrument.

Do Analysis Panel

"Do Analysis" panel shows an actual opened image and allows the user to find the current spot positions (Fig. A.3).

The number of spots to be taken into account by the evaluation can be selected from the list using the drop down button. Also the form of the pattern (circular or rectangular) has to be chosen using corresponding radio buttons.

The user can see the spot positions (marked as green crosses) loaded from the reference file and the actual spots that have been found (marked as red crosses) as well as the differences between them represented as yellow lines by clicking on the check boxes next to the option. Additionally, the spot positions calculated from the theory for the given parameters of the optical system can be shown[1].

Show Results Panel

"Show Results" panel shows corneal topography: different maps, corneal parameters, statistical indices, the Zernike coefficients, and some other data.

In Fig. A.4 the computer display of the Show Results panel summarizing the measurement results of an eye is presented. In the left part of the panel, the elevation and irregularity maps (Section 3.3.1) are displayed in a color-coded form. Every map has a color scale that assigns particular color to data range. We used relative scale[2] for colors that identifies the actual minimal and maximal value of a particular cornea.

In the middle of the panel some corneal parameters and data are shown. The corneal radius, refractive power, corneal elevation, and irregularity (wavefront error in microns) at any point of the corneal surface can be shown by moving the mouse above the maps to that point. All of these parameters are summarized at the top of

---

[1] The theoretical spot positions commonly differ from the reference spot positions being loaded because they do not consider all existing optical aberrations of the system.

[2] The other often used scale type is an absolute scale with the number of colors, step size, and range being constant. This scale gives sometimes a better presentation of the corneal topography.

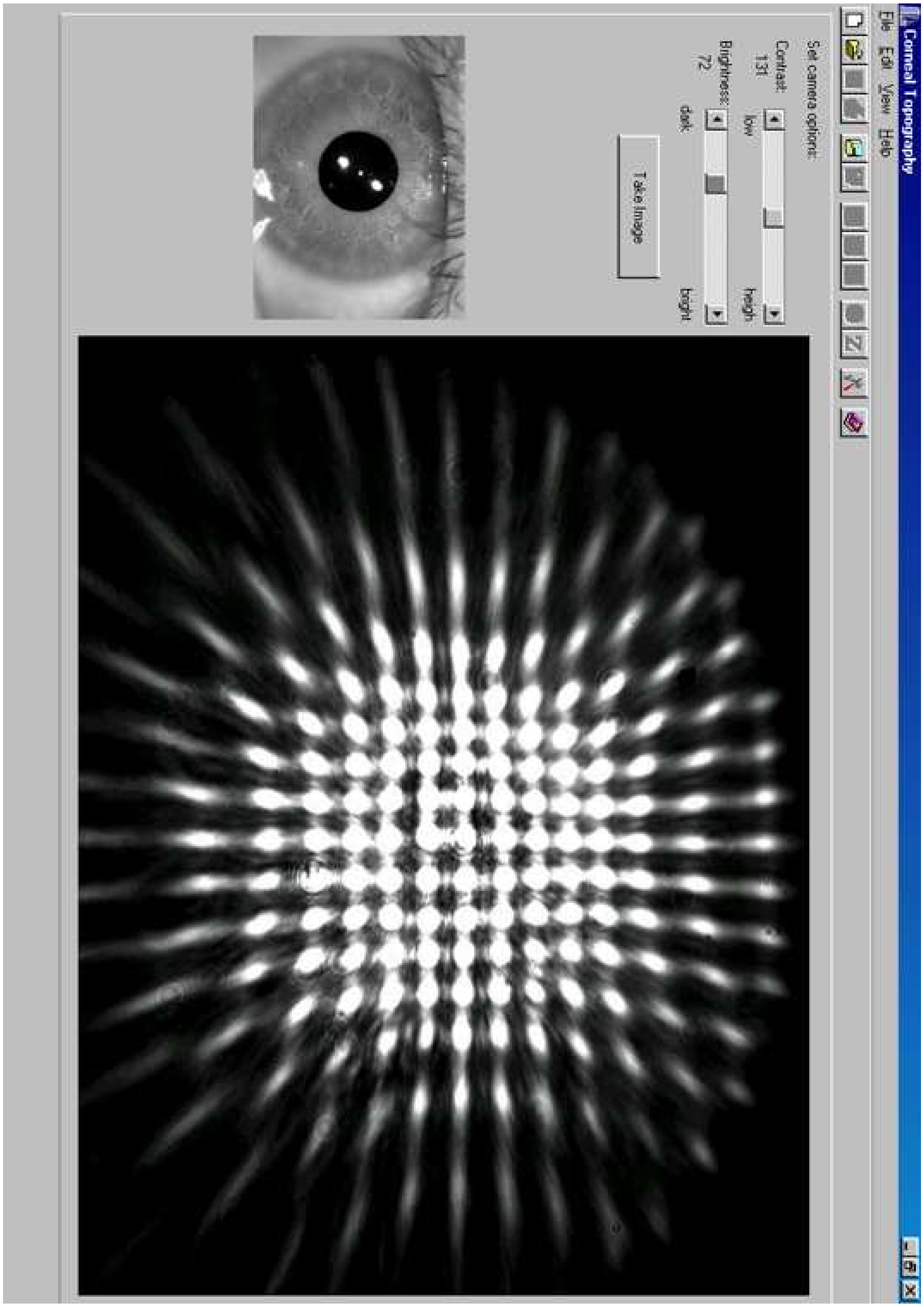

Contrast: 131

Brightness: 72

Fig. A.2. "Live Image" panel.

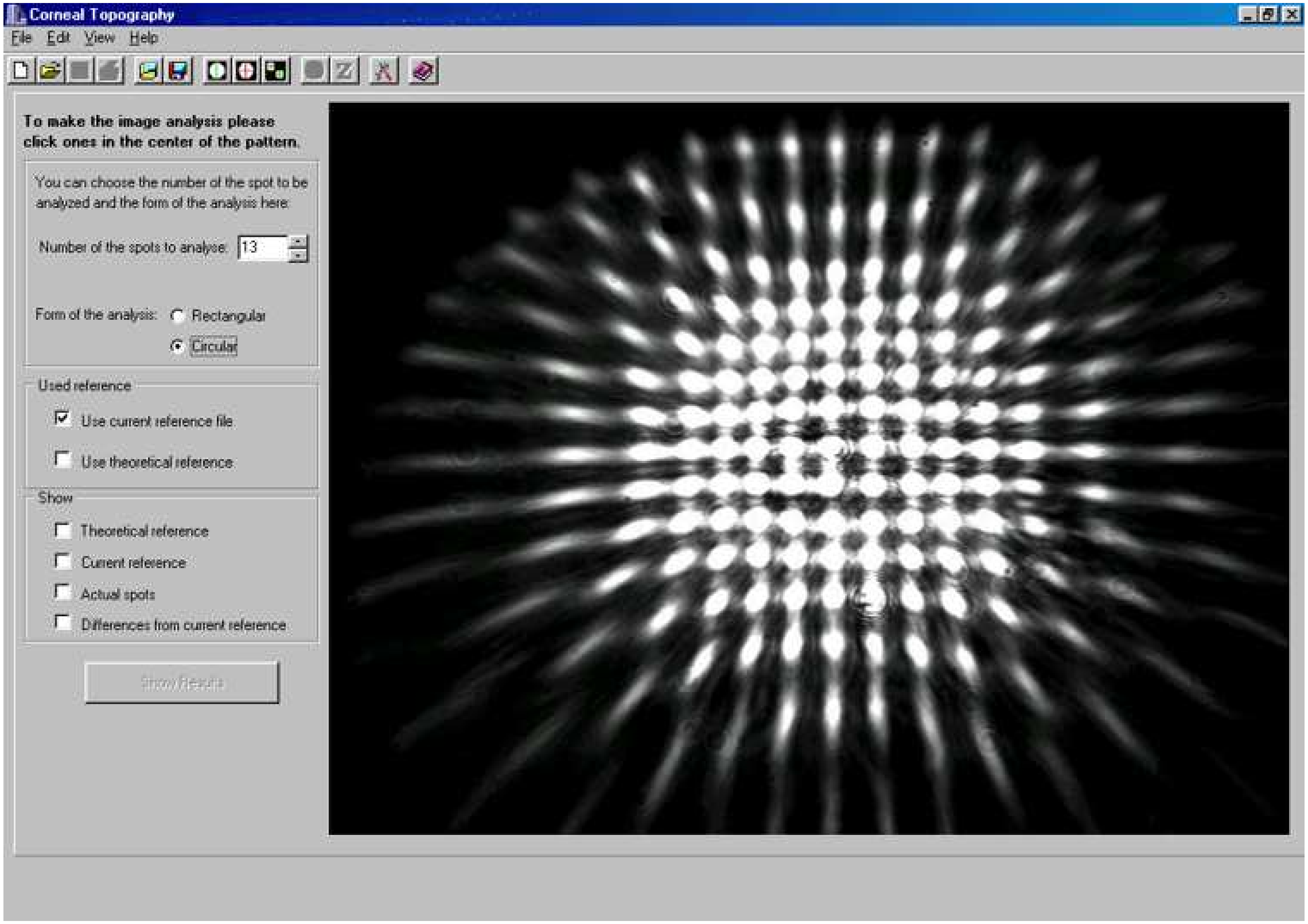

To make the image analysis please click ones in the center of the pattern.

You can choose the number of the spot to be analyzed and the form of the analysis here:

Number of the spots to analyse: 13

Form of the analysis: ○ Rectangular ● Circular

Used reference

☑ Use current reference file

☐ Use theoretical reference

Show

☐ Theoretical reference

☐ Current reference

☐ Actual spots

☐ Differences from current reference

Fig. A.3. "Do Analysis" panel.

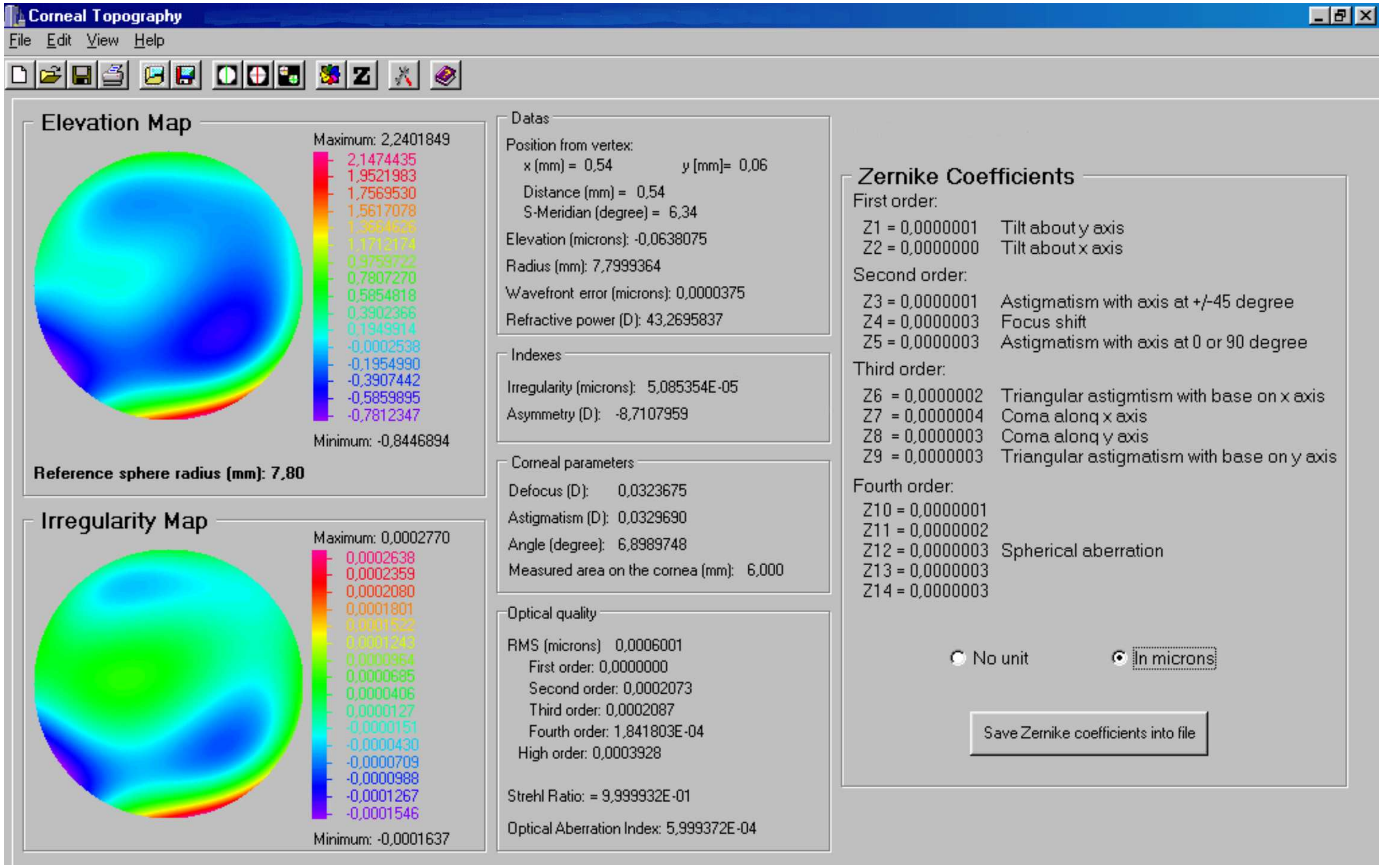

Reference sphere radius (mm): 7,80

Position from vertex:
x (mm) = 0,54 y (mm)= 0,06
Distance (mm) = 0,54
S-Meridian (degree) = 6,34
Elevation (microns): -0,0638075
Radius (mm): 7,7999364
Wavefront error (microns): 0,0000375
Refractive power (D): 43,2695837

Irregularity (microns): 5,085354E-05
Asymmetry (D): -8,7107959

Defocus (D): 0,0323675
Astigmatism (D): 0,0329690
Angle (degree): 6,8989748
Measured area on the cornea (mm): 6,000

RMS (microns) 0,0006001
First order: 0,0000000
Second order: 0,0002073
Third order: 0,0002087
Fourth order: 1,841803E-04
High order: 0,0003928

Strehl Ratio: = 9,999932E-01

Optical Aberration Index: 5,999372E-04

First order:
Z1 = 0,0000001 Tilt about y axis
Z2 = 0,0000000 Tilt about x axis
Second order:
Z3 = 0,0000001 Astigmatism with axis at +/-45 degree
Z4 = 0,0000003 Focus shift
Z5 = 0,0000003 Astigmatism with axis at 0 or 90 degree
Third order:
Z6 = 0,0000002 Triangular astigmtism with base on x axis
Z7 = 0,0000004 Coma along x axis
Z8 = 0,0000003 Coma along y axis
Z9 = 0,0000003 Triangular astigmatism with base on y axis
Fourth order:
Z10 = 0,0000001
Z11 = 0,0000002
Z12 = 0,0000003 Spherical aberration
Z13 = 0,0000003
Z14 = 0,0000003

Fig. A.4. ”Show Results” panel.

the middle column in the group ”Data”. In the group ”Indices” the evaluated corneal statistics[3] (such as irregularity and asymmetry indices) are listed. The box ”Corneal Parameters” contains corneal sphere, cylinder[4], and area measured on the cornea. In addition, information regarding optical performance[5] of the cornea (the indices such as RMS of different orders, OAI, and Strehl ratio) is given.

On the right side of the panel, the Zernike coefficients up to 4th order are listed. They can be shown without units or in microns.

A.2 Getting Started

This section goes through step-by-step examples that teach how to use the computer program. In the first example an examination will be performed. In the second example an existing image will be open, and in the third example an opened spot pattern will be analyzed. The fourth example explains how to set or change the reference spot positions.

A.2.1 Example 1 - Do a New Measurement

First of all, the computer program should be run. The main screen will appear. To begin, show a live image by clicking on **File/New Exam**. Once ”Live Image” panel is shown, the live image can be seen in the right part of the window. The contrast and brightness of the CCD camera can be controlled with the scroll bars to achieve a best signal-to-noise ratio.

Now, a patient’s eye should be positioned. There are two facilities helping by the positioning. First, use the watching camera to center the eye on the visual axis of the instrument moving the instrument up and down, left and right. Second, check if the anterior surface of the cornea is at the correct axial position by watching the intensity on the photomultiplier. It should be as maximal as possible to be sure the eye is positioned correctly. To correct the axial position of the eye, move the instrument towards or backwards to the eye in the axial direction. The patient’s chin should be positioned on the chinrest and forehead pressed against the forehead rest. Additionally, the patient has to fix on the target during the exam (black cross on the green background).

After the eye has been positioned, a measurement can be done. To start the measurement, click on ”Take Image” button. Now, ”Do Analysis” panel displaying the taken image appears on the screen, and the image can be analyzed (see Example 3).

The taken image can be also saved or printed by clicking on **File/Save Image** or **File/Print Image**, respectively.

---

[3] The highlighted statistic is explained in Section 3.3.2.

[4] These data are determined by Eq. (5.25).

[5] For more information, Section 5.6.3.

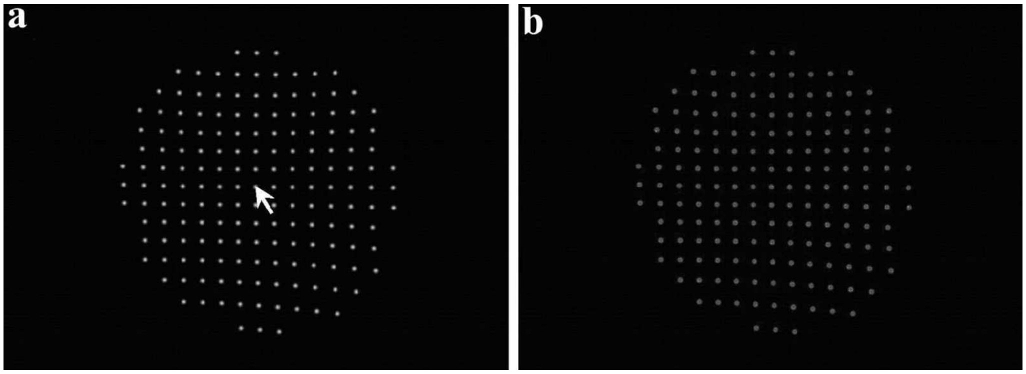

Fig. A.5. By clicking on the middle spot of a spot pattern (**a**) the centroids (spot gravity points) will be found and marked (**b**).

A.2.2 Example 2 - Open an Existing Image

The software allows to load an existing image, provides its analysis and graphical presentation of corneal topography. The supported file formats are BMP and TIFF.

To load an image select **File/Open Image**. The list of files in dialog window will be generated. When the image have been selected, click on the **OK** button, and the program will open the image in "Do Analysis" panel. Now, the image can be analyzed (see Example 3).

A.2.3 Example 3 - Analyze an Image

After a new image has been taken (see Example 1) or an existing image has been opened (see Example 2), it can be analyzed.

First, the reference spot positions should be loaded correctly. By program start the reference is loaded from reference file. If there are some problems, a message informing that the reference has not been found will appear at the start of the computer program. If the reference spot positions are wrong or not loaded please follow Example 4 to load or change the reference. The current reference spot positions can be shown by clicking on the check box **Current Reference** in the group box "Show".

Next, the user need to set a number of the spots that should be taken into account by the image analysis. It can be done using the drop down button. The form (rectangular or circular) of the spot pattern must be also selected for the analysis using the corresponding radio button.

Ones more, the options must be correct. To see what options are defaults or to edit them, click on **Edit/Options** in the menu or on the tool bar "Set Options".

Because the evaluation algorithm does not work automatically, the user has to make evaluation manually. So click on the middle spot of the spot pattern to find all centroids (spot gravity points) (Fig. A.5). After this, the spots being found will be marked, and "Show Results" button will be available. Clicking on this button takes the user to the "Show Results" panel showing the corneal topography (Section A.1.4).

The results of an examination can be saved into a file or printed by clicking on **File/Save Exam Into File** or **File/Print Exam**, respectively.

A.2.4 Example 4 - Set a Reference

The user can change the reference spot positions by loading a reference image (see Example 2) and clicking on the middle spot of the spot pattern (see Example 3). Before doing it, the number of spots and the form of the spot pattern should have been chosen. The user can select the number of spots by clicking on the drop down button for the spot number. The radio buttons ”Circular” and ”Rectangular” determine the pattern form used by the image analysis.

The spot positions being found can be saved as reference positions by opening **Edit/Reference** and clicking **OK**.

Bibliography

[1] Atchinson D.A., Smith G. (ed.) Optics of the human eye, Butterworth-Heinemann, 2000

[2] Belin M.W., et al., The PAR technology corneal topography system, Refrect. Corneal. Surg., 8 (1992), 88-96

[3] Bille J.F., Harner C.F.H., Loesel F.H. (ed.) Aberration-Free Refractive Surgery: New Frontiers in Vision, Springer, 2003

[4] Binder P., Videokeratography, CLAO J., 21 (1995), 133-144

[5] Charman W.N. (ed.) Vision and Visual Dysfunction, Volume 1: Visual Optics and Instruments, 1991

[6] Cohen K.H., Tripoli N.K., Pellom A.C., et al., A new photogrammetric method for quantifying corneal topography, Invest. Ophthalmol. Vis. Sci., 25 (1984), 323-330

[7] Corbett M.C., et al., Corneal topography using a new moiré image-based system, Eur. J. Implant. Ref. Surg., 7 (1995), 354-371

[8] Corbett M.C., Rosen E.S., O'Brart D. (ed.) Corneal Topography: Principles and applications, BMJ Books, 1999

[9] Cubalchini R., Modal wavefront estimation from phase derivative measurements, J. Opt. Soc. Am., 69 (1979), 972-977

[10] Dorsch R.G., Haimerl W.A., Esser G.K., Accurate computation of mean power and astigmatism by means of Zernike polynomials, J. Opt. Soc. Am. A, 15 (1998), 1686-1688

[11] Doss J.D., Hutson R.L., Rowsey J.J, Brown D.P., Method for calculation of corneal profile and power distribution, Arch. Ophthalmol., 99 (1981), 1261-1265

[12] Dunne C.M., Royston J.M., Barnes D.A., Normal variations of the posterior corneal surface, Acta Ophthal., 50 (1992), 255-261

[13] Le Grand Y., El Hage S.G, Physiological Optics, Springer, 1980

[14] Helmholz H. von, Handbuch des physiologischen Optik, Hamburg, Germany, Leopold Voss, 1909

[15] Herrmann J., Least-squares wavefront errors of minimum norm, J. Opt. Soc. Am., 70 (1980), 28-35

[16] Hersh P.S., A standard classification of corneal topography after laser refractive surgery, J. Ref. Surg., 13 (1997), 571-578

[17] Holladay J.T., Corneal topography using the Holladay Diagnostic Summary, J. Cataract Refract. Surg., 23 (1997), 209-221

[18] Kawara T., Corneal topography using moiré contour fringes, Applied Optics, 18 (1979), 3675-3678

[19] Keating M.P., Geometric, Physical and Visual Optics, Butterworths-Heinemann, Stoneham, MA, 1988

[20] Kiely P.M., Smith G., Carney G., The mean shape of the human cornea, Optica Acta, 29 (1982), 1027-1040

[21] Klein S.A., Mandell R.B., Shape and Refractive Powers in Corneal Topography, Invest. Ophthamol. Vis. Sci., 36 (1995), 2096-2109

[22] Klehr H., Aufbau eines Hartmann-Shack-Sensor-Systems zur Vermessung der Hornhauttopography des menschliches Auges für den klinischen Einsatz, Diploma thesis, University of Heidelberg, 2000

[23] Klyce S.D., Computer-assisted corneal topography. High-resolution graphic presentation and analysis of keratoscopy, Invest. Ophthamol. Vis. Sci., 25 (1984), 1426-1436

[24] Levene J.R., The true inventors of the keratoscope and photokeratoscope, Br. J. His. Sci., 2 (1965), 324-341

[25] Liang J., Grimm B., Gölz S., Bille J.F., Objective measurement of wave aberrations of the human eye with the use of a Hartmann-Shack wave-front sensor, J. Opt. Soc. Am. A, 11 (1994), 1949-1957

[26] Liang J., Wiliams D.R., Aberrations and retinal image quality of the normal human eye, J. Opt. Soc. Am. A, 14 (1997), 2873

[27] de Limo Monteiro D.W., CMOS-based integrated wavefront sensor, PhD thesis, Technical University Delft, The Netherlands, 2002

[28] Lowe R.F., Clark B.A., Posterior corneal curvature: Correlations in normal eyes and in eyes involved with primary angle-closure glaucoma, Brit. J. Ophthalmol., 57 (1973), 464-470

[29] Macrae S.M., Schwiegerling J., Snyder R., Customized corneal ablation and super vision, J. Refract. Surg., 16 (2000), S230-S235

[30] Madea N., et al., Automated keratoconus screening with corneal topography analysis, Invest. Ophthalnol. Vis. Sci., 1994, 35, 2749-2757

[31] Maguire L.J., Singer D.E., Klyce S.D., Graphic presentation of computer-analyzed keratoscope photographs, Arch. Ophthalmol., 105 (1987), 223-230

[32] Mueller F., Weiterentwicklung eines Hartmann-Shack-Wellenfrontsensors zur Verwendung am menschlichen Auge, Diploma Thesis, University of Heidelberg, 1998

[33] Oyster C.W., The Human Eye: Structure and Function, Sinauer Associates Inc. Publishers, 1999

[34] Patel S., Marshall J., Fitzke F.W., Shape and radius of posterior corneal surface, Refract. Corn. Surg., 9 (1993), 173-181

[35] Pfund J., Lindlein N., Schwider J., Dynamic range expansion of a Shack-Hartmann sensor by use of a modified unwrapping algorithm, Opt. Lett., 23 (1998), 995-997

[36] Placido A., Neue Instrumente, Centralbl Prakt Augenheilkd, 6 (1882), 30-31

[37] Rowsey J.J., Reynolds A.E., Brown R., Corneal topography: Corneascope, Arch. Ophthalmol., 99 (1981), 1093-1100

[38] Royston J.M., Dunne C.M., Barnes D.A., Measurement of the posterior corneal radius using slit lamp and Purkinje image techniques, Ophthal. Physiol. Opt., 10 (1990), 385-388

[39] Schanzlin D.J., Robin J.B. (ed.) Corneal Topography: Measuring and Modifying the Cornea, Springer, 1989

[40] Scheiner C., Oculus Hoc est: fundamentum opticum, Insbruck, 1619

[41] Seitz B., Behrens A., Langenbucher A., Corneal topography, Curr. Opinion in Ophthalmol., 8 (1997), 8-24

[42] Smith G., Atchison D., The eye and visual optical instruments, Cambridge University Press, 1997

[43] Southwell W.H., Wavefront estimation from wavefront slope measurement, J. Opt. Soc. Am., 70 (1980), 998-1006

[44] Rousset G., Wavefront sensor, *In*: Roddier F.J. (ed.) Adaptive Optics in Astronomy, Cambridge University Press, Cambridge (UK), 1990

[45] Takasaki H., Moiré topography, Applied Optics, 9 (1970), 1467-1472

[46] Thibos L.N., at all, Standards for Reporting the Optical Aberrations of Eyes, J. Refract. Surg., 18 (2002), S652-S660

[47] Walsh G., Charman W.H., Howland H.C., Objective technique for the detection of monochromatic aberrations of the human eye, J. Opt. Soc. Am. A, 1 (1984), 987

[48] Warnicki J.W., Corneal topography using computer analyzed rasterstereographic images, Applied Optics, 27 (1988), 1135-1140

[49] Vaughan D., Asbury T., General Ophthalmology, Prentice-Hall, London, 1992

[50] Wang J.Y., Silva D.E., Wave-front interpretation with Zernike polynomials, Applied Optics, 19 (1980), 1510-1518

[51] Wilson S.E., Klyce S.D., Quantitative descriptors of corneal topography: A clinical study, Arch. Ophthalmol., 109 (1991), 349-353

[52] Wilson S.E., Klyce S.D., Husseini Z.M., Standardized color-coded maps for corneal topography, Ophthalmology, 100 (1993), 1723-1727

[53] Use of the keratometer, *In*: Bennett A.G. (ed.) Optics of contact lenses, ADO, London, 1974

[54] Zernike F. von, Beugungstheorie des Schneidenverfahrens und seiner verbesserten Form, der Phasenkontrastmethode, Physica, 1 (1934), 689-704

[55] The detailed information about Orbscan II can be found on Internet: http://www.orbscan.com

[56] User manual of ATLAS: A clinical guide to the Humphrey Corneal Topography System, Humphrey Systems

Index